

Advances in Optical Technologies

Microwave Photonics

Guest Editors: Borja Vidal, Nathan J. Gomes, Tadao Nagatsuma,
and Thomas E. Darcie





Microwave Photonics

Advances in Optical Technologies

Microwave Photonics

Guest Editors: Borja Vidal, Nathan J. Gomes,
Tadao Nagatsuma, and Thomas E. Darcie



Copyright © 2012 Hindawi Publishing Corporation. All rights reserved.

This is a special issue published in "Advances in Optical Technologies." All articles are open access articles distributed under the Creative Commons Attribution License, which permits unrestricted use, distribution, and reproduction in any medium, provided the original work is properly cited.

Editorial Board

Mustafa A. G. Abushagur, USA
Partha P. Banerjee, USA
Ralph Barry Johnson, USA
Augusto Belendez, Spain
Steve Blair, USA
Maria Luisa Calvo, Spain
Pierre Chavel, France
Zhongping Chen, USA
Fu-Pen Chiang, USA
Petr Eliseev, USA
Michael A. Fiddy, USA
Patti Gillespie, USA

Richard B. Hoover, USA
Zoran Ikonc, UK
Saulius Juodkasis, Australia
Mark A. Kahan, USA
Alexander A. Kaminskii, Russia
Qiang Lin, China
Liren Liu, China
Qingming Luo, China
Daniel Malacara, Mexico
Mikhail Noginov, USA
Ci-Ling Pan, Taiwan
Markus Pessa, Finland

Giancarlo C. Righini, Italy
Joseph Rosen, Israel
José Luís Santos, Portugal
Colin J. R. Sheppard, Singapore
Kiyoshi Shimamura, Japan
Jagdish P. Singh, USA
Yinglin Song, China
Theo Tschudi, Germany
Leonid P. Yaroslavsky, Israel
Jianping Yin, China
Yong Zhao, China

Contents

Microwave Photonics, Borja Vidal, Nathan J. Gomes, Tadao Nagatsuma, and Thomas E. Darcie
Volume 2012, Article ID 206358, 1 page

Photonic Technologies for Millimeter- and Submillimeter-Wave Signals, B. Vidal, T. Nagatsuma, N. J. Gomes, and T. E. Darcie
Volume 2012, Article ID 925065, 18 pages

X-Cut LiNbO₃ Optical Modulators Using Gap-Embedded Patch-Antennas for Wireless-Over-Fiber Systems, Yusuf Nur Wijayanto, Hiroshi Murata, Tetsuya Kawanishi, and Yasuyuki Okamura
Volume 2012, Article ID 383212, 8 pages

Continuous Operation of a Bragg Diffraction Type Electrooptic Frequency Shifter at 16 GHz with 65% Efficiency, Shintaro Hisatake, Kenji Hattori, and Tadao Nagatsuma
Volume 2012, Article ID 676785, 6 pages

Photonic Heterodyne Pixel for Imaging Arrays at Microwave and MM-Wave Frequencies, Á. R. Criado, J. Montero-dePaz, C. de Dios, L. E. García, D. Segovia, and P. Acedo
Volume 2012, Article ID 792571, 7 pages

Fast Optical Beamforming Architectures for Satellite-Based Applications, B. Vidal, T. Mengual, and J. Martí
Volume 2012, Article ID 385409, 5 pages

Editorial

Microwave Photonics

Borja Vidal,¹ Nathan J. Gomes,² Tadao Nagatsuma,³ and Thomas E. Darcie⁴

¹*Nanophotonics Technology Center, Polytechnic University of Valencia, 46022 Valencia, Spain*

²*Broadband and Wireless Communications Group, University of Kent, Canterbury CT2 7NT, UK*

³*Department of Systems Innovation, Graduate School of Engineering Science, Osaka University, 1-1 Yamadaoka, Suita, Osaka 565-0871, Japan*

⁴*Department of Electrical and Computer Engineering, University of Victoria, Victoria, BC, Canada V8W 3P6*

Correspondence should be addressed to Borja Vidal, bvidal@dcom.upv.es

Received 22 October 2012; Accepted 22 October 2012

Copyright © 2012 Borja Vidal et al. This is an open access article distributed under the Creative Commons Attribution License, which permits unrestricted use, distribution, and reproduction in any medium, provided the original work is properly cited.

The continuous evolution of photonic technology in the last four decades has transformed the world allowing the development of the Internet, social networks, video on demand as well as considerable advances in medicine and industry. Photonic components can be also applied to the generation, transmission, and processing of microwave and millimeter-wave signals and benefit from the outstanding features of fiber optics. From early work in the late 70 s, this field, known as microwave photonics, has expanded considerably, producing a number of applications and attracting the interest of a wide range of researchers. These applications include radio-over-fiber links for mobile and satellite systems, remote feeding and control of microwave antennas, photonic-assisted analog-to-digital conversion, and systems and techniques for optical signal processing.

This special issue is intended to document some of the recent advances in the field. The contributions represent a diverse sample of current work on the field.

The paper entitled “*Photonic technologies for millimeter- and submillimeter-wave signals*” is a review paper presenting recent advances in the use of optical components for the generation, transmission, and processing of signals in the upper region of the millimeter-wave (beyond 30 GHz). This region of the radio spectrum is hardly used for practical applications due to the difficulty in dealing with signals of this frequency. However photonics can provide a feasible alternative for the applications in this band.

The paper entitled “*Photonic heterodyne pixel for imaging arrays at microwave and MM-wave frequencies*” presents a 3×3 imaging array based on a semiconductor optical amplifier heterodyne receiver.

The paper entitled “*Fast optical beamforming architectures for satellite-based applications*” compares several

architectures for fast optical beam forming of phased array antennas with particular application to space applications. Measurements of a fast beamformer without beam squint are provided between 4 and 8 GHz.

In the paper entitled “*X-Cut LiNbO₃ optical modulators using gap-embedded patch-antennas for wireless-over-fiber systems*,” an x-cut LiNbO₃ modulator integrated with gap-embedded patch-antennas is proposed for wireless-over-fiber applications. It showed an enhancement of 6 dB in comparison to z-cut LiTaO₃ devices.

Finally, “*Continuous operation of a Bragg diffraction type electrooptic frequency shifter at 16 GHz with 65% efficiency*” demonstrated for the first time the continuous operation of a Bragg diffraction waveguide-based electrooptic frequency shifter using a 16 GHz modulation signal. It provides an improved factor of 11 compared to a conventional bulk device.

The Guest Editors hope that this special issue will contribute to advance the research in this field as well as to the deployment of novel industrial applications for microwave photonic products. We thank the contributors for their report of significantly new results and the reviewers for their detailed evaluations that have strengthened the papers.

*Borjo Vidal
Nathan J. Gomes
Tadao Nagatsuma
Thomas E. Darcie*

Review Article

Photonic Technologies for Millimeter- and Submillimeter-Wave Signals

B. Vidal,¹ T. Nagatsuma,² N. J. Gomes,³ and T. E. Darcie⁴

¹*Nanophotonics Technology Center, Polytechnic University of Valencia, 46022 Valencia, Spain*

²*Department of Systems Innovation, Graduate School of Engineering Science, Osaka University, Osaka 565-0871, Japan*

³*Broadband and Wireless Communications Group, University of Kent, Canterbury CT2 7NT, UK*

⁴*Department of Electrical and Computer Engineering, University of Victoria, Victoria, BC, Canada V8W 3P6*

Correspondence should be addressed to B. Vidal, bvidal@dcop.upv.es

Received 24 July 2012; Accepted 9 September 2012

Academic Editor: Kiyoshi Shimamura

Copyright © 2012 B. Vidal et al. This is an open access article distributed under the Creative Commons Attribution License, which permits unrestricted use, distribution, and reproduction in any medium, provided the original work is properly cited.

Fiber optic components offer a competitive implementation for applications exploiting the millimeter-wave and THz regimes due to their capability for implementing broadband, compact, and cost-effective systems. In this paper, an outline of the latest technology developments and applications of fiber-optic-based technologies for the generation, transmission, and processing of high-frequency radio signals is provided.

1. Introduction

Optical fiber is an outstanding transmission medium which revolutionized data communications due to its unique combination of low loss and wide bandwidth [1]. Although originally targeted at long-distance communications, fiber optic technology has been applied to a wide range of fields, among them access networks, data centers, sensing, fiber lasers, illumination, imaging, and so forth. Another important, yet initially unforeseen, application for fiber optic technology was the interaction between optics and microwaves for applications such as radar, communications, warfare systems, and instrumentation. This area has become known as microwave photonics [2–6] and includes the photonic generation and distribution, processing, and monitoring of microwave signals, as well as photonic-assisted analog-to-digital conversion, to cite its main topics.

Features such as the low loss and wide bandwidth of fiber optic technology can be exploited to provide functions and capabilities to microwave systems that are very complex or even not implementable when carried out directly in the microwave domain. These advantageous characteristics are especially relevant when high frequency signals are considered given current limitations in the generation, processing,

and distribution of millimeter- and submillimeter-wave signals.

The millimeter-wave region of the electromagnetic spectrum (Figure 1), also called the extremely high frequency range, (EHF), corresponds to radiofrequencies from 30 GHz to 300 GHz (i.e., wavelengths from 10 mm to 1 mm). The high frequency of the signals in this band as well as their propagation characteristics makes them useful for a variety of applications. However, the difficulty in generating and detecting signals as well as atmospheric attenuation in this band limits current applications. Existing applications include data transmission (high-bit rate wireless access networks), and radar (mainly benefiting from the beam width achievable with small antennas in applications such as short range automotive radars at 77 GHz as well as in scientific, military, security controls, and range and speed measurement for industrial applications).

Beyond the millimeter-wave band, and below infrared frequencies, there is a gap in the spectrum where the historic difficulties in generating and detecting signals have prevented the development of applications. This still little used frequency band is known as the submillimeter-wave band, far-infrared, or terahertz band, corresponding to radiofrequencies from 300 GHz to 3 THz (i.e., wavelengths

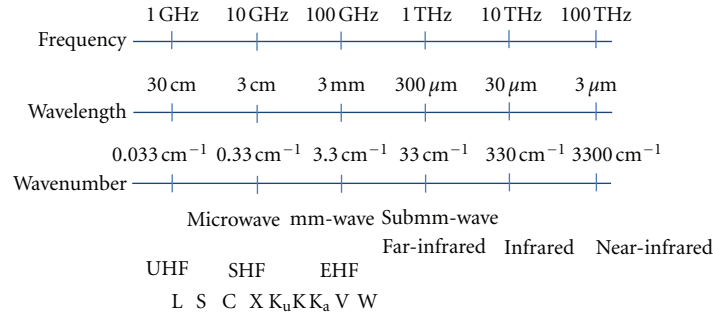


FIGURE 1: Electromagnetic spectrum and common band names.

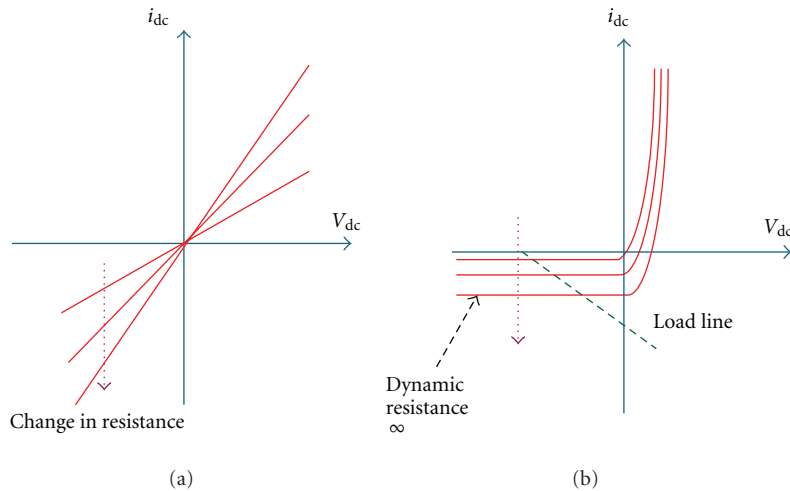


FIGURE 2: Typical dc I-V characteristics of (a) photoconductors and (b) photodiodes.

from 1 mm to 100 μm). Terahertz radiation has been long studied in fields such as astronomy and analytical science. However, recent technological innovations in photonics, electronics, and nanotechnology are resulting in a wide range of breakthroughs which have pushed THz research into the center stage [7–12].

In this paper, we explore and discuss several technologies, systems, and applications where fiber optic technology is showing competitive features in comparison to its electronic counterparts and is helping to widen the range of applications exploiting these frequency bands. The paper is organized as follows. Section 2 describes high bandwidth detectors and waveguides for the photonic generation of high-frequency signals. These are key components in implementing efficient fiber optic systems at millimeter- and submillimeter-wave frequencies. Section 3 is devoted to the application of fiber optic technology for data transmission and Section 4 to the exploitation of the submillimeter band by means of time and frequency spectroscopy. Finally, a conclusion is provided in Section 5.

2. Components

2.1. Photoconductors and Photodiodes for THz Generation and Detection. Photonic techniques have been essential in

developing THz technologies with respect to signal generation and detection. The most fundamental and widely used devices are based on the optical-to-THz or THz-to-optical conversion using interaction media such as nonlinear optical (NLO) materials, photoconductors, and photodiodes. Typical NLO materials are crystals with large nonlinear susceptibility such as CdTe, ZnTe, GaP, LiNbO₃, and DAST (4-dimethylamino-N-methyl-4-stilbazolium tosylate). Such materials offer the widest bandwidth in the signal generation and detection and the highest peak-power generation [13, 14]. There are no metallic electrodes nor antennas for NLO materials. However, because of their low conversion efficiency, NLO materials require intense illumination of light, which makes it difficult to introduce optical-fiber cables; THz systems with NLO materials are mostly based on free-space optics. Thus, in this section, we address photoconductor and photodiodes suitable for fiber-optic system applications.

Figure 2 shows typical dc current-voltage characteristics of a photoconductor and a photodiode, showing the change in the current-voltage curve under the illumination of infrared (IR) and visible light. The photoconductor is a conducting element whose conductance is controlled by the incident light. The response speed or the frequency bandwidth of the photoconductor is determined by the

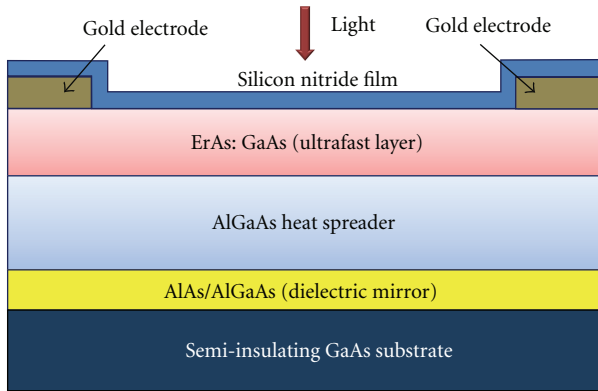


FIGURE 3: Example of layer structures for high-power GaAs-based photoconductors.

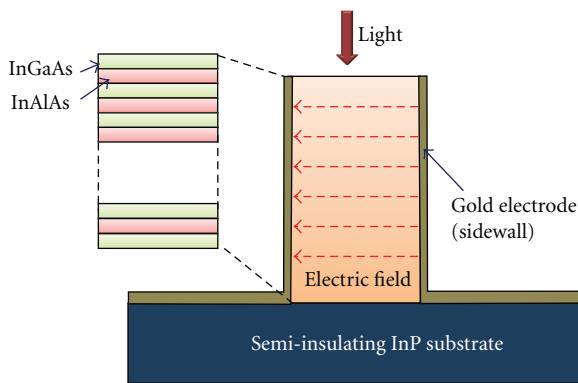


FIGURE 4: Example of device structures for high-power InGaAs-based photoconductors.

photogenerated carrier transit time and/or the carrier recombination time. To decrease the former time constant, there are two approaches; one is to reduce the gap distance between electrodes by deep-submicron lithography and the other is to apply a stronger electric field or voltage across the gap. In addition, an interdigitated finger structure can be introduced for the electrodes to ensure the sensitivity. In order to efficiently emit/receive THz waves into/from free space, the electrodes are directly integrated with planar antennas such as dipole, log-periodic, bow-tie, or spiral antennas.

The choice of photoconductive materials has been long studied since their first application for picosecond switching in the 1970's. Primary materials are low-temperature grown (LTG) GaAs and ErAs: GaAs (i.e., nanoparticles embedded in a GaAs matrix) for visible wavelength (700~800 nm) lasers (Figure 3). Heat spreading layers made of AlGaAs together with dielectric mirror layers have successfully been introduced to further enhance the THz emission and conversion efficiency [15]. For telecom wavelength (1550 nm) lasers, LTG InGaAs, ErAs: InGaAs, Br-irradiated InGaAs, Fe-ion-implanted InGaAs, and LT-InGaAs/InAlAs have been studied. Figure 4 shows a mesa-type LT-InGaAs/InAlAs structure with electrical side contacts, which improves the

output power of the emitter as well as the sensitivity of the receiver [16]. One of the issues of InGaAs-related materials is low resistivity or high dark conductivity compared to GaAs materials. Detailed references and other photoconductive materials particularly used for spectroscopy applications are described in Section 4.1.

Photoconductors are used for both pulsed and CW THz sources as well as detectors, while photodiodes are more suitable for CW generation in terms of output power. In CW THz generation, two lightwaves with different wavelengths are injected onto the photoconductors or photodiodes. This technique is usually referred to as "photomixing." In contrast to the continuous evolution of photoconductors since the 1970's, studies on high-frequency photodiodes accelerated in the 1990's, mainly because of increasing demands in broadband receivers in fiber-optic communications systems [17]. There have been many approaches to enhance photodiode performances with respect to structure design, carrier transport design, and circuit design. Regarding the structure design, conventional surface-illuminated photodiodes have evolved as shown in Figure 5 [10]. In order to enhance the efficiency of the back-illuminated photodiode, a refracting facet structure was introduced to enable edge-illumination; it also contributes to ease of packaging and eases optical alignment. Other types of edge-illuminated photodiodes are waveguide structures, periodically loaded traveling-wave (TW) structures integrated with optical waveguides, and evanescently coupled TW waveguide structures. These approaches offer both high efficiency and large bandwidth.

By considering the carrier dynamics in the photodiode, several types of layer structures and materials have been proposed starting from the conventional pin photodiode (a) as illustrated in Figure 6. These are referred to as the untravelling-carrier photodiode (UTC-PD) (b), dual depletion pin PD (c), partially doped absorber PD (d), and modified UTC-PD, which is a composite of the UTC-PD and the dual depletion pin PD (e).

The third method to enhance the bandwidth and/or output power is a resonant operation of the back-illuminated "lumped" photodiode. This technique compensates for the internal capacitance of the photodiode, thus eliminating the constraint of CR time constant at a specific frequency. The addition of a matching element, such as a short-stub, to the photodiode was proven to increase the output power by 2-3 dB at the resonant frequency. Integration of a resonant planar antenna with the photodiode is also effective, in particular for THz regions.

Figure 7 shows a comparison of reported continuous millimeter- and THz-wave output power (detected) against operating frequency for UTC-PDs, pin-PDs, and low-temperature-grown (LT)-GaAs photomixers. The output power of UTC-PDs is about two orders of magnitude higher than those of pin-PDs, mostly due to high saturation output current. The output power decreases in proportion to f^{-4} .

To overcome the limitation of the power capacity in a single device, the power combining technique using an array of photodiodes is promising to increase the output power by one order of magnitude. There are two methods of power combining; one uses an electrical power combiner circuit,

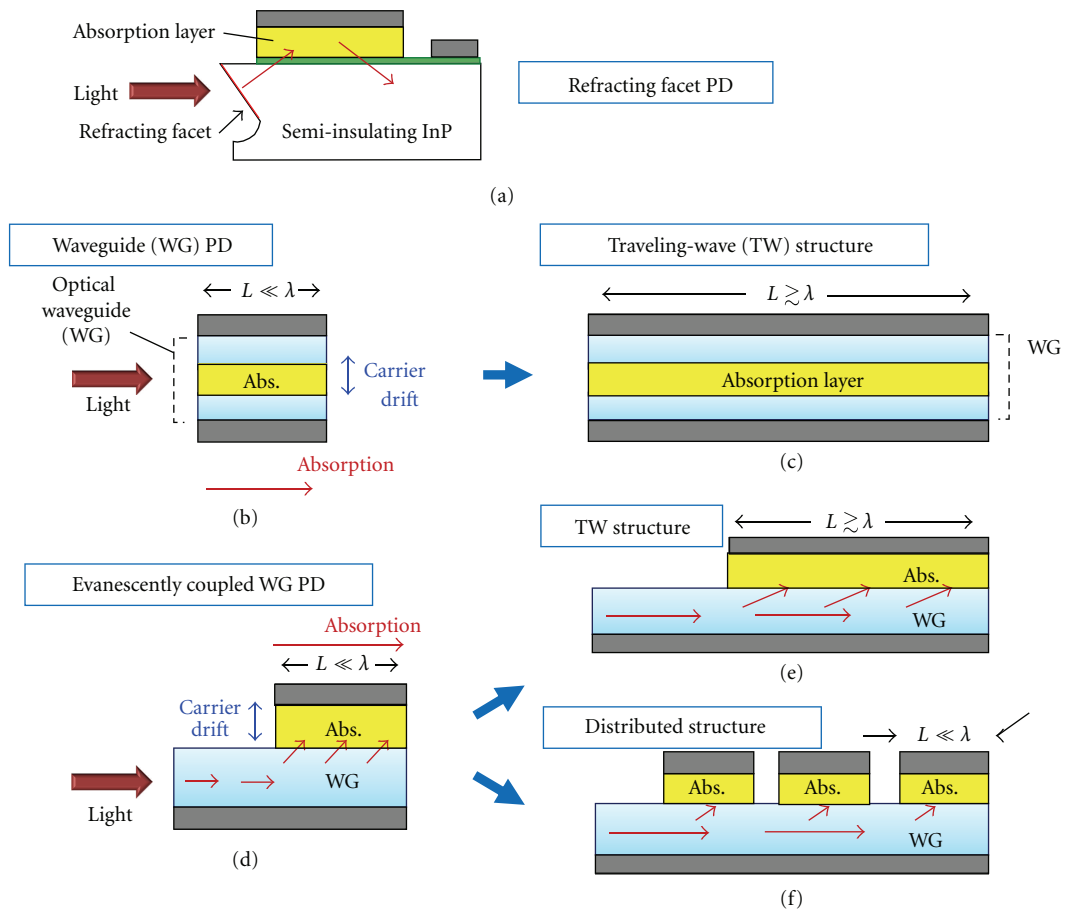


FIGURE 5: Structures of edge-illuminated photodiodes.

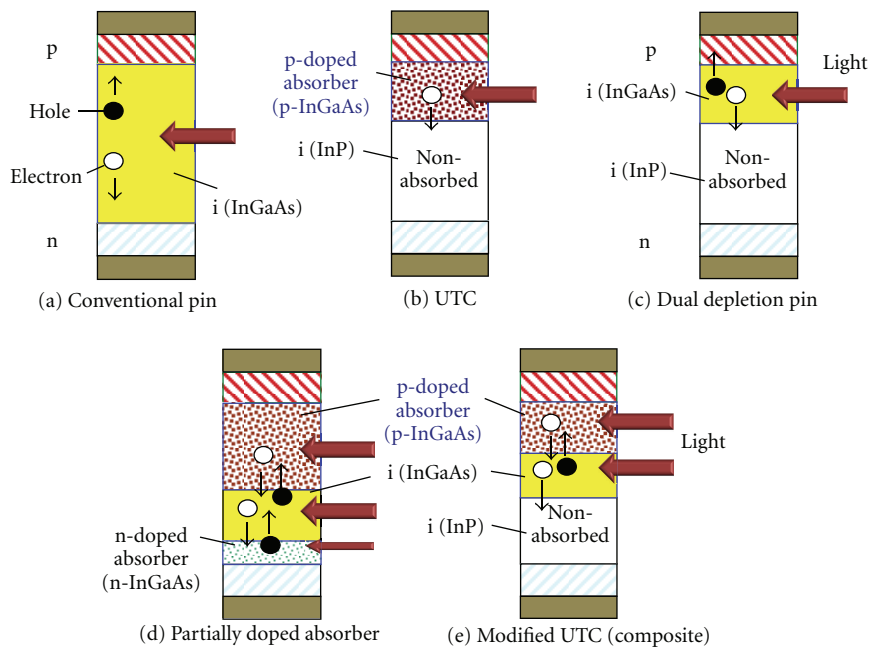


FIGURE 6: Layer structures of high-power and high-frequency photodiodes.

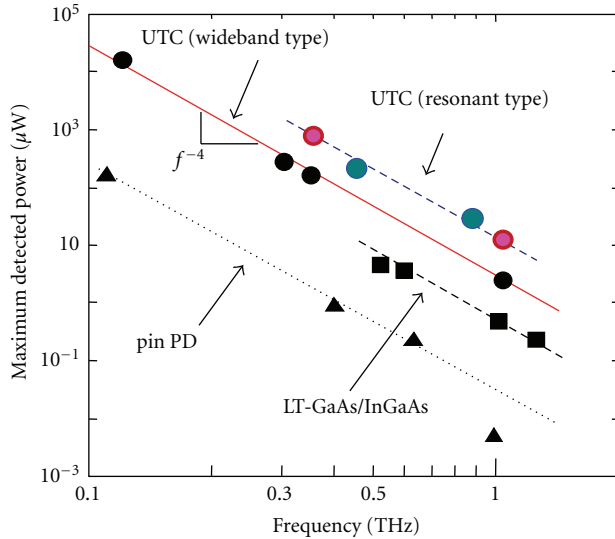


FIGURE 7: Comparison of CW output power from photodiodes and photoconductors.

and the other is based on spatial power combination using an array of antennas; both methods have been examined, as shown in Figure 8 [18, 19], achieving more than 1 mW at 300 GHz.

In addition to continuous-wave signal generation using photodiodes, there have been recently several studies on the application of photodiodes for THz heterodyne/homodyne detectors by making use of their nonlinearity [20, 21].

2.2. Low-Loss Waveguides for THz. While source and detector technologies continue to advance, considerable improvement is also needed in passive components before THz measurement and instrumentation is as economically accessible, easy to use, and high in performance as existing technology operating at lower (microwave) or higher (optical) frequencies. A large number of THz applications and instruments continue to emerge, but widespread exploitation of THz technology requires substantial improvements in both form and function. A simple example is a single-frequency source connected through a device under test to a spectrum (power spectrum) or network (S-parameters) analyzer. At microwave frequencies, precision sources are easily connected through inexpensive cables to easy-to-use analyzers. At optical frequencies, diode lasers, optical fiber, fiber-based passive and active components, and low-noise receivers provide similar efficacy. However, at THz frequencies, this simple configuration remains a research challenge involving specialized lasers, optical and THz beam alignments, and sampling delay lines. Existing technology does not easily or affordably allow the generation of a specified frequency, and passive components such as cables, connectors, couplers, filters, and circulators do not exist.

A significant first step is to develop components and systems in which THz waves are entirely confined within waveguide or transmission-line structures, rather than radiating as free-space beams as is typically done in today's systems. This

has motivated considerable research on waveguide or transmission line technology for THz applications. Two broad categories of activity in THz waveguides include (1) THz “cable”—a low-loss nondispersive interconnection between various THz components or instruments over bench-top distances (>10 cm), and (2) THz on-chip interconnect—a planar interconnection between small active devices (transistors, photomixers, mixers, etc.) over on-chip distances (<1 cm) in a THz component. In what follows, we review work in both these areas. Also, since desirable solutions for these two applications differ substantially, we describe adaptation methods using mode-converter components.

Many types of waveguides have been evaluated for THz applications over the last decade including various configurations of planar, dielectric, and metallic structures. Early work with coplanar transmission lines [22] suffered from high loss (20 cm^{-1}). Conventional rectangular or circular metallic waveguide has been downsized for use at THz frequencies (e.g., [23]). While loss can be low, application is limited by difficulties in fabrication, coupling from/to THz emitters/detectors, and the highly dispersive propagation of broadband radiation used commonly in pulsed time-domain THz systems. Dispersion also limits dielectric waveguides fabricated with polyethylene [24, 25] or sapphire [26]. Very low loss (0.03 cm^{-1}) was demonstrated using the radially polarized mode supported by a bare wire [27, 28]. However, coupling to this radial mode is difficult [29], and the resulting structure lacks practical compatibility with many applications.

2.2.1. THz “Cable”. For dispersion-free TEM-mode propagation, parallel-plate waveguide [30] and two-wire waveguide [31–33] offer extremely low loss ($<0.01\text{ dB/cm}$). Unlike a coaxial cable, both structures support a mode profile that matches well to the field emitted from typical THz sources. The strong confinement of the field between the conductors enables low bend loss [34] while the geometry can be optimized to suit a variety of objectives trading off loss for confinement. Either of these structures provides a suitable basis for low-loss guided-wave bench-top THz interconnections.

We studied the 2-wire waveguide in detail to understand loss [32] and coupling [33]. Analysis using conformal mapping shows the dependence of conductor loss on wire radius R and center-center separation D for gold wires, as shown in Figure 9. For radii greater than roughly $200\text{ }\mu\text{m}$ and separations greater than $1500\text{ }\mu\text{m}$, conductor loss is less than 0.01 cm^{-1} . Under these conditions, the field is broadly distributed throughout the space surrounding the wires. Alternatively, for close wire spacing, the field is concentrated in a small region between the wires and loss increases.

To make a practical waveguide or cable, a suitable mechanical structure must be devised to support the parallel wires with good mechanical stability and low loss. Extending common practice in high performance microwave cables, low-density foam has been shown to provide excellent characteristics at THz frequencies. As shown in [35], rigid polymethacrylimide (PMI) foam has permittivity of

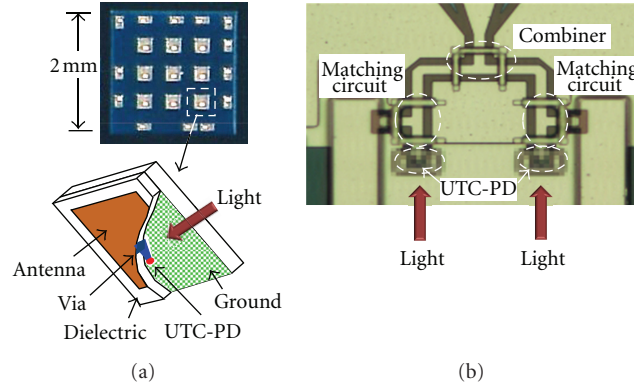


FIGURE 8: Power combining techniques with photodiode arrays by (a) spatial power combiner and (b) electrical power combiner.

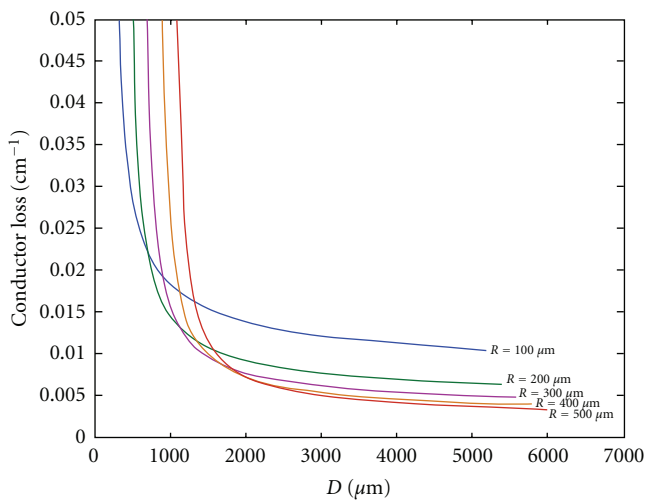


FIGURE 9: Dependence of conductor loss on wire radius R and center-center separation D for two-wire waveguide using gold wires at 1 THz.

only 1.03 and a loss tangent of $<0.5\%$. Our recent results with a test THz “cable,” formed using PMI as shown in Figure 10 to stabilize the wires, suggest that total loss as low as 0.02 cm^{-1} can be achieved at 1 THz. Dielectric loss was minimized by using periodic PMI supports over only 10% of the length of the structure.

2.2.2. THz On-Chip Interconnect. Planar structures using variants of microstrips, striplines, or coplanar lines are popular at microwave frequencies for ease of fabrication and general utility, but generally have high conductor and dielectric loss and suffer from shock-wave radiation loss [36] at higher frequencies. The latter has been reduced using suspended membrane structures [37] to prevent the propagating mode from being drawn into the substrate, but these are useful only over very short distances and are challenging to fabricate.

We have recently explored methods to reduce this radiation loss using either a symmetric cap layer or a photonic band gap structure [38]. As shown in Figure 11,

we begin with a slot-line structure, which is easy to fabricate highly compatible with photoconductive THz devices and offers good heat dissipation. The basic slot-line structure (a) offers the easiest solution, but loss is high. The addition of a symmetric cap layer (b) prevents loss into the substrate, but limits access to the surface of the chip for component mounting, optical pumping, or electrical connections. Alternatively, the photonic band gap structure (c) provides a simple way to prevent this loss into the substrate, with only minor complication in the design of the substrate. However, this approach introduces frequency dependence in propagation.

These structures have been studied in detail, using conformal mapping and numerical simulation [38], providing several general conclusions. First, since the skin depth for gold at 1 THz is less than 80 nm, conductor loss becomes independent of conductor thickness for thickness greater than roughly 100 nm. Second, for slot widths greater than roughly $5 \mu\text{m}$, conductor loss becomes independent of slot width. For thinner conductors or slots, conductor loss increases rapidly. Third, both structures can essentially eliminate radiation loss, leaving conductor loss of less than roughly 3 cm^{-1} . Adding the dielectric loss, for example using crystalline high-resistivity GaAs with loss of 0.5 cm^{-1} at 1 THz [39], gives a total loss of roughly 3.5 cm^{-1} .

2.2.3. Mode Converters. As seen in the preceding sections, the requirements and performance of transmission lines for a bench-top application differ substantially from those for on-chip interconnection. Clearly two-wire waveguide is not compatible with on-chip circuits and devices, and the loss associated with on-chip transmission lines, roughly 100 times greater than the loss for the two-wire waveguide, is unacceptable for bench-top applications. Obviously, then both technologies are needed, as is a mode converter to transition between one and the other.

Mode converters or adiabatic tapers are commonplace in optical and microwave systems. In optical systems, many papers have been published for applications in laser-to-fiber coupling, integrated optics, couplers, and photonic crystal fibers. The classic example at microwave frequencies is the

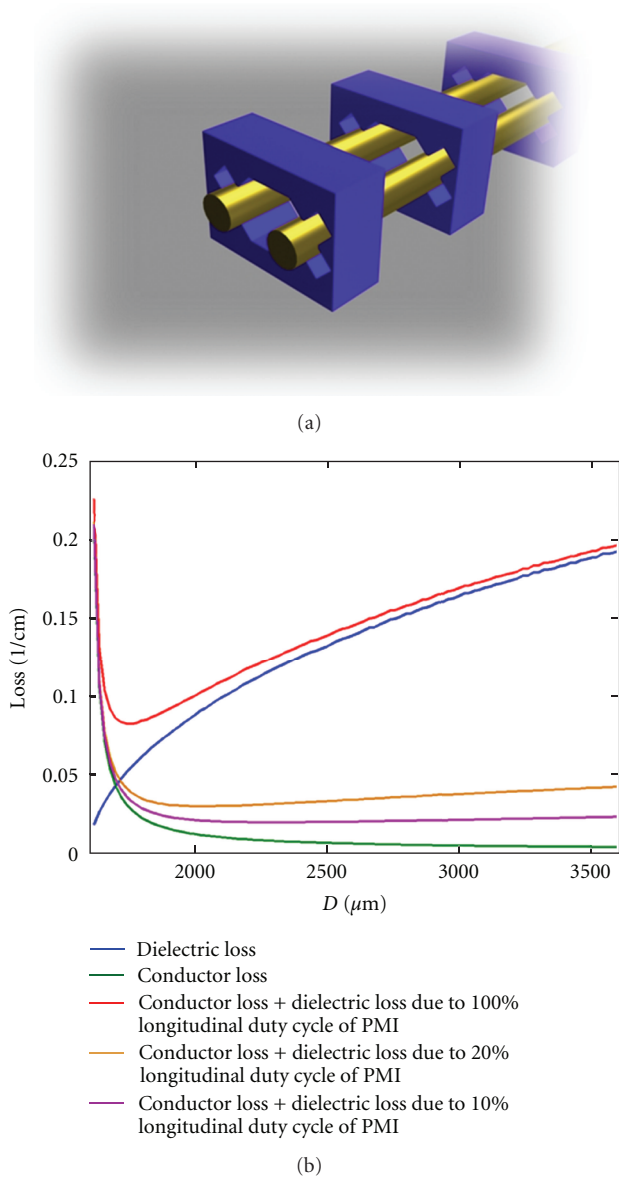


FIGURE 10: (a) THz cable based on two-wire waveguide with structural PMI blocks located periodically along the length. (b) Predicted performance at 1 THz for 400 μm radii wires with center-center separation D showing dielectric loss (blue), conductor loss (green), conductor loss plus dielectric loss due to 100% PMI along length (red), 20% (orange), and 10% PMI (purple).

horn antenna. The challenge is to design a structure that is simple to fabricate and provides a gradual transition between different modes while minimizing loss and reflection.

Using a mode-matching transmission-matrix approach, we studied slot-line to two-wire waveguide tapers as shown in the inset of Figure 12 [40]. Results show that this simple planar device can provide high throughput and low return loss at lengths less than 1 mm. Since conductor loss tends to be important only for the small slot widths that exist at the beginning of the taper, conductor loss tends to be small.

Performance is then limited by dielectric loss. Hence it is essential to minimize the taper length and convert to a low-permittivity support structure for the two-wire waveguide as quickly as possible.

3. Communication Links

Frequency bands beyond 30 GHz are not regulated in most countries. Given the current saturation of the radio spectrum at lower bands due to thriving wireless broadband applications, there is a strong pressure toward the exploitation of new spectral regions.

3.1. Millimeter-Wave over Fiber Communications Systems.

Research into millimeter-wave (mm-wave) over fiber communication systems is of interest for the support of mm-wave communications, generally, where, as was stated in Introduction, the large available spectrum can make possible ultra high-data-rate communications. The high path loss and lack of penetration through solid objects can also be made beneficial, as it can lead to well-defined cells in cellular systems. The loss experienced in electrical cables at such frequencies makes fiber transport an even more attractive proposition than at lower, microwave frequencies. However, the generation, transport, and detection of mm-wave modulated optical signals is not straightforward. Transport will be more affected by fiber dispersion as the mm-wave modulation frequency increases. Detection will require sensitive photodiodes with sufficient bandwidth and, for high-performance links, with high power-handling capability, as was shown in Figure 7, and discussed in Section 2.1. Generation requires specialized modulator configurations and/or optical generation techniques (such as optical heterodyning) due to the bandwidth limitations of optical transmitters and the need to reduce the fiber chromatic dispersion. These issues are discussed in the following subsections, followed by a brief review of mm-wave over fiber communications system architectures.

3.1.1. Fiber Transport.

Although multimode fiber has been used in mm-wave over fiber systems, using techniques such as IF transmission with remote mm-wave upconversion [41], remote heterodyne detection [42] or optical frequency multiplication [43], the higher (modal) dispersion and the incompatibility of the fiber core diameter with high-speed photodiodes, have meant that most research has focussed on single-mode fiber transport. Then, it is the chromatic dispersion which poses the most significant limitation. The different phase retardations of the spectral components from the mm-wave modulation caused by the fiber dispersion results in fading of the received signal [44]; in order to overcome this, modulation or optical techniques for mm-wave generation which result in only two spectral components are necessary. Then, the different phase retardations cause phase variations of the generated mm-wave signal, but not fading. As mm-wave over fiber is an analog technique, generally large received signals are required compared to

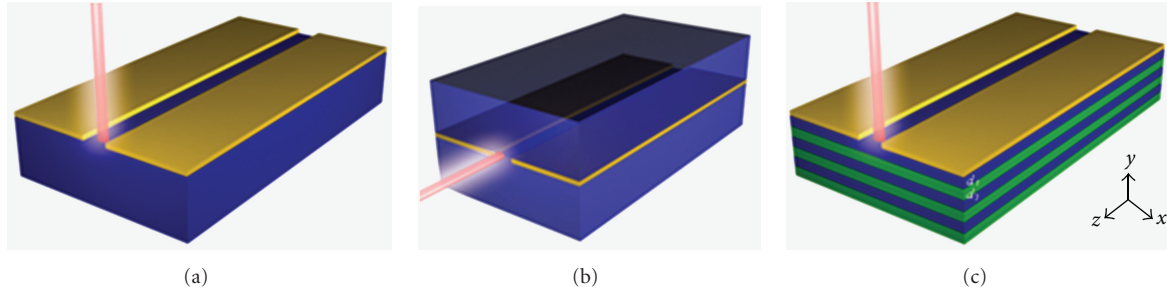


FIGURE 11: Conventional slot-line waveguide on photoconductive substrate with normal optical pump illumination, (b) edge-pumped slot-line in a homogeneous medium, and (c) slot-line on a layered substrate.

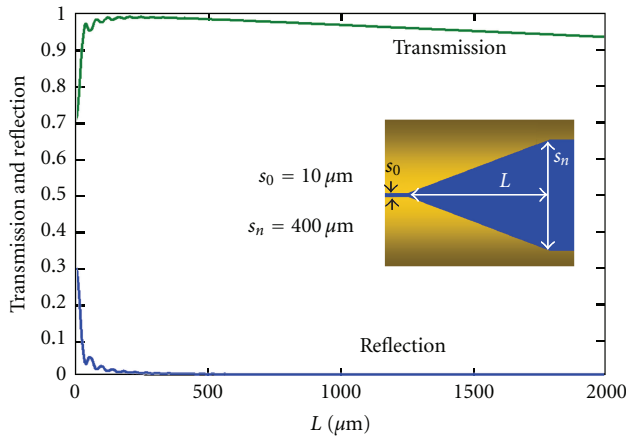


FIGURE 12: Transmission and reflection coefficients at 1 THz for a slot-line-based tapered structure versus L , the length of the taper, with dielectric loss = 0.5 cm^{-1} .

digital transmission; for high-performance links where optical signal levels may need to be high, or for the transport of multiple signals, fiber nonlinear effects may become significant [45].

3.1.2. Millimeter-Wave Generation. As stated in Section 3.1.1, optical generation techniques for mm-wave over fiber systems generate two optical spectral components, separated by the desired mm-wave frequency. Such schemes can be thought of as modulation-based, where the modulator setup and/or subsequent filters suppress the undesired spectral component(s)—these are referred to as optical single-sideband (OSSB) or optical double-sideband suppressed-carrier (ODSB-SC)—or as phase-/frequency-locking based, where separate optical components are locked together. The phase/frequency locking is important because tunable optical sources such as semiconductor lasers have broad linewidth in microwave terms, and this linewidth would appear on the resultant mm-wave signal if the noise sources causing it in the individual optical spectral components were not correlated.

Simple Mach-Zehnder modulators (MZMs) can be used in mm-wave generation [46, 47]. Biasing the modulator at its

null point suppresses the carrier and generates a mm-wave frequency double that of the input microwave/mm-wave frequency [46], see Figure 13(a). The method requires good control of the operating point for the carrier suppression and is limited by the bandwidth of available modulators. Frequency quadrupling is possible by biasing the MZM at its maximum transmission point and removing the carrier using a fixed optical filter [47], see Figure 13(b). Once optical filtering is considered, phase modulators may offer greater flexibility in generating the higher-order optical sidebands, which can be selected from for generating the desired mm-wave frequency [48–50] see Figure 13(c).

Conceptually, the simplest method for optically generating a mm-wave signal through the phase-locking technique is through an optical phase-locked loop which locks together two semiconductor lasers [51]. As shown in Figure 14(a), to remove the requirement for a mm-wave reference source, the locking can be done at a harmonic of the reference frequency. However, a major practical limitation is the requirement for the feedback loop delay to be much less than the timescales over which phase and frequency fluctuations occur [52]. Optical injection-locking can be performed by locking two optical sources to signals from the same reference—for example, different higher-order sidebands of the same frequency-modulated laser as shown in Figure 14(b). Here the limitation is the precise control over the laser wavelengths that is required, as locking bandwidths are typically narrow in optical terms. However, this control is possible with OPLLs, so a combination of the two techniques has been shown to be very effective [53].

Generating the optical components in a single laser source is also attractive, as the spectral lines can be locked through mechanisms such as mode-locking. Dual-mode lasers were first demonstrated for this purpose by Wake et al. (see, for example, [54]), while recently work has gone into making their behaviour more stable and predictable [55].

3.1.3. Photodetection. Small-area photodiodes can minimize capacitance and lead to possibilities for mm-wave operation, but waveguide devices enable some decoupling of the problems of collecting the photons for efficient operation and minimising the carrier transit times and device capacitance

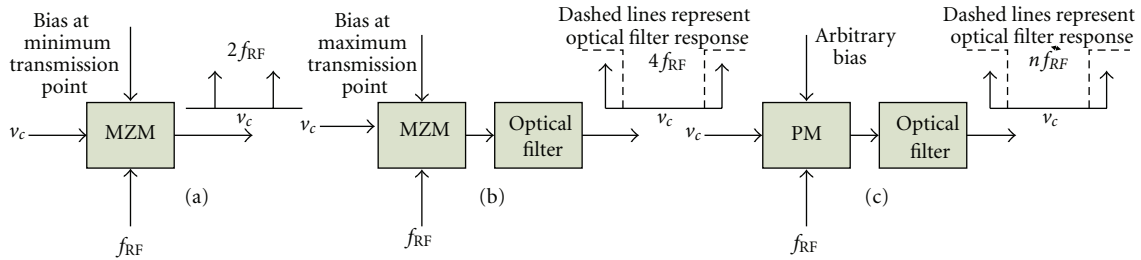


FIGURE 13: Millimeter-wave generation using external optical modulators: (a) frequency-doubling using a Mach-Zehnder modulator (MZM) biased at its minimum transmission point; (b) frequency-quadrupling using a MZM biased at its maximum transmission point and filtering out the optical carrier; (c) frequency n -tupling using a phase modulator and selecting appropriate sidebands.

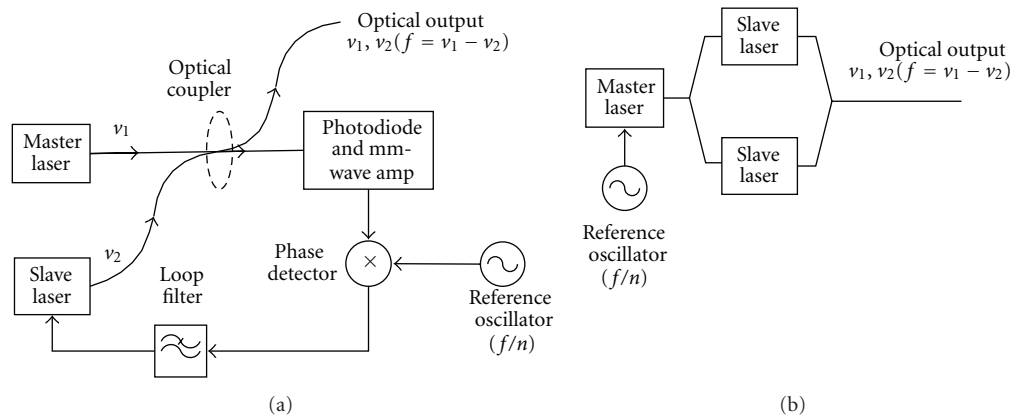


FIGURE 14: Millimeter-wave generation through optical heterodyning: (a) using an optical phase-locked loop (OPLL); (b) using optical sideband injection-locking.

[17]. Operation at telecommunication wavelengths with waveguide photodiodes enables the use of low-loss optical fiber for the delivery of the mm-wave signals, and such devices have been demonstrated up to over 600 GHz [56]. For mm-wave over fiber communications, however, system dynamic range is an important consideration and this is improved through operation at higher optical power levels, as will be discussed in the following subsection. Uni-traveling carrier (UTC) photodiodes, as we shown in Figure 6, have become key devices in high-speed and high-power operation.

3.1.4. Millimeter-Wave over Fiber Link Performance. As an analog link, a millimeter-wave over fiber link is characterised by gain and noise figure in its linear region, and by a dynamic range, referring to the range of signal powers that can be handled between a noise limited low end and a distortion limit at the high end. In externally modulated optical links, high optical power levels lead to higher link gains [57]; even in directly-modulated links, higher optical powers will lead to operation in a transmitter-noise-limited regime, generally resulting in lower link noise figure. It is for such reasons that UTC photodiodes have become of interest in high-performance millimetre-wave over fiber links.

Distortion, as in analog optical links generally, is mainly due to the optical transmitter—the laser or external modulator nonlinearity—although at very high optical power

levels (perhaps, 10 mW and above) fiber and photodiode nonlinearity can be significant. In links where MZM-type external modulators are used to apply the data-carrying modulation to the mm-wave signal, optimization of the bias can trade off the limitations arising from distortion and noise [58].

Today, many wireless systems use higher-level, quadrature amplitude modulation (QAM) schemes to maximise the use of available bandwidth. In some cases, the QAM is applied to an orthogonal frequency-division multiplexed (OFDM) signal, which alleviates multipath and intersymbol interference effects in the wireless channel. OFDM in the optical domain may offer some resilience to fiber dispersion effects, too [59]. In general, however, these advantages must be traded against the higher peak-to-average power ratio (PAPR) obtained with OFDM and multicarrier transmission, which leads to more significant signal degradation through nonlinear effects. With QAM signals, it is common to measure performance in terms of the error vector magnitude (EVM)—a ratio of the mean error power against the mean peak signal power, measured at the outermost signal constellation point. In a noise-limited regime, at least, EVM can be directly related to signal-to-noise ratio (SNR) [60]. Different wireless systems will express performance requirements as EVM (%) for given QAM-levels; it is important to note that for radio over fiber (including mm-wave over fiber) downlink performance, it is the more stringent transmitter

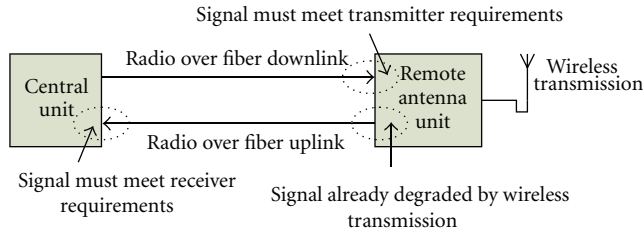


FIGURE 15: Radio (millimeter-wave) over fiber link performance characterization: the radio over fiber link is generally part of a larger system, and measurements must be compared to appropriate transmitter and receiver requirements.

EVM requirement that is important. This measurement against different transmitter and receiver requirements is illustrated in Figure 15. While EVM is often used to express the performance requirements against in-band noise and distortion, the optical link noise and distortion together with amplification in the antenna unit will also cause emissions out-of-band, and these must be controlled within spectral mask and adjacent channel power leakage limits.

3.1.5. Millimeter-Wave over Fiber System Architectures. For communications applications, the transport of the mm-wave signals over fiber is often necessary for connecting networks of distributed or remote antenna sites. Different fiber topologies have been proposed. For example, a star/tree topology, with space-division multiplexing (SDM) in the form of multifiber cables to distribution points, wavelength-division multiplexing (WDM), and subcarrier multiplexing (SCM) for smaller areas and individual antennas was proposed in [61]. The possible use of multimode fiber for in-building distribution was also accounted for. Ring and bus fiber topologies have also been proposed [62, 63], with the use of a secondary ring for protection against failures proposed in [64].

For the mm-wave signal transport, some proposals have examined transmission using baseband or IF signals with up-conversion to the mm-wave frequency, or downconversion from the mm-wave frequency, taking place at the remote unit [41, 65]. This has been particularly suggested for the uplink direction [65]. Experimental demonstrations of very high-bit-rate mm-wave signals over fiber have been performed [66]; those which have included a wireless link have shown the possibility for such fiber links to replace or extend point-to-point mm-wave links (e.g., for the backhaul of mobile systems) [67]. Other experiments have demonstrated the possibility of wireless local area network-type coverage over small areas using the mm-wave frequency bands [68].

3.2. THz Communications Based on Photonic Technology. Recently, there has been an increasing interest in the application of THz waves to wireless communications [69–71]. This is because frequency bands above 275 GHz have not yet been allocated to specific active services, and there is a possibility to employ extremely large bandwidths for ultrabroadband wireless communications. In particular, the 300–500-GHz

range is considered to be rather realistic since enabling semiconductor electronic and photonic devices operating at this frequency range have recently started to become available. From the viewpoint of atmospheric attenuation of electromagnetic waves, 500 GHz is nearly an upper limit in “last-one-mile” applications.

In order to examine the wireless link using 300–500-GHz carrier frequencies, the use of “photonics” is practical and powerful because of large its bandwidth in the signal generation and modulation [72, 73].

Figure 16 shows a block diagram of a short-distance (~0.5 m) wireless link using a photonics-based transmitter. First, an optical THz-wave signal is generated by heterodyning the two wavelengths of light from the wavelength-tunable light sources. The optical signal is digitally modulated by the optical intensity modulator driven by the pulse pattern generator (PPG). Finally, the optical signal is converted to an electrical signal by a uni-traveling-carrier-photodiode (UTC-PD) and is emitted into free space via a horn antenna with a gain of 25 dBi. The emitted terahertz wave is well collimated by a 2-inch-diameter Teflon lens. The total antenna gain is about 40 dBi. Main features of this photonic approach are that the carrier frequency is widely tunable, and that the modulation frequency can be increased to at least 40 Gbit/s.

The receiver consists of a Schottky barrier diode (SBD) followed by a low-noise preamplifier and a limiting amplifier. The envelope detection is performed by the SBD for the ASK (OOK) modulation. The frequency dependence of the output power from the UTC-PD module is shown in Figure 17. The 3-dB bandwidth is 140 GHz (from 270 to 410 GHz). The peak output power was $110 \mu\text{W}$ at 380 GHz for a photocurrent of 10 mA with a bias voltage of 1.1 V. The output power could be further increased to over $500 \mu\text{W}$ with increasing the photocurrent up to 20 mA with responsivity of 0.22 A/W [74]. The SBD detector has almost the same bandwidth of over 100 GHz.

Figure 18 shows bit-error-rate (BER) characteristics at 12.5 Gbit/s with a carrier frequency of 300 GHz. The horizontal axis is the photocurrent of the transmitter. An error-free transmission at 12.5 Gbit/s has been achieved with 4-mA current, which corresponds to the transmitter output of around $10 \mu\text{W}$. Currently, IF (baseband) bandwidth for demodulated signals in the receiver is as narrow as 18 GHz, which leads to the maximum bit rate of around 25 Gbit/s. Figure 18(c) shows an eye diagram of the received/demodulated signals at 24 Gbit/s. The eye is clear and open, which shows an error-free transmission.

Future challenges should address the increase of the receiver bandwidth towards 40-Gbit/s transmission and the integration of photonic components into a one-chip transmitter consisting of lasers, modulators, photodiodes, and antennas [75, 76].

4. Spectroscopy

The submillimeter-wave (Terahertz) electromagnetic spectrum hosts a wide range of complex interactions between

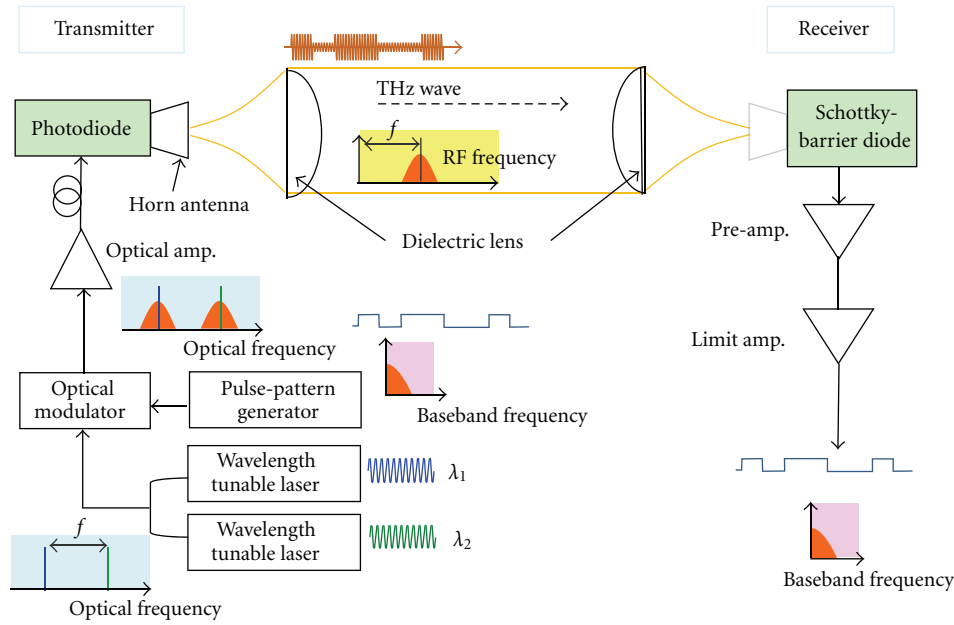


FIGURE 16: Schematic diagram of a 300-GHz band wireless link using photonics-based transmitter.

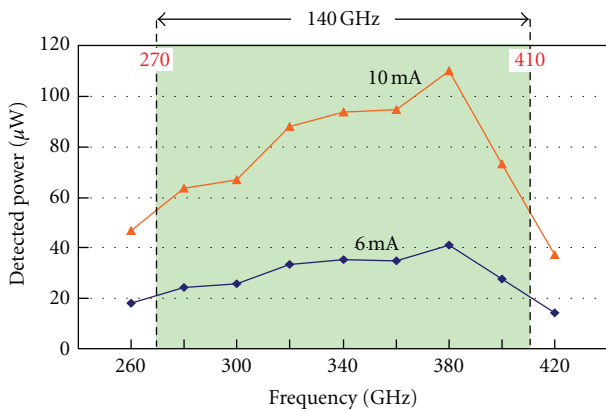


FIGURE 17: Typical frequency dependence of the output power from UTC-PDs.

radiation and matter that can be used to achieve innovative sensing and imaging systems. Low-energy interactions in a wide range of materials can be studied with spectroscopy in the THz range. Spectroscopic analysis in this band started with the development of Fourier Transform Infrared (FTIR) Spectroscopy in the 50s [77]. Further developments in the last decades have resulted in alternative techniques to exploit this area of the electromagnetic spectrum.

THz spectroscopic techniques are often far superior to conventional tools for analyzing a wide variety of materials [8]. Additionally, terahertz waves are nonionizing and transparent through many materials that are opaque in visible and IR light while many other materials present characteristic spectroscopic fingerprints in this area of the spectrum. Finally, wavelengths are short enough to give adequate spatial resolution for imaging or localization of

threat objects allowing spectroscopic imaging. The recent development of new sources and detectors jointly with the capability to probe fundamental physical interactions in this, previously inaccessible, spectral range has attracted considerable interest into the field of submillimeter, or THz, spectroscopy [11, 12].

Thus, THz spectroscopy has been applied to a wide range of fields with, for the moment, heterogeneous evolution to market exploitation.

- (i) *Material science.* There are a wide range of optical resonances in molecular crystals within the THz band given by the complicated interplay between intra- and intermolecular forces. In recent years, the spectroscopic analysis of polyatomic crystals, and especially crystals of organic molecules, have attracted considerable interest for chemical recognition [78]. THz spectroscopy has been applied also to the study of low-energy carrier dynamics in semiconductors, quantum dots, superconductors, and strongly correlated electron materials as well as conductivity studies in electronic materials [12]. Finally, liquids have been also extensively studied with THz spectroscopy [11]. In this case, THz absorption spectrum of a liquid is dominated by relaxation of either permanent dipoles in polar liquids (e.g., water or ethanol) or collision induced dipole moments in nonpolar liquids (e.g., benzene or toluene). Since most chemical reactions of importance in biology occur in an aqueous environment, a considerable percentage of the studies on the application of THz spectroscopy to liquids have been devoted to water and aqueous solutions of salts, sugars, and lower alcohols [11, 79].

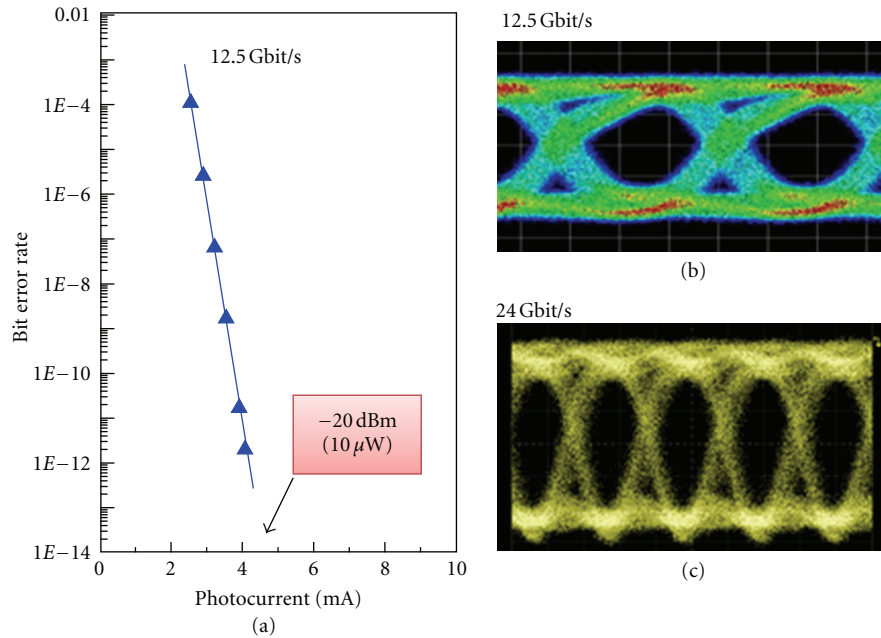


FIGURE 18: (a) Bit error rate characteristics of the wireless link at 12.5 Gbit/s. Eye diagrams at (b) 12.5 Gbit/s and (c) 24 Gbit/s.

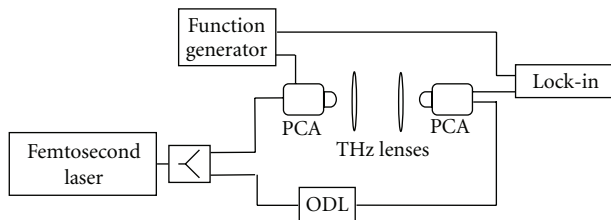


FIGURE 19: Block diagram of a generic fiber-based THz-TDS system.

- (ii) *Biological and pharmaceutical substances.* The capability of THz spectroscopy to observe intermolecular vibrations in some chemicals and organic molecules has led to its application to biomolecules, medicines, cancer tissue, DNA, proteins, and bacteria [8, 80, 81]. Another application is for polymorph classification in pharmacology [82]. There are substances that can be clearly identified from their THz-absorption spectra whereas FTIR measurements do not provide positive recognition. THz spectroscopy has also been applied for clinical diagnosis, in particular for discrimination between cancerous cells (basal cell carcinoma) and normal tissue [83]. However, the high cost of these systems has prevented practical clinical application of this approach.
- (iii) *Safety and security.* The capability for contactless chemical identification of THz waves jointly with the discovery of THz signatures of common explosives [84] led to the study of THz imaging and spectroscopy for detection of concealed explosives, drugs, and weapons. In particular, a wide

set of security applications have been analyzed ranging from THz cameras, detection of chemical and biological weapons, to archway body scanners for security checkpoints at airports, customs and even stand-off detection of explosives, improvised-explosive devices. Although several demonstrations of mail and luggage inspection have been successful [85, 86], the relatively weak and broad explosive signatures are regularly masked by the combined effects of atmospheric vapor absorption, barrier attenuation, and scattering from both clothing and the own explosive, making the practical deployment of remote through-barrier THz spectroscopic explosive detection systems very difficult to implement [87].

- (iv) *Industrial monitoring.* The THz spectrum can be used to monitor a wide range of industrial processes including polymeric compounding [88], quality control of plastic weld joints [89], moisture content in polymers [90], plastic fiber orientation [91], paper thickness and moisture content [92], and monitoring of industrial pollution [93], to cite some of them. Demonstrators have been presented, but technology improvements in terms of emitted power, scanning speed, and cost are needed to take advantage of the information in the THz domain while offering a competitive product.

Other applications include art conservation [94], detection of foreign bodies in food [95], pollutant and pesticide residue monitoring in food [96], and, last but not least, astronomy, the first field where far-infrared technology was developed [97, 98].

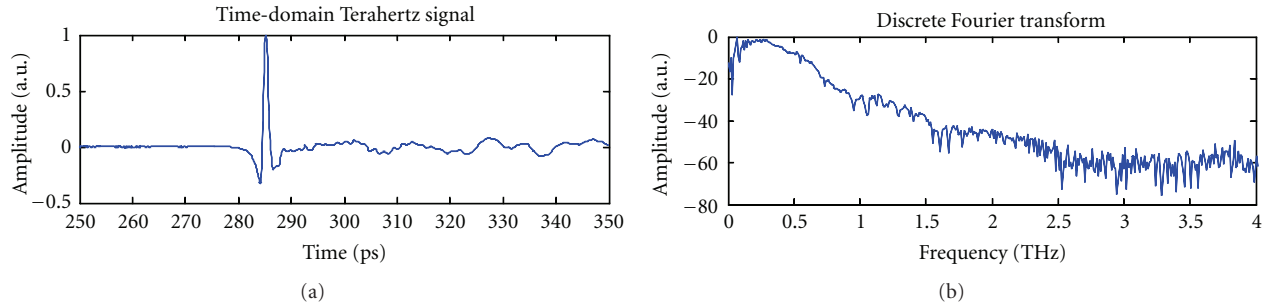


FIGURE 20: (a) Fiber-based THz-TDS temporal signal, (b) Fourier transform of (a).

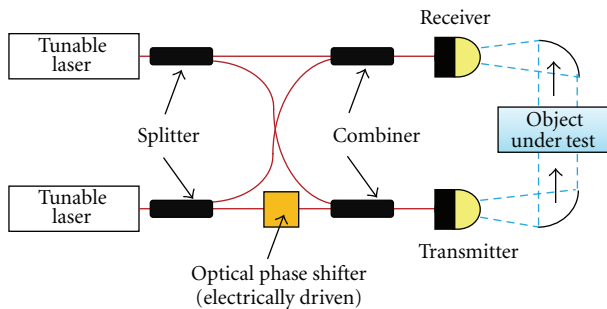


FIGURE 21: Schematic diagram of frequency domain spectroscopy (FDS) system using an optical phase shifter.

The main limitations to the wide deployment of THz spectroscopy in practical applications are related to current performance of THz technology, bulkiness of the instruments, and high cost. To overcome these restrictions, fiber optic technology can offer an interesting implementation in comparison to conventional bulk optics systems usually employed in THz spectroscopy.

4.1. Fiber-Optic THz Time Domain Spectroscopy. Sensing in the THz regime can be done using Fourier transform infrared (FTIR) spectroscopy. However, in the late 80s, an alternative method was proposed based on the excitation with femtosecond pulses of photoconductive dipole antennas to generate short pulses of THz radiation to probe materials [99]. This technique is known as THz Time-Domain Spectroscopy (THz-TDS). Unlike FTIR which is sensitive only to amplitude, THz-TDS can detect changes induced by the sample in both amplitude and phase, providing more information since real and imaginary parts of the optical constants are deduced simultaneously without using Kramers-Kronig analysis. Additionally, THz-TDS avoids the effect of background thermal radiation since THz waves are detected coherently unlike FTIR.

THz-TDS is based on producing terahertz energy using photoconductive switches or antennas (PCA) [7, 100]. A PCA is an electrical switch exploiting the increase in electrical conductivity of semiconductors and insulators when they are

exposed to light [101]. Several photoconductive materials have been tested for PCA: low-temperature grown gallium arsenide (LT-GaAs), radiation-damaged silicon-on-sapphire (RD-SOS), chromium-doped gallium arsenide (Cr-GaAs), indium phosphide (InP), and amorphous silicon. Among these LT-GaAs is probably the most common. The physical mechanism begins with an ultrafast laser pulse (with photon energy larger than the bandgap of the material), which creates electron-hole pairs in the photoconductor. The free carriers then accelerate in the static bias field to form a transient photocurrent, and the fast, time-varying current radiates electromagnetic waves [100]. To provide photons with enough energy, pulsed sources at 780–820 nm as Ti:Sapphire lasers are regularly used to match the bandgap of LT-GaAs. Typical optical-to-terahertz conversion efficiencies are below 10^{-5} . Even so, photoconductive emitters are capable of providing relatively large average THz power in comparison with other approaches with level powers up to $40 \mu\text{W}$ and bandwidths usually up to 4 THz [102] although recently has been demonstrated that by removing all absorbing elements in the THz beam path and using the shortest possible laser pulses (10 fs), photoconductive detection of frequencies approaching 100 THz has been reported [103].

Recently, other materials with smaller bandgaps than LT-GaAs have been proposed as photoconductive material. This allows the replacement of expensive and bulky Ti:Sapphire sources by cost-effective telecom 1550 nm sources. These materials include LT-InGaAs [104], LT-GaAsSb [105], ion-implanted InGaAs [106], and superlattice structures with LT-InGaAs/InAlAs [16, 107].

These new materials allow the implementation of fiber-optic THz-TDS systems [107]. These use a femtosecond fiber laser at telecom wavelengths (1550 nm) instead of a Ti:Sapphire (800 nm) which can reduce the cost of the photonic source between half and less than a third of the original budget. Figure 19 shows a setup for a fiber-based THz-TDS system. A fiber pulse source is used to generate 100 fs pulses which are split into two branches which fed two fiber-pigtailed PCAs. An optical delay line (ODL) is used to map THz traces, as shown in Figure 20. Fiber-based THz-TDS systems offer higher stability as well as reduced size and power consumption, and there are a wide range of mature, low-cost components developed for the optical communications market. Additionally, fiber-optic components

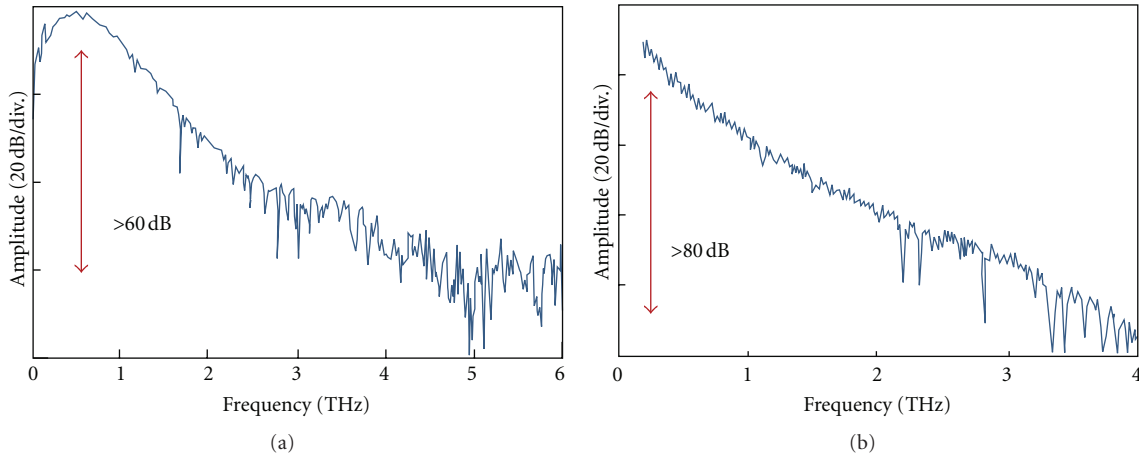


FIGURE 22: Comparison of typical spectral characteristics for (a) TDS and (b) FDS.

allow the implementation of compact, low-weight, and robust THz-TDS systems. Finally, telecom wavelengths and fiber-illuminated antennas allow the implementation of remote delivery for THz systems with small emitter and receiver heads and even sharing of a single optical source by several remote emitter/receiver heads to allow further cost saving [108].

4.2. Frequency Domain Spectroscopy. Recently, THz spectroscopy systems based on CW technology, which use monochromatic sources with an accurate frequency control capability, have attracted great interest [76, 109–113]. The CW source-based systems, referred to as frequency-domain spectroscopy (FDS), provide higher signal-to-noise ratio (SNR) and spectral resolution. When the frequency band of interest is targeted for the specific absorption line of the objects being tested, FDS systems with the selected frequency-scan length and resolution are more practical in terms of data acquisition time as well as system cost.

A THz-FDS system with photonic emitters and detectors is frequently called a homodyne system, and its configuration is the same as that of the THz-TDS system except for the optical signal source. The optical delay line is fixed after being adjusted to maximize the interference signal in case of the homodyne detection. In addition, the optical delay line can be replaced by the optical phase shifter such as electrooptic phase modulators and piezo-electric phase shifters as shown in Figure 21 [114, 115]. This method not only leads to the increase in the speed of delay change, but also enables an accurate phase measurement.

Like THz-TDS systems, THz-FDS systems are commercially available, which employ nonlinear crystals [116], photoconductive antennas (PCAs) [117–119], photodiodes [118] for THz generators, and electrooptic (EO) crystals [116], and photoconductive antennas (PCAs) [117–119] for THz detectors.

Figure 22 shows typical frequency spectra obtained with the fiber-optic TDS and FDS systems, respectively, which were reported by the Fraunhofer Heinrich Hertz Institute

[120]. The FDS system offers >80 dB dynamic range, which is higher than that of the fiber-optic TDS.

5. Conclusion

Different photonic technologies and applications based on the millimeter- and submillimeter-wave bands have been discussed in this overview paper. The key elements for the photonic generation and detection of high frequency signals (photodiodes and photoconductors) have been analyzed and a comparison has been provided. Recent advances in guided-wave techniques for THz systems have also been reviewed. The main conclusions are that for bench-top interconnection applications, the combination of dielectric loss and conductor loss forces the use of large conductors and conductor separations relative to those required for an on-chip application. It can be found that the two-wire waveguide offers the best combination of performance and practicality for bench-top terahertz interconnections in guided-wave systems. For on-chip applications, where a substrate is deemed essential and dimensions are typically less than a millimeter, we find that the slot line offers high performance, if suitable methods are employed to eliminate power loss into the substrate. Finally, adiabatic mode-converting tapers have been reviewed showing that these can be fabricated easily and with low loss. This work suggests that guided-wave terahertz systems may soon begin to displace the free-space systems in routine use today and enable new classes of terahertz applications and instruments with better performance and utility.

Two applications for the application of photonic technology to the millimeter and submillimeter-wave bands have been reviewed. First, it has been shown how different photonic technologies can be applied to generate and distribute signals in these bands to implement high-bit rate access network which will foster the deployment of new high bit-rate applications. Future challenges should address the increase of the receiver bandwidth towards 40-Gbit/s transmission and the integration of photonic components

into a one-chip transmitter consisting of lasers, modulators, photodiodes, and antennas. Additionally, the application of photonic technology to spectroscopic sensing has been also reviewed showing that both time- and frequency-domain spectroscopy systems can benefit from fiber-optic implementation easing the application of sensing in these spectral regions.

To summarize, the development of new components and architectures is paving the way to the deployment of applications in fields such as communications and sensing that offer new functionalities and capabilities. These technologies are playing a significant part in the increasing utilization of currently unproductive spectral regions.

Acknowledgments

B. Vidal would like to thank the Spanish Ministerio de Economía y Competitividad for its support through Project TEC2009-08078. T. Nagatsuma would like to acknowledge the financial support provided by the Ministry of Education, Science, Sports and Culture, Grant-in-Aid for Scientific Research (A) 23246067, 2011 and the JST-ANR WITH program.

References

- [1] G. P. Agrawal, *Fiber Optic Communication Systems*, John Wiley & Sons, New York, NY, USA, 2010.
- [2] A. J. Seeds, "Microwave photonics," *IEEE Transactions on Microwave Theory and Techniques*, vol. 50, no. 3, pp. 877–887, 2002.
- [3] J. Capmany and D. Novak, "Microwave photonics combines two worlds," *Nature Photonics*, vol. 1, no. 6, pp. 319–330, 2007.
- [4] R. C. Williamson and R. D. Esman, "RF photonics," *Journal of Lightwave Technology*, vol. 26, no. 9, pp. 1145–1153, 2008.
- [5] J. Yao, "Microwave photonics," *Journal of Lightwave Technology*, vol. 27, no. 3, pp. 314–335, 2009.
- [6] T. Berceci and P. R. Herzfeld, "Microwave photonics—a historical perspective," *IEEE Transactions on Microwave Theory and Techniques*, vol. 58, no. 11, pp. 2992–3000, 2010.
- [7] P. H. Siegel, "Terahertz technology," *IEEE Transactions on Microwave Theory and Techniques*, vol. 50, no. 3, pp. 910–928, 2002.
- [8] M. Tonouchi, "Cutting-edge terahertz technology," *Nature Photonics*, vol. 1, no. 2, pp. 97–105, 2007.
- [9] B. Ferguson and X. C. Zhang, "Materials for terahertz science and technology," *Nature Materials*, vol. 1, no. 1, pp. 26–33, 2002.
- [10] T. Nagatsuma, "Generating millimeter and terahertz waves," *IEEE Microwave Magazine*, vol. 10, no. 4, pp. 64–74, 2009.
- [11] P. U. Jepsen, D. G. Cooke, and M. Koch, "Terahertz spectroscopy and imaging—modern techniques and applications," *Laser and Photonics Reviews*, vol. 5, no. 1, pp. 124–166, 2011.
- [12] S. L. Dexheimer, *Terahertz Spectroscopy*, CRC Press, New York, NY, USA, 2008.
- [13] K. L. Yeh, M. C. Hoffmann, J. Hebling, and K. A. Nelson, "Generation of 10 μ J ultrashort terahertz pulses by optical rectification," *Applied Physics Letters*, vol. 90, no. 17, Article ID 171121, 3 pages, 2007.
- [14] A. G. Stepanov, S. Henin, Y. Petit, L. Bonacina, J. Kasparian, and J. P. Wolf, "Mobile source of high-energy single-cycle terahertz pulses," *Applied Physics B*, vol. 101, no. 1-2, pp. 11–14, 2010.
- [15] E. R. Brown, "Advancements in photomixing and photoconductive switching for THz spectroscopy and imaging," in *4th Terahertz Technology and Applications*, vol. 7938 of *Proceedings of SPIE*, San Francisco, Calif, USA, January 2011.
- [16] H. Roehle, R. J. B. Dietz, H. J. Hensel et al., "Next generation 1.5 μ m terahertz antennas: mesa-structuring of InGaAs/InAlAs photoconductive layers," *Optics Express*, vol. 18, no. 3, pp. 2296–2301, 2010.
- [17] K. Kato, "Ultrawide-B and/high-frequency photodetectors," *IEEE Transactions on Microwave Theory and Techniques*, vol. 47, no. 7, pp. 1265–1281, 1999.
- [18] N. Shimizu and T. Nagatsuma, "Photodiode-integrated microstrip antenna array for subterahertz radiation," *IEEE Photonics Technology Letters*, vol. 18, no. 6, pp. 743–745, 2006.
- [19] H. J. Song, K. Ajito, Y. Muramoto, A. Wakatsuki, T. Nagatsuma, and N. Kukutsu, "Uni-travelling-carrier photodiode module generating 300 GHz power greater than 1 mW," *IEEE Microwave and Wireless Components Letters*, vol. 22, no. 7, pp. 363–365, 2012.
- [20] T. Nagatsuma, A. Kaino, S. Hisatake et al., "Continuous-wave terahertz spectroscopy system based on photodiodes," *PIERS Online*, vol. 6, no. 4, pp. 390–394, 2010.
- [21] E. Rouvalis, M. J. Fice, C. C. Renaud, and A. J. Seeds, "Millimeter-wave optoelectronic mixers based on uni-traveling carrier photodiodes," *IEEE Transactions on Microwave Theory and Techniques*, vol. 60, no. 3, pp. 686–691, 2012.
- [22] M. Y. Frankel, S. Gupta, J. A. Valdmanis, and G. A. Mourou, "Terahertz attenuation and dispersion characteristics of coplanar transmission lines," *IEEE Transactions on Microwave Theory and Techniques*, vol. 39, no. 6, pp. 910–916, 1991.
- [23] G. Gallot, S. P. Jamison, R. W. McGowan, and D. Grischkowsky, "Terahertz waveguides," *Journal of the Optical Society of America B*, vol. 17, no. 5, pp. 851–863, 2000.
- [24] R. Mendis and D. Grischkowsky, "Plastic ribbon THz waveguides," *Journal of Applied Physics*, vol. 88, no. 7, pp. 4449–4451, 2000.
- [25] L. J. Chen, H. W. Chen, T. F. Kao, J. Y. Lu, and C. K. Sun, "Low-loss subwavelength plastic fiber for terahertz waveguiding," *Optics Letters*, vol. 31, no. 3, pp. 308–310, 2006.
- [26] S. P. Jamison, R. W. McGowan, and D. Grischkowsky, "Single-mode waveguide propagation and reshaping of subps terahertz pulses in sapphire fibers," *Applied Physics Letters*, vol. 76, no. 15, pp. 1987–1989, 2000.
- [27] K. Wang and D. M. Mittleman, "Metal wires for terahertz wave guiding," *Nature*, vol. 432, no. 7015, pp. 376–379, 2004.
- [28] T. I. Jeon, J. Zhang, and D. Grischkowsky, "THz Sommerfeld wave propagation on a single metal wire," *Applied Physics Letters*, vol. 86, no. 16, Article ID 161904, 3 pages, 2005.
- [29] J. A. Deibel, K. Wang, M. D. Escarra, and D. M. Mittleman, "Enhanced coupling of terahertz radiation to cylindrical wire waveguides," *Optics Express*, vol. 14, no. 1, pp. 279–290, 2006.
- [30] R. Mendis and D. M. Mittleman, "Multifaceted terahertz applications of parallel-plate waveguide: TE₁ mode," *Electronics Letters*, vol. 46, pp. 40–44, 2010.
- [31] M. K. Mbonye, V. Astley, W. L. Chan, J. A. Deibel, and D. M. Mittleman, "A terahertz dual wire waveguide," in *Proceedings of the Lasers and Electro-Optics Conference, Optical Society of America*, p. CThLL1, Baltimore, Maryland, USA, 2007.

- [32] H. Pahlevaninezhad, T. E. Darcie, and B. Heshmat, "Two-wire waveguide for terahertz," *Optics Express*, vol. 18, no. 7, pp. 7415–7420, 2010.
- [33] H. Pahlevaninezhad and T. E. Darcie, "Coupling of terahertz waves to a two-wire waveguide," *Optics Express*, vol. 18, no. 22, pp. 22614–22624, 2010.
- [34] M. Mbonye, R. Mendis, and D. M. Mittleman, "A terahertz two-wire waveguide with low bending loss," *Applied Physics Letters*, vol. 95, no. 23, Article ID 233506, 3 pages, 2009.
- [35] C. Roman, O. Ichim, L. Sarger, V. Vigneras, and P. Mounaix, "Terahertz dielectric characterisation of polymethacrylimide rigid foam: the perfect sheer plate?" *Electronics Letters*, vol. 40, no. 19, pp. 1167–1169, 2004.
- [36] C. Fattinger and D. Grischkowsky, "Observation of electromagnetic shock waves from propagating surface-dipole distributions," *Physical Review Letters*, vol. 62, no. 25, pp. 2961–2964, 1989.
- [37] P. H. Siegel, R. P. Smith, M. C. Gaidis, and S. C. Martin, "2.5-THz GaAs monolithic membrane-diode mixer," *IEEE Transactions on Microwave Theory and Techniques*, vol. 47, no. 5, pp. 596–604, 1999.
- [38] H. Pahlevaninezhad, B. Heshmat, and T. E. Darcie, "Efficient terahertz slot-line waveguides," *Optics Express*, vol. 19, no. 26, pp. B47–B55, 2011.
- [39] D. Grischkowsky, S. Keiding, M. van Exter, and C. Fattinger, "Far-infrared time-domain spectroscopy with terahertz beams of dielectrics and semiconductors," *Journal of Optical Society of America B*, vol. 7, no. 10, pp. 2006–2015, 1990.
- [40] H. Pahlevaninezhad, *Design and implementation of efficient terahertz waveguides [Ph.D. thesis]*, 2012.
- [41] C. Loyez, C. Lethien, R. Kassi et al., "Subcarrier radio signal transmission over multimode fibre for 60 GHz WLAN using a phase noise cancellation technique," *Electronics Letters*, vol. 41, no. 2, pp. 91–92, 2005.
- [42] A. Nkansah, A. Das, N. J. Gomes, and P. Shen, "Multilevel modulated signal transmission over serial single-mode and multimode fiber links using vertical-cavity surface-emitting lasers for millimeter-wave wireless communications," *IEEE Transactions on Microwave Theory and Techniques*, vol. 55, no. 6, pp. 1219–1227, 2007.
- [43] M. G. Larrodé and A. M. J. Koonen, "Theoretical and experimental demonstration of OFM robustness against modal dispersion impairments in radio over multimode fiber links," *Journal of Lightwave Technology*, vol. 26, no. 12, pp. 1722–1728, 2008.
- [44] U. Gliese, S. Norskov, and T. N. Nielsen, "Chromatic dispersion in fiber-optic microwave and millimeter-wave links," *IEEE Transactions on Microwave Theory and Techniques*, vol. 44, no. 10, pp. 1716–1724, 1996.
- [45] G. P. Agrawal, *Nonlinear Fiber Optics*, Academic Press, New York, NY, USA.
- [46] J. J. O'Reilly, P. M. Lane, R. Heidemann, and R. Hofstetter, "Optical generation of very narrow linewidth millimetre wave signals," *Electronics Letters*, vol. 28, no. 25, pp. 2309–2311, 1992.
- [47] G. Qi, J. Yao, J. Seregelyi, C. Bélisle, and S. Paquet, "Generation and distribution of a wide-band continuously tunable millimeter-wave signal with an optical external modulation technique," *IEEE Transactions on Microwave Theory and Techniques*, vol. 53, no. 10, pp. 3090–3097, 2005.
- [48] P. Shen, N. J. Gomes, P. A. Davies, W. P. Shillue, P. G. Huggard, and B. N. Ellison, "High-purity millimeter-wave photonic local oscillator generation and delivery," in *Proceedings of the International Microwave Photonics Topical Meeting (WP'03)*, pp. 189–192, Budapest, Hungary.
- [49] G. Qi, J. Yao, J. Seregelyi, C. Bélisle, and S. Paquet, "Optical generation and distribution of continuously tunable millimeter-wave signals using an optical phase modulator," *Journal of Lightwave Technology*, vol. 23, no. 9, pp. 2687–2695, 2005.
- [50] B. Vidal, P. G. Huggard, B. N. Ellison, and N. J. Gomes, "Optoelectronic generation of W-band millimetre-wave signals using Brillouin amplification," *Electronics Letters*, vol. 46, no. 21, pp. 1449–1450, 2010.
- [51] L. Goldberg, H. F. Taylor, J. F. Weller, and D. M. Bloom, "Microwave signal generation with injection locked laser diodes," *Electronics Letters*, vol. 19, no. 13, pp. 491–493, 1983.
- [52] R. T. Ramos and A. J. Seeds, "Delay, linewidth and bandwidth limitations in optical phase-locked loop design," *Electronics Letters*, vol. 26, no. 6, pp. 389–391, 1990.
- [53] A. C. Bordonalli, C. Walton, and A. J. Seeds, "High-performance phase locking of wide line width semiconductor lasers by combined use of optical injection locking and optical phase-lock loop," *Journal of Lightwave Technology*, vol. 17, no. 2, pp. 328–342, 1999.
- [54] D. Wake, C. R. Liana, and P. A. Davies, "Optical generation of millimeter-wave signals for fiber-radio systems using a dual-mode DFB semiconductor laser," *IEEE Transactions on Microwave Theory and Techniques*, vol. 43, no. 9, pp. 2270–2276, 1995.
- [55] F. van Dijk, A. Accard. Enard, O. Drisse, D. Make, and F. Lelarge, "Monolithic dual wavelength DFB lasers for narrow linewidth heterodyne beat-note generation," in *Proceedings of the International Topical Meeting on Microwave Photonics (MWP'11)*, pp. 73–76, Singapore, October 2011.
- [56] P. G. Huggard, B. N. Ellison, P. Shen et al., "Generation of millimetre and sub-millimetre waves by photomixing in 1.55 μm wavelength photodiode," *Electronics Letters*, vol. 38, no. 7, pp. 327–328, 2002.
- [57] C. H. Cox III, G. E. Betts, and L. M. Johnson, "Analytic and experimental comparison of direct and external modulation in analog fiber-optic links," *IEEE Transactions on Microwave Theory and Techniques*, vol. 38, no. 5, pp. 501–509, 1990.
- [58] M. L. Farwell, W. S. C. Chang, and D. R. Huber, "Increased linear dynamic range by low biasing the Mach-Zehnder modulator," *IEEE Photonics Technology Letters*, vol. 5, no. 7, pp. 779–782, 1993.
- [59] J. Armstrong, "OFDM for optical communications," *Journal of Lightwave Technology*, vol. 27, pp. 189–204, 2009.
- [60] H. Arslan and H. A. Mahmoud, "Error vector magnitude to SNR conversion for nondata-aided receivers," *IEEE Transactions on Wireless Communications*, vol. 8, no. 5, pp. 2694–2704, 2009.
- [61] A. Nkansah, A. Das, N. J. Gomes, P. Shen, and D. Wake, "VCSEL-based single-mode and multimode fiber star/tree distribution network for millimeter-wave wireless systems," in *Proceedings of the International Topical Meeting on Microwave Photonics (MWP'06)*, pp. 1–4, Grenoble, France, October 2006.
- [62] C. Lim, A. Nirmalathas, D. Novak, and R. B. Waterhouse, "Capacity analysis and optimum channel allocations for a WDM ring fibre-radio backbone incorporating wavelength interleaving with a sectorized antenna interface," in *Proceedings of the International Topical Meeting on Microwave Photonics (MWP'02)*, pp. 371–374, November 2002.
- [63] X. Zhang, B. Liu, J. Yao, and R. Kashyap, "A novel millimeter-wave-band radio-over-fiber system with dense

- wavelength-division multiplexing bus architecture,” *IEEE Transactions on Microwave Theory and Techniques*, vol. 54, no. 2, pp. 929–936, 2006.
- [64] W. P. Lin, “A robust fiber-radio architecture for wavelength-division-multiplexing ring-access networks,” *Journal of Lightwave Technology*, vol. 23, no. 9, pp. 2610–2620, 2005.
- [65] Z. Jia, J. Yu, G. Ellinas, and G. K. Chang, “Key enabling technologies for optical wireless networks: optical millimeter-wave generation, wavelength reuse, and architecture,” *Journal of Lightwave Technology*, vol. 25, no. 11, pp. 3452–3471, 2007.
- [66] R. Sambaraju, J. Herrera, J. Marti et al., “Up to 40 Gb/s wireless signal generation and demodulation in 75–110 GHz band using photonic techniques,” in *Proceedings of the IEEE International Topical Meeting on Microwave Photonics (MWP’10)*, pp. 1–4, Montreal, Canada, October 2010.
- [67] M. Weiss, A. Stohr, F. Lecoche, and B. Charbonnier, “27 Gbit/s photonic wireless 60 GHz transmission system using 16-QAM OFDM,” in *Proceedings of the International Topical Meeting on Microwave Photonics (MWP’09)*, Valencia, Spain, October 2009.
- [68] J. James, P. Shen, A. Nkansah, X. Liang, and N. J. Gomes, “Nonlinearity and noise effects in multi-level signal millimeter-wave over fiber transmission using single and dual wavelength modulation,” *IEEE Transactions on Microwave Theory and Techniques*, vol. 58, no. 11, pp. 3189–3198, 2010.
- [69] J. Federici and L. Moeller, “Review of terahertz and subterahertz wireless communications,” *Journal of Applied Physics*, vol. 107, no. 11, Article ID 111101, 22 pages, 2010.
- [70] T. Kleine-Ostmann and T. Nagatsuma, “A review on terahertz communications research,” *Journal of Infrared, Millimeter, and Terahertz Waves*, vol. 32, no. 2, pp. 143–171, 2011.
- [71] H. J. Song and T. Nagatsuma, “Present and future of terahertz communications,” *IEEE Trans. Terahertz Science and Technology*, vol. 1, no. 1, pp. 256–264, 2011.
- [72] T. Nagatsuma, H. J. Song, Y. Fujimoto et al., “Giga-bit wireless link using 300–400 GHz bands,” in *Proceedings of the IEEE International Topical Meeting on Microwave Photonics (MWP’09)*, Valencia, Spain, October 2009.
- [73] H. J. Song, K. Ajito, A. Wakatsuki et al., “Terahertz wireless communication link at 300 GHz,” in *Proceedings of the IEEE International Topical Meeting on Microwave Photonics (MWP’10)*, pp. 42–45, Montreal, Canada, October 2010.
- [74] A. Wakatsuki, T. Furuta, Y. Muramoto, T. Yoshimatsu, and H. Ito, “High-power and broadband sub-terahertz wave generation using a J-band photomixer module with rectangular-waveguide output port,” in *Proceedings of the 33rd International Conference on Infrared and Millimeter Waves and the 16th International Conference on Terahertz Electronics, 2008, IRMMW-THz 2008*, pp. 1–2, Pasadena, Calif, USA, September 2008.
- [75] A. J. Seeds, M. J. Fice, F. Pozzi et al., “Photonic-enabled microwave and terahertz communication systems,” in *Proceedings of the Optical Fiber Communication (OFC’09)*, pp. 1–3, March 2009, OTuE6.
- [76] M. J. Fice, E. Rouvalis, L. Ponnampalam, C. C. Renaud, and A. J. Seeds, “Telecommunications technology-based terahertz sources,” *Electronics Letters*, vol. 46, no. 26, pp. s28–s31, 2010.
- [77] K. D. M. Möller and W. G. Rothschild, *Far-Infrared Spectroscopy*, John Wiley & Sons, New York, NY, USA, 1971.
- [78] B. Fischer, M. Hoffmann, H. Helm, G. Modjesch, and P. U. Jepsen, “Chemical recognition in terahertz time-domain spectroscopy and imaging,” *Semiconductor Science and Technology*, vol. 20, no. 7, pp. S246–S253, 2005.
- [79] J. T. Kindt and C. A. Schmuttenmaer, “Far-infrared dielectric properties of polar liquids probed by femtosecond terahertz pulse spectroscopy,” *Journal of Physical Chemistry*, vol. 100, no. 24, pp. 10373–10379, 1996.
- [80] B. M. Fischer, M. Walther, and P. U. Jepsen, “Far-infrared vibrational modes of DNA components studied by terahertz time-domain spectroscopy,” *Physics in Medicine and Biology*, vol. 47, no. 21, pp. 3807–3814, 2002.
- [81] K. Ajito and Y. Ueno, “THz chemical imaging for biological applications,” *IEEE Transactions on Terahertz Science and Technology*, vol. 1, no. 1, pp. 293–300, 2011.
- [82] P. F. Taday, I. V. Bradley, D. D. Arnone, and M. Pepper, “Using Terahertz pulse spectroscopy to study the crystalline structure of a drug: a case study of the polymorphs of ranitidine hydrochloride,” *Journal of Pharmaceutical Sciences*, vol. 92, no. 4, pp. 831–838, 2003.
- [83] R. M. Woodward, B. E. Cole, V. P. Wallace et al., “Terahertz pulse imaging in reflection geometry of human skin cancer and skin tissue,” *Physics in Medicine and Biology*, vol. 47, no. 21, pp. 3853–3863, 2002.
- [84] A. G. Davies, A. D. Burnett, W. Fan, E. H. Linfield, and J. E. Cunningham, “Terahertz spectroscopy of explosives and drugs,” *Materials Today*, vol. 11, no. 3, pp. 18–26, 2008.
- [85] D. Zimdars, J. S. White, G. Stuk, A. Chernovsky, G. Fichter, and S. Williamson, “Large area terahertz imaging and non-destructive evaluation applications,” *Insight*, vol. 48, no. 9, pp. 537–539, 2006.
- [86] H. Hoshina, Y. Sasaki, A. Hayashi, C. Otani, and K. Kawase, “Noninvasive mail inspection system with terahertz radiation,” *Applied Spectroscopy*, vol. 63, no. 1, pp. 81–86, 2009.
- [87] M. C. Kemp, “Explosives detection by terahertz spectroscopy—a bridge too far,” *IEEE Transactions on Terahertz Science and Technology*, vol. 1, no. 1, pp. 282–292, 2011.
- [88] S. Wietzke, C. Jansen, F. Rutz, D. M. Mittleman, and M. Koch, “Determination of additive content in polymeric compounds with terahertz time-domain spectroscopy,” *Polymer Testing*, vol. 26, no. 5, pp. 614–618, 2007.
- [89] C. Jansen, S. Wietzke, O. Peters et al., “Terahertz imaging: applications and perspectives,” *Applied Optics*, vol. 49, no. 19, pp. E48–E57, 2010.
- [90] C. Jördens, S. Wietzke, M. Scheller, and M. Koch, “Investigation of the water absorption in polyamide and wood plastic composite by terahertz time-domain spectroscopy,” *Polymer Testing*, vol. 29, no. 2, pp. 209–215, 2010.
- [91] F. Rutz, M. Koch, S. Khare, M. Moneke, H. Richter, and U. Ewert, “Terahertz quality control of polymeric products,” *International Journal of Infrared and Millimeter Waves*, vol. 27, no. 4, pp. 547–556, 2006.
- [92] J. B. Jackson, J. Bowen, G. Walker et al., “A survey of terahertz applications in cultural heritage conservation science,” *IEEE Transactions on Terahertz Science and Technology*, vol. 1, no. 1, pp. 220–231, 2011.
- [93] D. Banerjee, W. von Spiegel, M. D. Thomson, S. Schabel, and H. G. Roskos, “Diagnosing water content in paper by terahertz radiation,” *Optics Express*, vol. 16, no. 12, pp. 9060–9066, 2008.
- [94] F. Hindle, A. Cuisset, R. Bocquet, and G. Mouret, “Continuous-wave terahertz by photomixing: applications to gas phase pollutant detection and quantification,” *Comptes Rendus Physique*, vol. 9, no. 2, pp. 262–275, 2008.
- [95] C. Jördens and M. Koch, “Detection of foreign bodies in chocolate with pulsed terahertz spectroscopy,” *Optical Engineering*, vol. 47, no. 3, Article ID 037003, 2008.

- [96] Y. Hua and H. Zhang, "Qualitative and quantitative detection of pesticides with terahertz time-domain spectroscopy," *IEEE Transactions on Microwave Theory and Techniques*, vol. 58, no. 7, pp. 2064–2070, 2010.
- [97] R. Blundell and C. Y. E. Tong, "Submillimeter receivers for radio astronomy," *Proceedings of the IEEE*, vol. 80, no. 11, pp. 1702–1720, 1992.
- [98] C. Kulesa, "Terahertz spectroscopy for astronomy: from comets to cosmology," *IEEE Transactions on Terahertz Science and Technology*, vol. 1, no. 1, pp. 232–240, 2011.
- [99] M. van Exter, C. Fattinger, and D. Grischkowsky, "Terahertz time-domain spectroscopy of water vapor," *Optics Letters*, vol. 14, no. 20, pp. 1128–1130, 1989.
- [100] Y. S. Lee, *Principles of Terahertz Science and Technology*, Springer, New York, NY, USA, 2009.
- [101] D. H. Auston, "Picosecond optoelectronic switching and gating in silicon," *Applied Physics Letters*, vol. 26, no. 3, pp. 101–103, 1975.
- [102] N. Katzenellenbogen and D. Grischkowsky, "Efficient generation of 380 fs pulses of THz radiation by ultrafast laser pulse excitation of a biased metal-semiconductor interface," *Applied Physics Letters*, vol. 58, no. 3, pp. 222–224, 1991.
- [103] M. Ashida, "Ultra-broadband terahertz wave detection using photoconductive antenna," *Japanese Journal of Applied Physics*, vol. 47, no. 10, pp. 8221–8225, 2008.
- [104] C. Baker, I. S. Gregory, W. R. Tribe et al., "Highly resistive annealed low-temperature-grown InGaAs with sub-500 fs carrier lifetimes," *Applied Physics Letters*, vol. 85, no. 21, pp. 4965–4967, 2004.
- [105] J. Sigmund, C. Sydlo, H. L. Hartnagel et al., "Structure investigation of low-temperature-grown GaAsSb, a material for photoconductive terahertz antennas," *Applied Physics Letters*, vol. 87, no. 25, Article ID 252103, 3 pages, 2005.
- [106] M. Suzuki and M. Tonouchi, "Fe-implanted InGaAs photoconductive terahertz detectors triggered by 1.56 μm femtosecond optical pulses," *Applied Physics Letters*, vol. 86, no. 16, Article ID 163504, 3 pages, 2005.
- [107] B. Sartorius, H. Roehle, H. Künzel et al., "All-fiber terahertz time-domain spectrometer operating at 1.5 μm telecom wavelengths," *Optics Express*, vol. 16, no. 13, pp. 9565–9570, 2008.
- [108] Palací and B. Vidal, "Distributed THz transmitter/receiver based on a 1.5 μm Fiber Link," in *Proceedings of the 36th International Conference on Infrared, Millimeter and Terahertz Waves (IRMMW-THz)*, Houston, Tex, USA, October 2011.
- [109] J. R. Demers, R. T. Logan Jr., and E. R. Brown, "An optically integrated coherent frequency-domain THz spectrometer with signal-to-noise ratio up to 80 dB," in *Proceedings of the International Topical Meeting on Microwave Photonics (MWP'07)*, pp. 92–95, Victoria, Canada, October 2007.
- [110] M. Scheller, K. Baaske, and M. Koch, "Multifrequency continuous wave terahertz spectroscopy for absolute thickness determination," *Applied Physics Letters*, vol. 96, no. 15, Article ID 151112, 3 pages, 2010.
- [111] H. J. Song, N. Shimizu, T. Furuta, K. Suizu, H. Ito, and T. Nagatsuma, "Broadband-frequency-tunable sub-terahertz wave generation using an optical comb, AWGs, optical switches, and a uni-traveling carrier photodiode for spectroscopic applications," *Journal of Lightwave Technology*, vol. 26, no. 15, pp. 2521–2530, 2008.
- [112] A. Roggenbuck, H. Schmitz, A. Deninger et al., "Coherent broadband continuous-wave terahertz spectroscopy on solid-state samples," *New Journal of Physics*, vol. 12, Article ID 043017, 2010.
- [113] D. Stanze, A. Deninger, A. Roggenbuck, S. Schindler, M. Schlak, and B. Sartorius, "Compact cw terahertz spectrometer pumped at 1.5 μm wavelength," *Journal of Infrared, Millimeter, and Terahertz Waves*, vol. 32, no. 2, pp. 225–232, 2011.
- [114] T. Göbel, D. Schoenherr, C. Sydlo, M. Feiginov, P. Meissner, and H. L. Hartnagel, "Single-sampling-point coherent detection in continuous-wave photomixing terahertz systems," *Electronics Letters*, vol. 45, no. 1, pp. 65–66, 2009.
- [115] S. Hisatake, G. Kitahara, N. Kukutsu, Y. Fukada, N. Yoshimoto, and T. Nagatsuma, "Phase-sensitive terahertz self-heterodyne system based on photonic techniques," in *Proceedings of the IEEE International Topical Meeting on Microwave Photonics (MWP)*, 2012.
- [116] http://www.rainbowphotonics.com/prod_teratune.php.
- [117] <http://www.teraview.com/products/terahertz-continuous-wave-cw400/index.html>.
- [118] http://www.toptica.com/products/terahertz_generation/lasers_and_photomixers_for_cw_terahertz_generation.html.
- [119] <http://emcorephotonicsystems.com/products/terahertz-thz-frequency-domain-spectrometer-ftir/>.
- [120] <http://www.hhi.fraunhofer.de/en/departments/photonic-components/terahertz-generation-detection/>.

Research Article

X-Cut LiNbO₃ Optical Modulators Using Gap-Embedded Patch-Antennas for Wireless-Over-Fiber Systems

Yusuf Nur Wijayanto,¹ Hiroshi Murata,¹ Tetsuya Kawanishi,² and Yasuyuki Okamura¹

¹Division of Advanced Electronics and Optical Science, Department of Systems Innovation, Graduate School of Engineering Science, Osaka University, 1-3 Machikaneyama, Toyonaka, Osaka 560-8531, Japan

²Lightwave Device Laboratory, Photonic Network Research Institute, National Institute of Information and Communications Technology, 4-2-1 Nukui-Kitamachi, Koganei, Tokyo 184-8795, Japan

Correspondence should be addressed to Yusuf Nur Wijayanto, wijayanto@ec.ee.es.osaka-u.ac.jp

Received 15 July 2012; Accepted 17 September 2012

Academic Editor: Borja Vidal

Copyright © 2012 Yusuf Nur Wijayanto et al. This is an open access article distributed under the Creative Commons Attribution License, which permits unrestricted use, distribution, and reproduction in any medium, provided the original work is properly cited.

We propose an *x*-cut LiNbO₃ optical modulator using gap-embedded patch-antennas for wireless-over-fiber systems. The proposed device is composed of an array of narrow-gap-embedded patch-antennas and an optical waveguide located at the center of the gap without a buffer layer. The modulation efficiency of the proposed *x*-cut LiNbO₃ optical modulators was enhanced by 6 dB compared to the *z*-cut LiTaO₃-based devices.

1. Introduction

Wireless-over-fiber technology suitably supports wireless communication systems in microwave/millimeter-wave bands by compensating for large transmission losses of metallic cables [1]. In wireless-over-fiber technology for communication systems, microwave/millimeter-wave signals are converted to lightwave signals and transferred through optical fibers with low transmission loss. Large transmission bandwidth and no induction are also advantages of the optical fibers [2]. The wireless-over-fiber systems are composed of two domains: one is a microwave/millimeter-wave domain and the other is an optical domain. Therefore, conversion devices between the microwave/millimeter-wave and optical signals are required to realize the wireless-over-fiber systems.

A microwave/millimeter-wave generation for downlink in wireless-over-fiber systems can be achieved by a high-speed photodiode [3]. On the contrary for uplink conversion, the microwave/millimeter-wave signals can be directly converted into lightwave signals by use of high-speed optical modulation technology [4].

A conversion device from wireless microwave to lightwave signals can be composed of wireless microwave antennas and electrooptic (EO) modulators [5]. Wireless microwave signals can be received by the antennas. The received signals are transferred to the EO modulators by a connection line such as coaxial cables. However, microwave signal distortion and decay might occur in the coaxial cables due to high-frequency operation.

In order to reduce the microwave signal distortion and realize a simple compact device, wireless microwave-lightwave signal converters using integration of wireless microwave antennas and optical modulators have been developed. Several EO modulators using antenna-coupled resonant modulation electrodes were reported [6–10]. They were composed of planar antennas for wireless microwave signal receiving, resonant electrodes for optical modulation, and their connection lines on an EO crystal as a substrate. The antennas, resonant electrodes, and connection lines should be tuned precisely to obtain good resonance and impedance matching conditions for effective conversion. However, the complete matching and precise tuning are difficult and the microwave distortion might be still induced through the coupling of them.

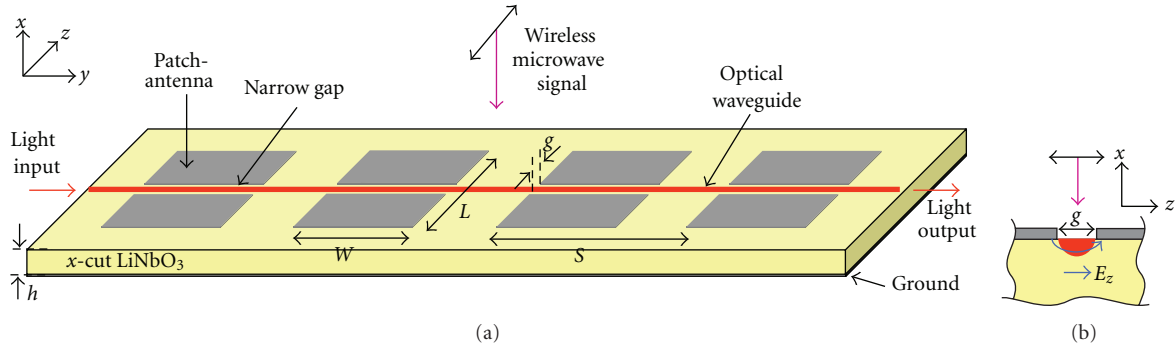


FIGURE 1: Schematic device structures of x -cut LiNbO₃ optical modulators using gap-embedded patch-antennas. (a) Whole device structure (3D view). (b) Cross-sectional view configuration of the device structure in xz -plane.

We have demonstrated EO modulators using patch-antennas embedded with narrow gaps on a z -cut LiTaO₃ crystal as the substrate [11–13]. The EO modulators are composed of patch-antennas only and there is no other planar structure on the substrate. They have no required precise tuning. Therefore, the optical modulation with extremely low distortion can be obtained with simple compact structures. Their basic operations were verified successfully with no external electrical power supply. However, modulation efficiency remains low due to large dielectric constant of the LiTaO₃ substrate and buffer layer structures in the devices.

In this paper, we propose a new x -cut LiNbO₃ optical modulator using gap-embedded patch-antennas for wireless microwave-lightwave signal conversion in the wireless-over-fiber systems. The proposed device is fabricated on z -cut LiNbO₃ with lower dielectric constant and no buffer layer structures. The basic operations of the proposed device were demonstrated experimentally at wireless microwave frequency of 26 GHz. Their modulation efficiency was enhanced by ~ 6 dB compared with the LiTaO₃-based devices [12].

In the following sections, the device structure, operational principle, analysis, and experiments are presented.

2. Device Structures

Figure 1 shows the structure of the proposed x -cut LiNbO₃ optical modulator using gap-embedded patch-antennas. It consists of a channel optical waveguide and patch-antennas embedded with a narrow-gap onto an x -cut LiNbO₃ as the substrate. An array of the gap-embedded patch-antennas is set onto the substrate with a separation, S , which is key parameter to determine the characteristics in microwave-lightwave interactions described in the next section. The length, L , of each antenna along the x -axis is set as half a wavelength of the wireless microwave signal. The width, W , of each antenna along the y -axis is set as below one wavelength of the wireless microwave signal to avoid unwanted higher-order mode effects. The narrow gap in micrometer order is set at the centre of each antenna, along the y -axis. The optical waveguide is located at the center of the gap, where the magnified cross-sectional view is shown in

Figure 1(b). The reverse side of the substrate is covered with a ground electrode.

When a wireless signal is irradiated to a standard patch-antenna with no gap, a standing wave current is induced on the patch-antenna surface and becomes maximum at the center [14, 15]. With introducing a narrow gap at the center of the patch-antenna perpendicular to the surface current, a displacement current must be induced across the gap due to continuity of the current flow [16]. The strong electric field is also induced across the gap. When a lightwave propagates into an optical waveguide located under the gap, a lightwave is modulated by the wireless microwave signal through Pockels effects and the converted signal is obtained [17].

The optical modulation can be enhanced using the proposed device fabricated on the x -cut LiNbO₃ substrate. A buffer layer is not required. The dielectric constant of the x -cut LiNbO₃ along z -axis is about 28 and the LiTaO₃ is about 42. Therefore, strong electric field across the gap can be obtained using the proposed x -cut LiNbO₃ optical modulator. The efficiency enhancement is obtained by the lower dielectric constant of the substrate and no buffer layer.

3. Operational Principle

When a wireless microwave signal at the angular frequency ω_m is irradiated to the proposed device, the displacement current and strong electric field are induced across the narrow gap. The induced electric field is obtained by the time integration of the displacement currents [16]. The induced electric field can be expressed as

$$E_m^0(t) = E_{m0} \sin(\omega_m t). \quad (1)$$

When a lightwave propagates in the optical waveguide, the microwave electric field as would be observed by the lightwave can be expressed by the following equation taking into account the transit time of the lightwave [18, 19]:

$$\begin{aligned} E_{m\text{-opt}}^0(y) &= E_m^0 \left(\frac{y - y'}{v_g} \right) \\ &= E_{m0} \sin \left[k_m n_g y + \varphi \right], \end{aligned} \quad (2)$$

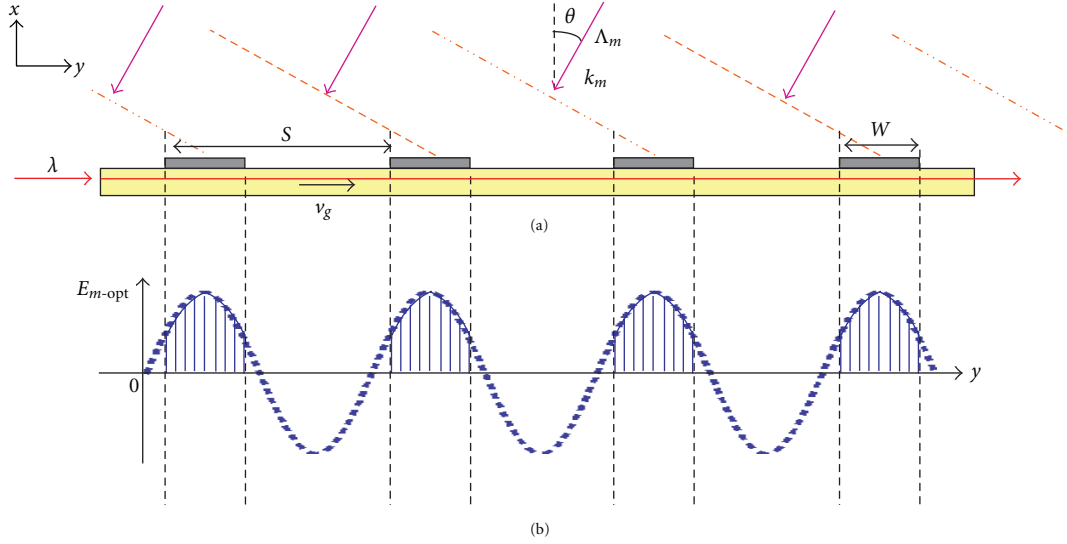


FIGURE 2: Operational principle of EO modulators. (a) Cross-sectional view under irradiation of a wireless microwave signal angle of θ degrees. (b) Microwave electric field observed by propagating lightwave along each gap-embedded patch-antenna. Modulation index corresponds to the shaded areas.

where k_m is the wave number of the microwave signal in vacuum ($k_m = \omega_m/c$), n_g is the group index of the lightwave propagating in the optical waveguide ($n_g = c/v_g$), v_g is the group velocity of the lightwave, c is the light velocity in vacuum, n_0 is the refractive index of the microwave in air ($=1$), and φ is an initial phase of the lightwave in the optical waveguide ($\varphi = k_m n_g y'$), corresponding to the phase of the microwave signal when the lightwave propagates in the optical waveguide.

For an array of gap-embedded patch-antennas as shown in Figure 2(a), the temporal phases of the microwave signal supplied to the gap-embedded patch-antennas are changed according to their separation, S , and the wireless irradiation angle, θ . The microwave electric field observed by the lightwave at h th gap-embedded patch-antennas, $E_{m\text{-opt}}^h$, can be expressed by

$$E_{m\text{-opt}}^h(y, \theta) = E_{m0} \sin[k_m n_g y + (h-1)S k_m n_0 \sin \theta + \varphi], \quad (3)$$

where

$$S = n v_g \frac{1}{\omega_m / 2\pi}, \quad (n: \text{integer}), \quad (4)$$

h denotes the number of the gap-embedded patch-antennas and S is a separation of the patch-antennas as shown in Figure 2.

The proposed device is an optical phase modulator. The modulation index is calculated from the integration of microwave electric field as would be observed by the

lightwave along the gap-embedded patch-antennas, it can be shown as

$$\Delta\phi(\theta) = \frac{\pi r_{33} n_e^3}{\lambda} \Gamma \sum_{h=1}^N \int_{(h-1)S}^{(h-1)S+W} E_{m\text{-opt}}^h(y, \theta) dy, \quad (5)$$

where λ is the wavelength of lightwave propagating in the optical waveguides, r_{33} is the EO coefficient, n_e is the extraordinary refractive index of the substrate, W are the width of the patch-antenna as the interaction length of the microwave and lightwave, N is the number of gap-embedded patch-antennas in the array structure, and Γ is a factor expressing the overlapping between the induced microwave electric field and the lightwave. The overlapping factor of the microwave and optical fields in the x - or z -components depends on the crystal orientation and optical field polarization. The modulation index of the proposed device corresponds to the sum of the shaded areas in Figure 2(b). Since the modulation index is also a function of wireless irradiation angle, θ , the directivity in the efficiency can be also calculated by (5).

4. Analysis

The details of the induced electric field across the gap in the proposed device using x -cut LiNbO₃ were analyzed. The device was designed for an operational frequency of 26 GHz. The thickness of the LiNbO₃ substrate was set as 0.5 mm. The size of the patch-antenna embedded with a 5 μm -wide gap was set to 0.7×1.3 mm for 26 GHz operation. The optical waveguide was designed 5 μm .

For comparison, an optical modulator with a gap-embedded patch-antenna using z -cut LiTaO₃ substrate was also analyzed. The thickness of the LiTaO₃ substrate was set

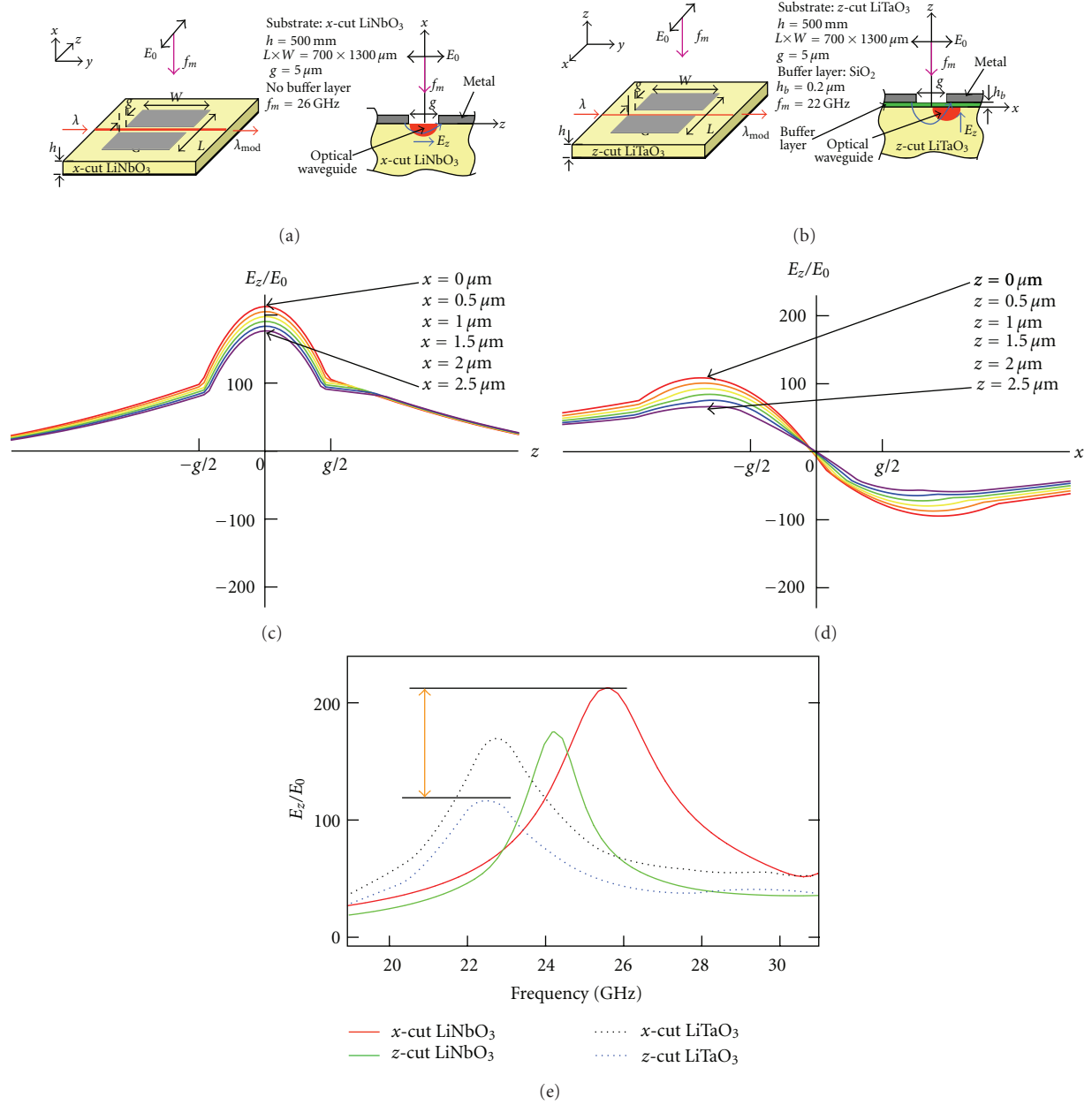


FIGURE 3: Microwave analysis of the optical modulators onto x -cut and z -cut of LiNbO_3 and LiTaO_3 substrates. (a) Structure of the device using x -cut LiNbO_3 . (b) Structure of the device using z -cut LiTaO_3 . (c) Calculated microwave electric field profile in the z -component for the device using x -cut LiNbO_3 . (d) Calculated microwave electric profile in the x -component for the device using z -cut LiTaO_3 . (e) Calculated frequency dependence of the maximum microwave electric for optical modulation.

as 0.5 mm. The size of the patch-antenna and gap were also set as $0.7 \times 1.3 \text{ mm}$ and $5 \mu\text{m}$, respectively. However, the corresponding operational frequency becomes slightly small as 22 GHz owing to the large dielectric constant of LiTaO_3 along the z -axis.

Figures 3(a) and 3(b) show the cross-sectional views of the device configuration using x -cut LiNbO_3 and z -cut LiTaO_3 substrates. For the device using x -cut LiNbO_3 substrate, there is no buffer layer and the optical waveguide is located at the centre of the gap on the surface of the substrate

as shown in Figure 3(a). For the device using z -cut LiTaO_3 substrate, there is a $0.2 \mu\text{m}$ -thick SiO_2 buffer layer and the optical waveguide is located under one side of the gap edge on the surface of the substrate as shown in Figure 3(b). The main microwave electric field components for driving EO effect are shown by the arrows in Figures 3(a) and 3(b), which are determined by the crystal orientation.

The microwave characteristics of the device were numerically analyzed using electromagnetic analysis software, HFSS. When a linearly polarized wireless microwave signal of E_0

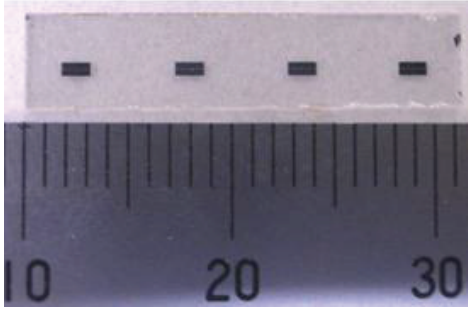


FIGURE 4: A photograph of a fabricated x -cut LiNbO_3 optical modulator using gap-embedded patch antennas before ground electrode fabrication.

perpendicular to the gap was irradiated to the devices, the microwave electric field profiles in the cross-section are shown in Figures 3(c) and 3(d). We can see that the strong microwave electric fields for optical modulation are obtained for device using: x -cut LiNbO_3 compared to z -cut LiTaO_3 -based device. We believe that these are due to the smaller dielectric constant and no buffer layer structure.

Figure 3(e) shows the calculated frequency dependence of the microwave electric field magnitude for optical modulation with the same patch-antennas size fabricated on different substrates, x -cut LiNbO_3 , z -cut LiNbO_3 , x -cut LiTaO_3 , and z -cut LiTaO_3 . They are indicated with colors of red, green, black, and blue, respectively. We can see that the largest electric field is induced for the x -cut LiNbO_3 device due to the smaller dielectric constant and no buffer layer structure. The peak resonant frequencies were slightly shifted owing to difference of dielectric constants in the LiNbO_3 and LiTaO_3 substrates.

The strong microwave electric field in the device using x -cut LiNbO_3 substrate can be used for optical modulation in the optical waveguide at the centre of the gap on the surface of the substrate. The modulation index can be calculated using (5). Considering the calculated microwave electric fields as shown in Figure 3(e), enhanced modulation index about two times can be obtained by using the x -cut LiNbO_3 device compared with the z -cut LiTaO_3 device, when the overlapping factor between the electric fields of the microwave and lightwave is almost same in both devices.

5. Experiments

The designed device was fabricated. First, a single-mode straight optical channel waveguide for the wavelength of $1.55 \mu\text{m}$ was fabricated by using titanium-diffused methods. A 4-element array of the gap-embedded patch-antennas were fabricated using a $1 \mu\text{m}$ -thick aluminum film on the substrate by use of thermal vapor deposition, a standard photolithography, and a lift-off technique. Finally, the reverse side of the device was covered using a $1 \mu\text{m}$ -thick aluminum film as a ground electrode. The photographs of the fabricated prototype device are shown in Figure 4.

The experimental setup for measuring basic operations of the fabricated device is shown in Figure 5. A $1.55 \mu\text{m}$

wavelength lightwave from a Distributed-Feed-Back (DFB) laser was passed through a lightwave polarizer and coupled to the fabricated device by use of an objective lens. A 26 GHz microwave signal from a microwave signal generator was irradiated to the fabricated device using a horn antenna with irradiated power of about 0.2 W. The output light spectrum was measured and monitored using an optical spectrum analyzer.

The examples of the output light spectra measured by an optical spectrum analyzer are shown in Figure 6, where the wireless microwave signal with frequency of 26 GHz was irradiated to the device normally ($\theta = 0$ degree). Figures 6(a) and 6(b) show measured output light spectra for the transverse electric (TE) and transverse magnetic (TM) modes of the lightwave, respectively, when a linearly-polarized wireless microwave signal with Z -polarization was irradiated. We can see that the optical modulation is more effective for TE-mode of the lightwave due to the larger EO effects in the z -direction of the LiNbO_3 . Figure 6(c) shows the output light spectrum when the polarization of the wireless microwave signal polarization was rotated with 90 degrees, which corresponds to Y -polarization. No optical sideband was observed for the Y -polarized wireless signal.

The measured frequency dependence of the modulation efficiency is shown by the dotted curve in Figure 7, when the irradiation angle of the wireless microwave signal was set normal to the device (0 degree) and the lightwave was set to TE-mode. The fabricated device was an optical phase modulator; therefore, a modulation index can be adopted as a measure for modulation efficiency. The modulation index can be calculated from the spectrum intensity ratio between the first sideband and the optical carrier as long as the modulation index value is rather smaller than unity. The peak frequency of the wireless microwave-optical conversion was about 25.7 GHz, which almost coincided with the calculated frequency dependence as shown by the red curve in Figure 7.

Figure 8 shows the measured dependence of modulation efficiency by the separation between the horn antenna and the fabricated device, S_d . The optical sidebands were observed with a range up to 1 m between the horn antenna and the device. In addition, the calculated far-field separation of ~ 80 mm for the fabricated device was obtained.

Figure 9 shows the measured irradiation angle dependence (directivity) of the fabricated device in the xy -plane. The measured directivity has good agreement with the theoretical calculation of the designed device.

The basic operations of the proposed device were demonstrated successfully. The enhanced modulation efficiency by 6 dB was obtained using the proposed x -cut LiNbO_3 optical modulators compared to the z -cut LiTaO_3 -based device as shown in Figure 10. The modulation efficiency of the proposed device can be enhanced further using photonic technology by the use of a sharp-cut optical filter and an optical amplifier [9].

In addition, the insertion loss of the device was measured approximately 11 dB by use of objective lenses as the lightwave coupling. They can be reduced by using optical fibers as the lightwave coupling. The insertion loss is not directly

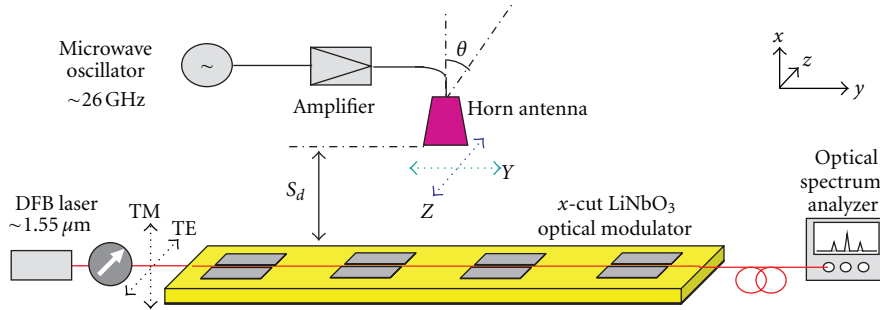


FIGURE 5: Experimental setup for measuring the operations of the fabricated optical modulators.

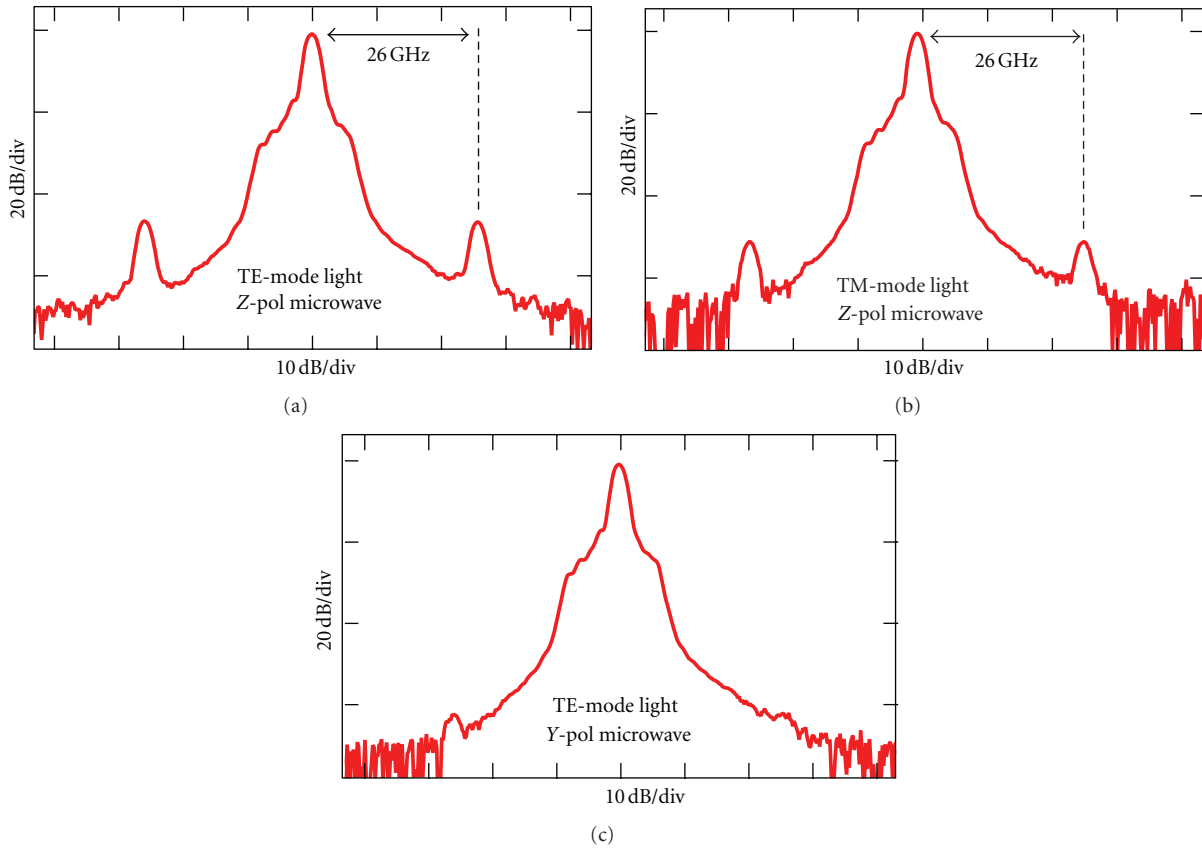


FIGURE 6: Measured output light spectra under microwave wireless signal irradiation of 26 GHz. (a) Output light spectrum for A-polarization of microwave signal and TE-mode of lightwave. (b) Output light spectrum for Z-polarization of microwave signal and TM-mode of lightwave. (c) Output light spectrum for Y-polarization of microwave signal and TE-mode of lightwave.

contributed to the modulation index of the device since the modulation index expresses by the spectrum intensity ratio between the first sideband and the optical carrier. However, low insertion loss is an important issue to realize low power consumption in the wireless-over-fiber system.

6. Conclusions

An x -cut LiNbO_3 optical modulator using gap-embedded patch-antennas was proposed for wireless microwave-lightwave signal conversion in the wireless-over-fibre systems. The proposed device is fabricated on x -cut LiNbO_3

substrate with no buffer layer structure. Modulation efficiency enhancement using the x -cut LiNbO_3 optical modulators can be obtained. The basic operations of the proposed device were demonstrated successfully. The modulation efficiency of the proposed device was enhanced by 6 dB compared to the z -cut LiTaO_3 -based device.

Wireless microwave/millimetre-wave-lightwave signal conversion with extremely low microwave/millimetre-wave signal distortion can be realized by the use of the proposed devices with simple compact structures. By using many gap-embedded patch-antennas in array structure with polarization-reversed structure of the x -cut LiNbO_3 for

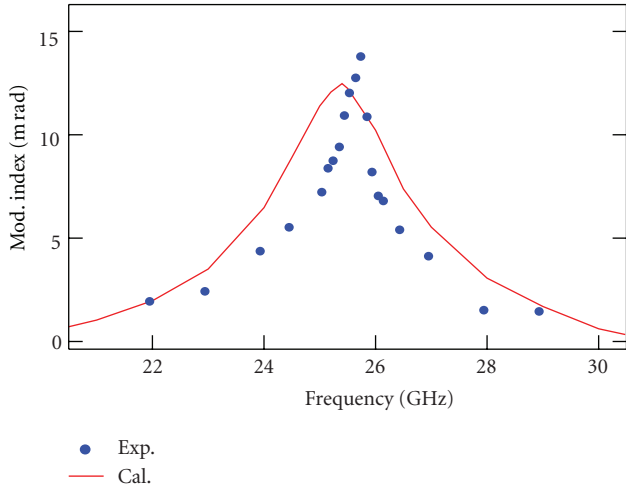


FIGURE 7: Measured frequency dependences of modulation efficiency with wireless irradiation angle of 0 degree (normal direction).

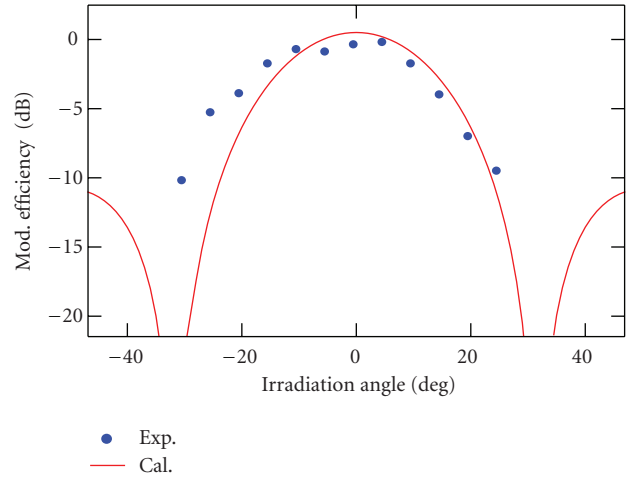


FIGURE 9: Measured wireless irradiation angle dependences (directivity) of modulation efficiency.

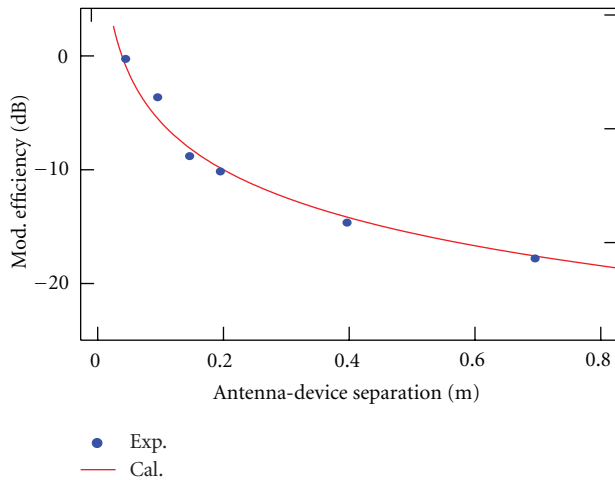


FIGURE 8: Measured antenna-device separation dependences of modulation efficiency.

obtaining quasiphase-matching structures, the modulation efficiency can be further enhanced.

Acknowledgments

The authors would like thanks to Dr. Hidehisa Shiomi and Dr. Kazuhiro Kitatani, from Osaka University, for their precious suggestions throughout the discussion and kind support in the experiment. This research was supported in part by the Grants-in-Aid for Scientific Research and the Grants for Osaka University Global COE Program, Center for Electronics Device Innovation, both from the Ministry of Education, Culture, Sports, Science, and Technology in Japan.

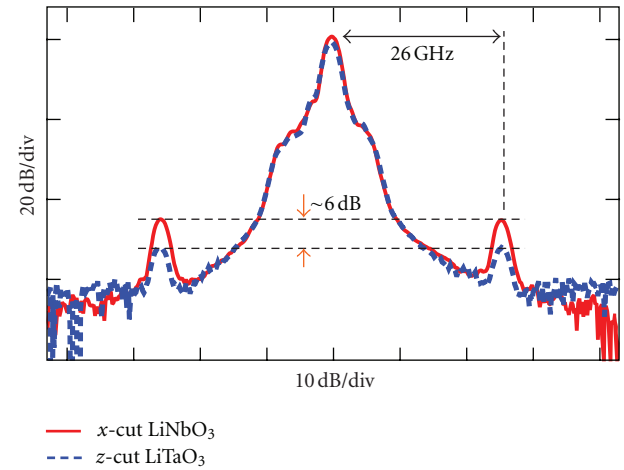


FIGURE 10: Comparison of measured output light spectra using the x-cut LiNbO₃ and z-cut LiTaO₃-based devices.

References

- [1] A. J. Seeds, "Microwave photonics," *IEEE Transactions on Microwave Theory and Techniques*, vol. 50, no. 3, pp. 877–887, 2002.
- [2] S. Iezekiel, *Microwave Photonics: Devices and Applications*, John Wiley & Sons, Chichester, UK, 2009.
- [3] I. Watanabe, T. Nakata, M. Tsuji, K. Makita, T. Torikai, and K. Taguchi, "High-speed, high-reliability planar-structure super-lattice avalanche photodiodes for 10-Gb/s optical receivers," *Journal of Lightwave Technology*, vol. 18, no. 12, pp. 2200–2207, 2000.
- [4] R. Krähenbühl, J. H. Cole, R. P. Moeller, and M. M. Howerton, "High-speed optical modulator in LiNbO₃ with cascaded resonant-type electrodes," *Journal of Lightwave Technology*, vol. 24, no. 5, pp. 2184–2189, 2006.
- [5] S. Shinada, T. Kawanishi, and M. Izutsu, "A resonant type linbo₃ optical modulator array with micro-strip antennas," *IEICE Transactions on Electronics*, vol. E90-C, no. 5, pp. 1090–1095, 2007.

- [6] R. B. Waterhouse and D. Novak, "Integrated antenna/electro-optic modulator for RF photonic front-ends," in *Proceedings of the International Microwave Symposium (WE2C-4 '11)*, Baltimore, Md, USA, June 2011.
- [7] F. T. Sheehy, W. B. Bridges, and J. H. Schaffner, "60 GHz and 94 GHz antenna-coupled LiNbO₃ electrooptic modulators," *IEEE Photonics Technology Letters*, vol. 5, no. 3, pp. 307–310, 1993.
- [8] W. B. Bridges, F. T. Sheehy, and J. H. Schaffner, "Wave-coupled LiNbO₃ electrooptic modulator for microwave and millimeter-wave modulation," *IEEE Photonics Technology Letters*, vol. 3, no. 2, pp. 133–135, 1991.
- [9] H. Murata, R. Miyanaka, and Y. Okamura, "Wireless space-division-multiplexed signal discrimination device using electro-optic modulator with antenna-coupled electrodes and polarization-reversed structures," *International Journal of Microwave and Wireless Technologies*, vol. 4, pp. 399–405, 2012.
- [10] Y. N. Wijayanto, H. Murata, and Y. Okamura, "Electro-optic wireless millimeter-wave-lightwave signal converters using planar Yagi-Uda array antennas coupled to resonant electrodes," in *Proceedings of the Optoelectronics and Communications Conference*, vol. 5E1-2, Busan, Republic of Korea, July 2012.
- [11] Y. N. Wijayanto, H. Murata, and Y. Okamura, "Novel electro-optic microwave-lightwave converters utilizing a patch antenna embedded with a narrow gap," *IEICE Electronics Express*, vol. 8, no. 7, pp. 491–497, 2011.
- [12] Y. N. Wijayanto, H. Murata, and Y. Okamura, "Electro-optic microwave-lightwave converters utilizing patch antennas with orthogonal gaps," *Journal of Nonlinear Optical Physics and Materials*, vol. 21, no. 1, Article ID 1250001, 2012.
- [13] Y. N. Wijayanto, H. Murata, and Y. Okamura, "Electro-optic microwave-lightwave converters utilizing a quasi-phase-matching array of patch antennas with a gap," *Electronics Letters*, vol. 48, no. 1, pp. 36–38, 2012.
- [14] G. Lefort and T. Razban, "Microstrip antennas printed on lithium niobate substrate," *Electronics Letters*, vol. 33, no. 9, pp. 726–727, 1997.
- [15] V. R. Gupta and N. Gupta, "Characteristics of a compact microstrip antenna," *Microwave and Optical Technology Letters*, vol. 40, no. 2, pp. 158–160, 2004.
- [16] R. Rodríguez-Berral, F. Mesa, and D. R. Jackson, "Gap discontinuity in microstrip lines: an accurate semianalytical formulation," *IEEE Transactions on Microwave Theory and Techniques*, vol. 59, no. 6, pp. 1441–1453, 2011.
- [17] R. E. Newnham, *Properties of Materials*, Oxford University Press, New York, 2005.
- [18] A. Yariv, *Quantum Electronics*, Wiley, New York, Ny, USA, 3rd edition, 1989.
- [19] H. Murata, S. Matsunaga, A. Enokihara, and Y. Okamura, "Resonant electrode guided-wave electro-optic phase modulator using polarisation-reversal structures," *Electronics Letters*, vol. 41, no. 8, pp. 497–498, 2005.

Research Article

Continuous Operation of a Bragg Diffraction Type Electrooptic Frequency Shifter at 16 GHz with 65% Efficiency

Shintaro Hisatake, Kenji Hattori, and Tadao Nagatsuma

Graduate School of Engineering Science, Osaka University, Toyonaka, Osaka 560-8531, Japan

Correspondence should be addressed to Shintaro Hisatake, hisatake@ee.es.osaka-u.ac.jp

Received 15 July 2012; Accepted 22 September 2012

Academic Editor: Borja Vidal

Copyright © 2012 Shintaro Hisatake et al. This is an open access article distributed under the Creative Commons Attribution License, which permits unrestricted use, distribution, and reproduction in any medium, provided the original work is properly cited.

We demonstrate for the first time the continuous operation of a Bragg diffraction type electrooptic (EO) frequency shifter using a 16 GHz modulation signal. Because frequency shifting is based on the Bragg diffraction from an EO traveling phase grating (ETPG), this device can operate even in the millimeter-wave (>30 GHz) range or higher frequency range. The ETPG is generated based on the interaction between a modulation microwave guided by a microstrip line and a copropagating lightwave guided by a planar waveguide in a domain-engineered LiTaO₃ EO crystal. In this work, the modulation power efficiency was improved by a factor of 11 compared with that of bulk devices by thinning the substrate so that the modulation electric field in the optical waveguide was enhanced. A shifting efficiency of 65% was achieved at the modulation power of 3 W.

1. Introduction

Coherent optical frequency conversion based on external modulation is an important technique not only for the optical communication and optical measurement but also for microwave and millimeter-wave photonics because it corresponds to an upconversion from RF to optical domain. Photomixing of two optical modulation sidebands generated by an electrooptic phase modulator (EOM) or a frequency comb generator has been used to generate low phase noise coherent microwaves or millimeter-waves, which are desirable for many applications such as the radar [1], sensing [2–4], and wireless communications [5]. The advantages of the external modulation method over other methods such as optical injection locking, optical phase-locked loop, and dual-wavelength laser source are the system's simplicity, stability, and frequency tunability. However, typical sinusoidal phase modulation is an inherently inefficient method of frequency conversion. At best, the fraction of the power in the first-order sideband generated by normal phase modulation is theoretically $(J_1(\beta))^2 \approx 34\%$, where $J_1()$ is a first-order Bessel function of the first kind and β is the modulation depth. The conversion efficiency of 34%

corresponds to an extra loss of about 5 dB. Because the noise figure (NF) of an optical amplifier is relatively poor compared to electronic amplifiers, extra loss due to a low conversion efficiency impacts most key aspects of microwave and millimeter-wave photonics in which low-loss 1550 nm components should be used [6, 7]. The lower conversion efficiency results in a lower carrier-to-noise ratio (CNR). The higher conversion efficiency is essential not only for microwave and millimeter-wave photonics applications but also for other photonic applications in which the system performance is governed by the CNR.

Recently, we proposed a new-type of EO frequency shifter and experimentally demonstrated the 16.25 GHz frequency shift with 82% efficiency [8]. The operation is based on the Bragg diffraction from an EO traveling phase grating (ETPG). Because the ETPG is produced based on the Pockels effect, this shifter can operate in the millimeter-wave (>30 GHz) range or in the higher frequency range. Moreover, multiplication of the frequency shift can be realized by cascading the ETPGs. We demonstrated a frequency shifting of ± 32.5 GHz with a 60% efficiency, using a 16.25 GHz modulation signal (doubler operation) [9]. Together with recent progressive high-speed modulation technologies [10],

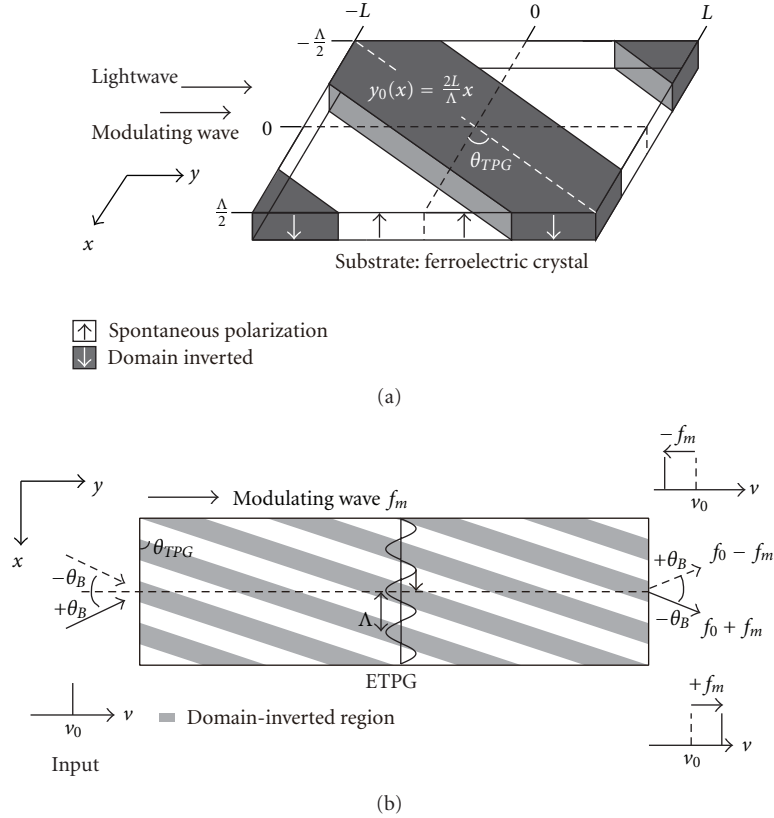


FIGURE 1: (a) Basic structure of the domain-inverted ferroelectric crystal. The width and the center position of the domain-inverted region are L and y_0 , respectively. (b) Schematic of the frequency shifting operation.

multiplication of the Bragg diffraction from the ETPG promises to realize the terahertz (>100 GHz) coherent link with high efficiency (more than Bessel function). However, bulk devices previously reported required relatively higher modulation power, typically several tens of watts at 16 GHz, therefore they were driven with pulsed magnetron.

In this paper, we demonstrate a waveguide-based frequency shifter in which the modulation power is significantly reduced compared with bulk shifters. A planar waveguide is fabricated using a conventional proton exchange method in a congruent LiTaO₃ (CLT) EO crystal [11]. The modulation electrode is a microstrip line. To improve the modulation efficiency, we reduced the thickness of the substrate, that is, the distance between the hot and ground electrodes, from 0.5 mm in the former bulk device to 0.1 mm.

In Section 2, the principle of the ETPG and frequency shifting are briefly summarized. Section 3 discusses the improvement of the modulation power efficiency by reducing the thickness of the substrate. In Section 4, we summarize the design and fabrication of the waveguide-based frequency shifter. Experimental results and discussions are summarized in Section 5.

2. Principle of the Frequency Shift Based on the ETPG

We briefly explain the principle of the frequency shift based on the ETPG. The ETPG is a time-varying phase distribution

within the optical beam cross-section produced by an interaction between the traveling modulation wave and the copropagating lightwave in a periodically domain-inverted (polarization-reversed) EO crystal. Figure 1(a) shows the basic structure of the domain-inverted EO crystal. The device is formed by repeating this basic structure and arranging the repeated structure in two dimensions on the x - y plane. When a lightwave with the group velocity of v_0 propagates along the y -axis with a collinear traveling modulation wave with the phase velocity of v_m in the crystal, the modulating electric field $E(y, t_0)$, which the lightwave entering the device at time t_0 encounters at position y , can be written as $E(y, t_0) = E_m \cos(2\pi f_m t_0 - \pi y/L)$, where E_m is the amplitude of the modulating wave, f_m is the modulation frequency, and $L = 1/(2f_m(1/v_m - 1/v_0))$. From this equation, we find that the traveling phase grating can be realized by setting the length and the center position of the domain-inverted region to be L and $y_0(x) = 2Lx/\Lambda$, respectively. The phase shift induced to a light passing through the length of $2L$ of this domain-inverted crystal, which is shown in Figure 1(a), is expressed as

$$\begin{aligned} \Delta\phi(x, t) &= \Delta\phi_m \sin\left(2\pi f_m t_0 + \frac{\pi y_0(x)}{L}\right) \\ &= \Delta\phi_m \sin(2\pi f_m t_0 + \beta x), \end{aligned} \quad (1)$$

where $\Delta\phi_m$ is the modulation index and $\beta = 2\pi/\Lambda$. This resultant phase distribution expresses a traveling sinusoidal

phase grating pumped by the electrical modulation signal. We refer to this time-varying phase distribution as the ETPG. Operation of the acousto-optic (AO) frequency shifter is based on the Bragg diffraction from the traveling phase grating pumped by an acoustic wave. Based on the analogy with the AO frequency shifter, we can realize the EO frequency shifter based on the Bragg diffraction from the ETPG [8].

The remarkable features of the ETPG are (1) the period of the ETPG is determined by the period (Λ) of the domain inversion in the x direction, not by the wavelength of the modulating wave, and (2) the traveling direction of the ETPG is determined by the sign of the β , that is, the sign of the tilting angle (θ_{TPG}) of the periodic domain inversion. The first feature allows the ETPG to operate at a higher modulation frequency even at the millimeter-wave frequency. The second feature allows us to cascade the ETPG to accumulate frequency shifting (multiplication) [9].

3. Improvement of the Modulation Power Efficiency

Although the proton exchange process might degrade the Pockels effect [12], in this section, we will confirm experimentally the effect of reducing the thickness of the substrate on the improvement of the modulation efficiency. We fabricated waveguide devices with four different thicknesses t and measured the modulation efficiency, which is defined as the modulation index per interaction length per modulation power (rad/mm/W). Figures 2(a) and 2(b) show a cross-section view of the conventional bulk device and the proposed waveguide device, respectively. The substrate is a congruent LiTaO₃ (CLT) EO crystal. The lightwave and modulation microwave propagate along the y direction. The traveling modulation microwave is guided by the microstrip line. The SiO₂ buffer layer is deposited on the waveguide before evaporating the hot electrode of the microstrip line to reduce propagation losses. The thickness of the buffer layer is about 0.1 μm . The depth of the waveguide is about 0.8 μm for single mode operation, which will be discussed later.

Figure 3 plots the modulation efficiency of the waveguide device for $t = 0.1, 0.15, 0.3, \text{ and } 0.5$ mm. The modulation efficiencies are normalized by the values obtained with the 0.5-mm bulk device. The dashed line is the theoretical function ($\propto 1/t^2$) fitted to the data. Because of the proton exchange process, the experimentally achieved modulation efficiency of the waveguide device was reduced to about 50% of that of the bulk device. The modulation efficiency improved inversely proportional to the square of the device thickness, t^2 . The modulation power efficiency of the 0.1-mm waveguide device was enhanced by a factor of 11 compared with that of 0.5-mm bulk devices.

4. Design and Fabrication of the Waveguide Frequency Shifter

Figure 4 schematically shows the waveguide frequency shifter. Periodic domain inversion was performed on a CLT

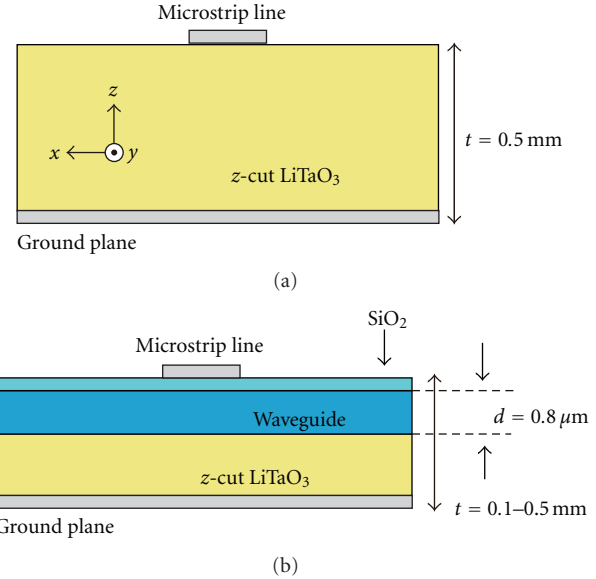


FIGURE 2: Schematic view of the frequency shifter. (a) Cross-section view of the conventional bulk device. (b) Cross-section view of the waveguide device.

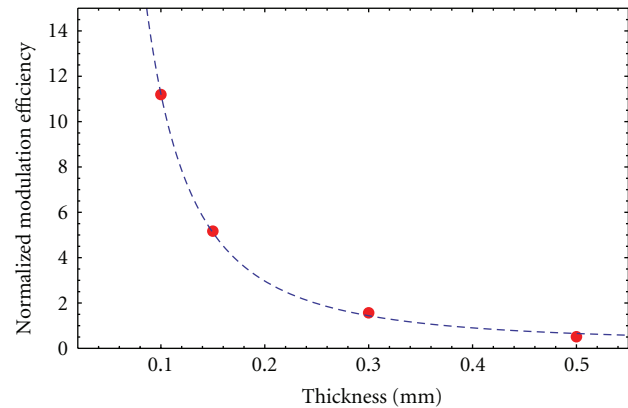


FIGURE 3: Modulation efficiency normalized by that of the 0.5-mm bulk device. The dashed curve is the theoretical curve fitted to the data.

substrate with the period of $\Lambda_p = 60 \mu\text{m}$. The interaction length was 34 mm. The thickness of the substrate was 0.1 mm. An extraordinary refractive index n_s and a group refractive index n_g of the CLT substrate were calculated to be $n_s = 2.21$ and $n_g = 2.41$, respectively, using the Sellmeier equation for 514.5 nm (Ar laser) [13]. The refractive index of the waveguide was measured to be $n_f = 2.26$. The refractive index of the SiO₂ buffer layer was also calculated to be 1.47, using the Sellmeier equation [14]. Using these refractive indices, the depth of the optical waveguide was designed to be $d = 0.8 \mu\text{m}$, based on mode calculation using effective index method to realize a single TM-guided mode operation.

The 0.8- μm waveguide was fabricated based on the standard proton exchange technique using melted benzoic acid. The temperature of the melted benzoic acid for

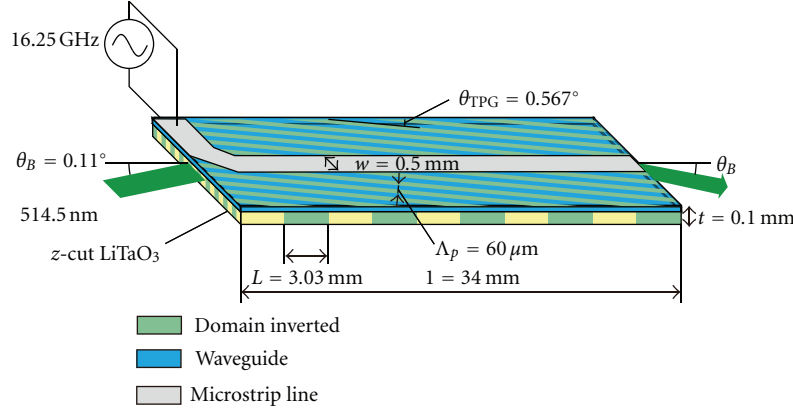


FIGURE 4: Schematic view of the waveguide frequency shifter.

the proton exchange was set at 240 degrees Celsius. The relation between the exchanging time (t_{ex}) and the depth (d) of the waveguide can be expressed as $d = 2\sqrt{D_{ex}t_{ex}}$, where $D_{ex} = 8.41 \times 10^{-2}(\mu\text{m}^2/\text{h})$ [15]. The exchanging time was set to 2 hours. After the exchanging, the device was thermally annealed for 30 minutes at 400 degrees Celsius to reduce the propagation losses and recover the Pockels effect.

The effective relative permittivity for the modulation microwave should be calculated to determine the half period L of the domain inversion. We calculated the effective relative permittivity using an electromagnetic field simulator (method of moments). Figure 5 shows the results. The filled circles represent results of the simulations without SiO_2 buffer layer. The solid line is calculated using the accurately approximate formula for isotropic substrate [16]. The formula is well fitted to the simulated results, therefore the effective relative permittivity with the SiO_2 buffer layer can be calculated through the simulation (open circles in Figure 3). From the simulated result, the phase velocity of the modulation microwave for $t = 0.1 \text{ mm}$ substrate can be determined to be $v_m = 5.48 \times 10^7 \text{ m/s}$. Together with the group velocity of the optical wave, the half period of the domain inversion for $t = 0.1 \mu\text{m}$ is determined as $L = 3.03 \text{ mm}$ using (1).

The tilting angle of the domain inversion was $\theta_{\text{TPG}} = \arcsin(\Lambda_p/(2L)) = 0.567^\circ$. The Bragg angle was $\theta_B = \arcsin(\lambda/(2\Lambda)) = 0.11^\circ$, where λ is the wavelength of the optical wave in the crystal and $\Lambda = \Lambda_p/\sqrt{1 - (\Lambda_p/(2L))^2}$.

5. Experimental Results and Discussion

The frequency of the modulation signal was 16.25 GHz, which was supplied from a signal generator and amplified by a commercially available power amplifier (R&K: AA380). The available maximum modulation power was 3 W.

Figure 6 shows the frequency-resolved far-field pattern of the output beam. The frequency of the output beam is resolved to the vertical direction with the diffraction grating and the Fourier transform mirror, therefore the horizontal axis is space, whereas the vertical axis corresponds to the frequency. The modulation power was about 1.7 W.

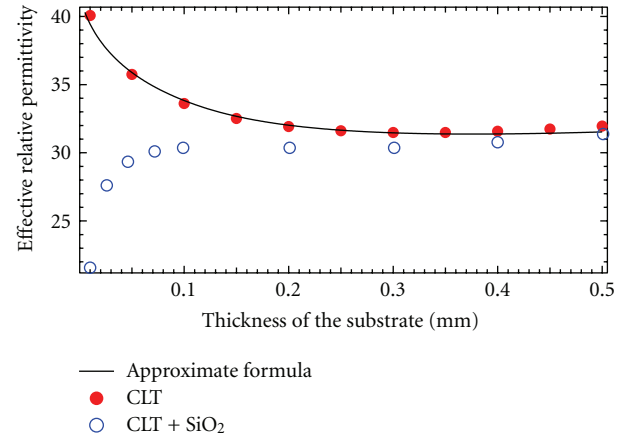


FIGURE 5: Effective relative permittivity of the microstrip line. Filled and open circles are calculated based on the electromagnetic field simulator (method of moments) for the substrate of CLT only and CLT with SiO_2 buffer layer, respectively. The solid curve is calculated using an accurately approximate formula for the isotropic substrate.

We observed two optical beam spots resolved in both space and frequency. The frequency of the 1st diffracted component was shifted by 16.25 GHz and there were no unwanted components at this modulation power. We define the frequency shifting efficiency as the output power ratio of the 1st order diffracted components to the whole output optical power. A frequency shifting efficiency of about 50% was achieved at the modulation power of 1.7 W.

Figure 7 shows the diffraction efficiency of the 1st order of the diffracted component as a function of the square root of the modulation power. The dashed curve is the theoretical curve fitted to the data. A diffraction efficiency of about 65% was achieved at the modulation power of 3 W. About 35% of the optical power was observed in other diffracted components, such as 1st and 2nd order diffracted components. From the fitting, we conclude that the maximum diffraction efficiency can be achieved at the modulation power of 3.6 W.

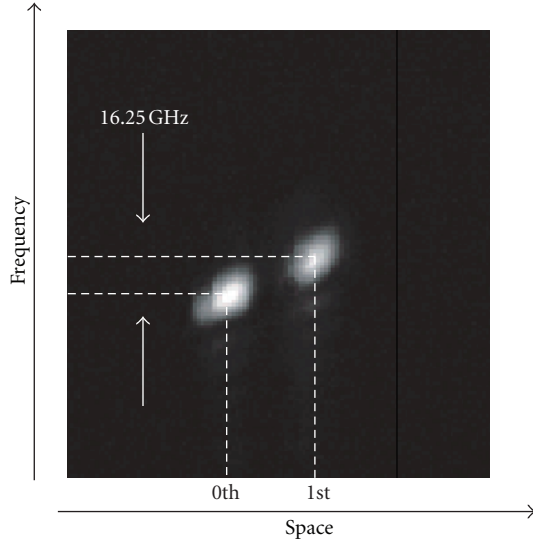


FIGURE 6: Far-field pattern of the output beam with resolved frequency. The horizontal axis is space. The vertical axis corresponds to the frequency.

Previously, we achieved the maximum diffraction efficiency at the modulation power of about 300 W for the interaction length of 12.5 mm in the 0.5-mm bulk device [9]. Compensating the difference of the interaction length, the power efficiency of the current waveguide device should be improved by a factor of 84, which corresponds to the expected modulation power of 3.8 W. The achieved value of 3.6 W is close to this predicted value.

On the other hand, the maximum diffraction efficiency we achieved with the 0.5-mm bulk device was 82% [8]. The degradation of the diffraction efficiency might be due to the degradation of the Q factor of the device. The boundary between the Bragg regime and Raman-Nath regime can be described in terms of the so-called Q factor, given by $Q = 2\pi\lambda l/\Lambda^2$. The Q factor of the current waveguide device was 13.5, whereas that of the former bulk device was 23. Shortening the period of the domain inversion will recover the diffraction efficiency.

We confirmed experimentally the improvement of the modulation power efficiency at 514.4 nm by reducing the gap distance between the hot and ground electrode of the microstrip line. Operation of the shifter at 1550 nm requires further improvement of the modulation power efficiency, by factor of 9. It can be achieved by narrowing the gap to about 0.03 mm for a 34-mm-long device. The 0.03-mm-thick device can be fabricated by the mechanical polishing with the proton exchange process. Crystal ion slicing and wafer bonding (smart guide) [17] is another technique to fabricate the thin-film device without degradation of the optical quality compared with the bulk crystal. Rabiei and Steier demonstrated a LiNbO₃ waveguide modulator at 1550 nm with a low propagation loss in which the waveguide was fabricated using the smart guide [18]. Using Sellmeier equation, the group refractive index is calculated to be about 2.17 for 1550 nm, which requires slight modification of the

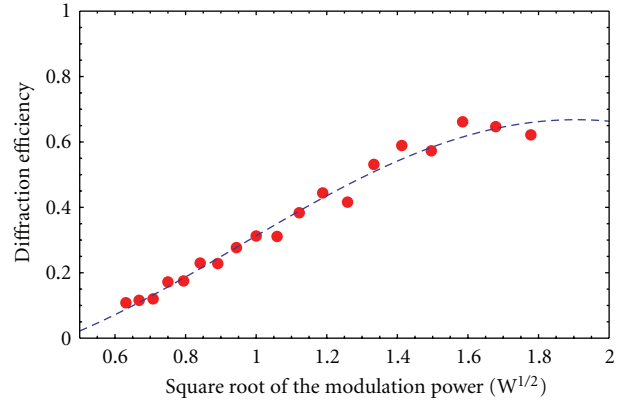


FIGURE 7: Diffraction efficiency as a function of the square root of the modulate power. The filled circles show the experimental data. The dashed curve shows the theoretical curve fitted to the data.

period of the domain inversion for the QVM condition. On the other hand, the propagation characteristics of a thin-film microstrip line can be calculated using equivalent-circuit model [19]. The effective relative permittivity for the 0.03-mm-thick microstrip line with the SiO₂ buffer layers is estimated to be about 28. Using calculated values of the group refractive index for 1550 nm and the effective relative permittivity, the modified half-period of the periodic domain inversion is calculated to be 2.96 mm. The Q factor of the device with 60 μ m domain inversion at 1550 nm will be about 40, which promises the frequency conversion efficiency of more than 80% [8]. It is feasible to implement the frequency shifter for the 1550 nm band operating at 16 GHz with more than 80% efficiency.

Improvement of the modulation power efficiency will increase the operation frequency of the device. The thin-film microstrip line supports the THz wave transmission, although stronger attenuation appears above 300 GHz, which is caused by an increasing amount of radiation loss [20]. A 2 W Q-band (30 to 50 GHz) power amplifier is commercially available. Our technique would promise to fabricate the low-loss upconverter which connects the millimeter-wave and 1550 nm optical wave.

6. Conclusion

We proposed waveguide-based frequency shifter, in which modulation power efficiency is improved by a factor of 11 compared with the conventional bulk device. At the modulation power of 3 W, we achieved a frequency shifting of 16.25 GHz with the efficiency of 65%. Improvement of the modulation power efficiency enabled us to demonstrate the continuous operation of the shifting.

Acknowledgment

This research was partially supported by a Grant from the Grant-in-Aid for Challenging Exploratory Research (23656049) from the Ministry of Education, Culture, Sports, Science, and Technology of Japan and a Grant Program

from the Feasibility Study Stage in Adaptable and Seamless Technology Transfer Program (FS-stage, A-STEP).

References

- [1] Ze Li, X. Zhang, H. Chi, S. Zheng, X. Jin, and J. Yao, "A reconfigurable microwave photonic channelized receiver based on dense wavelength division multiplexing using an optical comb," *Optics Communications*, vol. 285, pp. 2311–2315, 2012.
- [2] D. J. Lee and J. F. Whitaker, "Bandwidth enhancement of electro-optic sensing using high-even-order harmonic sidebands," *Optics Express*, vol. 17, no. 17, pp. 14909–14917, 2009.
- [3] M. Tsuchiya, K. Sasagawa, A. Kanno, and T. Shiozawa, "Live electrooptic imaging of W-band waves," *IEEE Transactions on Microwave Theory and Techniques*, vol. 58, no. 11, pp. 3011–3021, 2010.
- [4] H. J. Song, N. Shimizu, T. Furuta, K. Suizu, H. Ito, and T. Nagatsuma, "Broadband-frequency-tunable sub-terahertz wave generation using an optical comb, AWGs, optical switches, and a uni-traveling carrier photodiode for spectroscopic applications," *Journal of Lightwave Technology*, vol. 26, no. 15, pp. 2521–2530, 2008.
- [5] A. Hirata, T. Kosugi, H. Takahashi et al., "120-GHz-band millimeter-wave photonic wireless link for 10-Gb/s data transmission," *IEEE Transactions on Microwave Theory and Techniques*, vol. 54, no. 5, pp. 1937–1942, 2006.
- [6] T. K. Woodward, A. Agarwal, T. Banwell et al., "Systems perspectives on optically-assisted RF signal processing using silicon photonics," in *Proceedings of the IEEE International Topical Meeting on Microwave Photonics*, pp. 377–380, October 2011.
- [7] A. Agarwal, T. Banwell, and T. K. Woodward, "Optically filtered microwave photonic links for RF signal processing applications," *Journal of Lightwave Technology*, vol. 29, no. 16, Article ID 5957251, pp. 2394–2401, 2011.
- [8] K. Shibuya, S. Hisatake, and T. Kobayashi, "10-GHz-order high-efficiency electrooptic frequency shifter using slant-periodic domain inversion," *IEEE Photonics Technology Letters*, vol. 16, no. 8, pp. 1939–1941, 2004.
- [9] S. Hisatake, T. Konishi, and T. Nagatsuma, "Multiplication of optical frequency shift by cascaded electro-optic traveling phase gratings operating above 10 GHz," *Optics Letters*, vol. 36, no. 8, pp. 1350–1352, 2011.
- [10] M. Chaciski and U. Westergren, "100 GHz electro-optical modulator chip," in *Proceedings of the Optoelectronics and Communications Conference (OECC '11)*, pp. 59–60, 2011.
- [11] K. Tada, T. Murai, T. Nakabayashi, T. Iwashima, and T. Ishikawa, "Fabrication of LiTaO₃ optical waveguide by H⁺ exchange method," *Japanese Journal of Applied Physics, Part 1*, vol. 26, no. 3, pp. 503–504, 1987.
- [12] I. Savatinova, S. Tonchev, R. Todorov, M. N. Armenise, V. M. N. Passaro, and C. C. Ziling, "Electro-optic effect in proton exchanged LiNbO₃ and LiTaO₃ waveguides," *Journal of Lightwave Technology*, vol. 14, no. 3, pp. 403–409, 1996.
- [13] K. S. Abedin and H. Ito, "Temperature-dependent dispersion relation of ferroelectric lithium tantalate," *Journal of Applied Physics*, vol. 80, no. 11, pp. 6561–6563, 1996.
- [14] C. M. Herzinger, B. Johs, W. A. McGahan, J. A. Woollam, and W. Paulson, "Ellipsometric determination of optical constants for silicon and thermally grown silicon dioxide via a multi-sample, multi-wavelength, multi-angle investigation," *Journal of Applied Physics*, vol. 83, no. 6, pp. 3323–3336, 1998.
- [15] P. J. Matthews, A. R. Mickelson, and S. W. Novak, "Properties of proton exchange waveguides in lithium tantalate," *Journal of Applied Physics*, vol. 72, no. 7, pp. 2562–2574, 1992.
- [16] M. Kobayashi and R. Terakado, "Accurately approximate formula of effective filling fraction for microstrip line with isotropic substrate and its application to the case with anisotropic substrate," *IEEE Transactions on Microwave Theory and Techniques*, vol. 27, no. 9, pp. 776–778, 1979.
- [17] P. Rabiei and P. Gunter, "Optical and electro-optical properties of submicrometer lithium niobate slab waveguides prepared by crystal ion slicing and wafer bonding," *Applied Physics Letters*, vol. 85, no. 20, pp. 4603–4605, 2004.
- [18] P. Rabiei and W. H. Steier, "Lithium niobate ridge waveguides and modulators fabricated using smart guide," *Applied Physics Letters*, vol. 86, no. 16, Article ID 161115, pp. 1–3, 2005.
- [19] F. Schnieder and W. Heinrich, "Model of thin-film microstrip line for circuit design," *IEEE Transactions on Microwave Theory and Techniques*, vol. 49, no. 1, pp. 104–110, 2001.
- [20] M. Nagel, T. Dekorsy, M. Brucherseifer, P. Haring, and B. H. Kurz, "Characterization of polypropylene thin-film microstrip lines at millimeter and submillimeter wavelengths," *Microwave and Optical Technology Letters*, vol. 29, no. 2, pp. 97–100, 2001.

Research Article

Photonic Heterodyne Pixel for Imaging Arrays at Microwave and MM-Wave Frequencies

Á. R. Criado,¹ J. Montero-dePaz,² C. de Dios,¹ L. E. García,² D. Segovia,² and P. Acedo¹

¹Electronics Technology Department, Universidad Carlos III de Madrid, 28911 Leganés, Spain

²Grupo de Radiofrecuencia (GRF), Universidad Carlos III de Madrid, 28911 Leganés, Spain

Correspondence should be addressed to P. Acedo, pag@ing.uc3m.es

Received 27 June 2012; Accepted 13 September 2012

Academic Editor: Borja Vidal

Copyright © 2012 Á. R. Criado et al. This is an open access article distributed under the Creative Commons Attribution License, which permits unrestricted use, distribution, and reproduction in any medium, provided the original work is properly cited.

The use of photonic heterodyne receivers based on semiconductor optical amplifiers to be used in imaging arrays at several GHz frequencies is evaluated. With this objective, a 3×3 imaging array based on such photonic pixels has been fabricated and characterized. Each of the receiving optoelectronic pixels is composed of an antipodal linear tapered slot antenna (LTSA) that sends the received RF signal directly to the electrical port of a semiconductor optical amplifier (SOA) acting as the optoelectronic mixer. Both the local oscillator (LO) and the intermediate frequency (IF) signals are directly distributed to/from the array pixels using fiber optics, that allows for remote LO generation and IF processing to recover the image. The results shown in this work demonstrate that the performances of the optoelectronic imaging array are similar to a reference all-electronic array, revealing the possibility of using this photonic architecture in future high-density, scalable, compact imaging arrays in microwave and millimeter wave ranges.

1. Introduction

Microwave photonics and radio-over-fiber (RoF) techniques have been used in antenna arrays for some years now typically associated with local oscillator (LO) distribution and remote intermediate frequency (IF) processing [1]. The advantages usually associated with the use of such techniques are the high bandwidth capabilities, the electromagnetic interference (EMI) immunity, the extremely low transmission losses when using optical fibers, and the possibilities of including signal processing features, like true local time delay (TTD) [2] or optical beam forming [3]. Their advantages are also associated with the availability of optical/photonic devices in the telecom wavelength range which, due to the growth of the optical communications in the last decades, provide us with high-performance, wide-variety, compact, and low-cost (COTS) optical components suitable for its use in microwave photonics and RoF.

Following this trend, new functionalities based on photonic processing of RF are becoming available to be incorporated into arrays beyond optical signal distribution. In this sense, a major contribution to obtain high-density

receiving arrays based on photonic techniques would be the obtaining of a photonic heterodyne receiver able to perform directly the mixing of the LO (photonic distributed) and the received RF with high sensitivity. This all-optical pixel would reduce the several electrooptical (EO) conversions typical to conventional RoF systems and would be able to be integrated directly into the mature optical signal distribution architectures already available. In order to obtain such heterodyne optoelectronic RF detector, several mixing techniques have been already proposed using components as Mach-Zehnder modulators [4], electroabsorption modulators [5], or dual-mode monolithic laser sources [6] that show polarization dependence or low conversion efficiencies. Recently, semiconductor optical amplifiers (SOAs) have also been proposed as optoelectronic mixers [7–10]. Optical mixing using SOAs has been demonstrated both in all-optical [9, 10] and electrooptical (EO) configurations [7, 8]. In the EO approach, which is the most interesting in terms of obtaining a photonic heterodyne mixer, one of the electrical signals involved (i.e., the local oscillator (LO) or the radio-frequency (RF)) is modulated onto an optical carrier that is delivered to the optical input of the SOA. The other electrical

signal is directly applied to the electrical port of the SOA modulating its bias voltage. Both downconversion [8] and upconversion [7] have been reported.

One of the fields these all-optical pixel-based receiving arrays will have a great impact on is microwave and millimeter wave imaging. These techniques have been successfully demonstrated for a variety of applications like nondestructive testing [11], medical imaging [12], and security applications [13]. Usually these systems, working either in near field or far field, have their pixel elements multiplexed in the RF level into a single receiver to obtain reasonable size systems. Recently, a portable real-time camera at 24 GHz based on this strategy has been reported [14], but although the speed is reasonably good (22 frames per second) the resolution (24×24 pixels) is still far to be the required for the applications mentioned above, especially if we address the necessity of obtaining a portable (low-size and -weight) device.

In this sense, the incorporation of all-optical RF receiving pixel-based photonic mixing techniques [15] to imaging arrays will have a major impact on the resulted size, weight, and power consumption of the system. The high integration potential associated to PICs (photonic integrated circuits) [16] allows also for the integration on the same substrate of all the required functionalities necessary to process RF frequencies in the optical domain. Nowadays, several high-functionality PICs have already been reported [17], especially for optical communication purposes, demonstrating that the technology is already mature to implement other functionalities.

With this aim, in this work we present a three by three element (3×3) imaging array based on a heterodyne optoelectronic pixel based on an electrooptical (EO) ultra nonlinear mixer using an ultra nonlinear semiconductor optical amplifier (XN-SOA) [15]. This XN-SOA EO mixer presents a direct RF electrical input provided by an antipodal linear tapered slot antenna (LTSA) [18]. The LO is optically introduced at the optical input of the XN-SOA, and the IF is also optically delivered at its output, allowing for remote photonic LO generation and remote IF processing over optical fiber. Both, the mixing scheme and the used antenna make up a compact, low-cost, and flexible receiving heterodyne antenna that offers good scalability properties for imaging array applications. In this work, first imaging results using the heterodyne optoelectronic pixel 3×3 array are presented. Although the imaging system presented in this paper works at a relatively low frequency (13 GHz), the high bandwidth associated to the photonic components already available for optical communications opens the possibility to scale the presented architecture to higher (millimeter wave) frequencies.

2. Description and Characterization of the Heterodyne Optoelectronic Pixel for Imaging Arrays

2.1. Heterodyne Optoelectronic Pixel Fundamentals. The core of the reported photonic imaging array is an ultra nonlinear

semiconductor optical amplifier (XN-SOA) based heterodyne pixel receiver that makes our system compact and cost-effective. The scheme is depicted in Figure 1 [15]. The LO signal (f_{LO}) is applied to a distributed feedback (DFB) diode laser (QPhotonics QDFBLD-1550-50) that works under gain switching conditions [19], allowing for the modulation of the optical carrier without external modulators. The photonic LO produced has an optical frequency comb-like spectra [15] that is distributed to the heterodyne receiver using a fiber link (Figure 1(a)). The LO is then coupled to the optical input of the ultra nonlinear SOA (CIP SOA-XN-OEC-1550), where the EO mixing process takes place when the RF electrical signal (f_{RF}) introduced into the electrical port of the XN-SOA modulates its bias point. The XN-SOA device has a small signal gain of 20 dB at 150 mA bias current and a maximum saturated optical output power of 13 dBm. The obtained IF appears modulating the optical carrier at the output of the XN-SOA (Figure 1(c)) and is recovered at the end of the optical downlink using a high bandwidth photodiode (u2t XPDV2120R) followed by a low-pass filter. This scheme is cost-effective and takes advantage of the additional nonlinearities of the mixer and its polarization independence compared to other schemes already proposed [7, 8].

It is important to note in this scheme that no external modulator is used for the photonic LO generation and neither a laser nor an external modulator is needed for modulating the RF signal onto an optical carrier for the mixing process. Moreover, no optical coupler is required to add the optical signals containing LO and RF prior to the SOA input, as it is typical to previous reported schemes [9]. In this way, most devices usually employed in typical RoF architectures are avoided, thus having a much more compact and cost-effective configuration, allowing for easier integration onto a single PIC. The proposed approach, with the LO and the IF distributed over fiber, results in an especially suitable strategy for scaled and flexible signal distribution in large array applications.

2.2. Heterodyne Optoelectronic Pixel Description. The optoelectronic heterodyne pixel incorporates to the EO mixing scheme described above for heterodyne RF detection, a broadband antenna to provide the XN-SOA with an impedance as constant as possible along its broad working band. For this reason an antipodal linear tapered slot antenna (LTSA) [18] has been selected (Figure 2). As a substrate, Rogers Duroid 5880, with $\epsilon_r = 2.2$ and 0.787 mm thickness, has been chosen. In Figure 2, we see how the antenna collects the RF signal that is directly delivered to the bias port of the XN-SOA of Figure 1. The optical signal at the output of the XN-SOA, that contains the IF, is delivered over optical fiber to the remote IF-processing stage, where a photodiode performs the conversion from optical to electrical domain.

2.3. Heterodyne Optoelectronic Pixel Characterization. The characterization of the heterodyne pixel must include both the evaluation of the performances of the photonic mixing scheme (Figure 1) and the antenna (Figure 2). The parameter

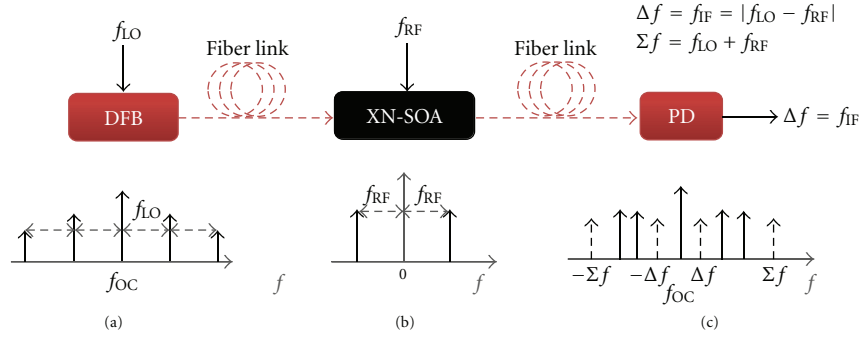


FIGURE 1: EO mixing concept using an ultra nonlinear SOA. (a) Optical output of GS DFB laser; (b) electrical signal modulating the XN-SOA bias; (c) optical output of the XN-SOA (only sum and difference terms are represented).

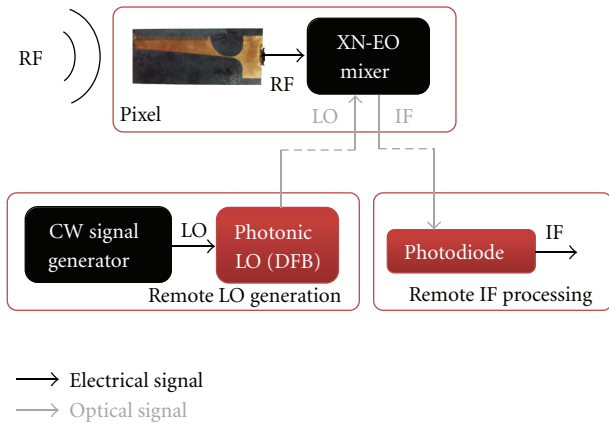


FIGURE 2: Heterodyne photonic receiving antenna setup.

we have used to evaluate the performance of the photonic mixer has been the downconversion ratio (Figure 3), defined for optoelectronics mixers as the ratio between the electrical power of the downconverted signal at f_{IF} (output of the photodiode) and the electrical power of the RF signal present after mixing at f_{RF} [9]. An analysis of the frequency dependence of the downconversion ratio has been performed sweeping both f_{LO} and f_{RF} up to 15 GHz. The bias current applied to the DFB is 40 mA, for an average optical power around 5 mW. The XN-SOA is biased at 150 mA (saturation) and shows an average optical output power of 10 mW. The regions with better (higher) conversion ratios appear for RF frequencies in the ~4 to 13 GHz range and LO frequencies below 4 GHz. When both frequencies (LO and IF) are close to each other, the conversion ratio falls as expected (homodyne operation).

As mentioned before, the broadband antenna design selected for the receiver pixels is an antipodal LTSA [18] that includes a number of corrugations in order to make the beam symmetric and improve its radiation pattern [20]. The characterization of the antenna started with the measurement of the reflection coefficient. In Figure 4, we show the reflection coefficient for the LTSA demonstrating a working frequency band from 7 GHz to 20 GHz with the

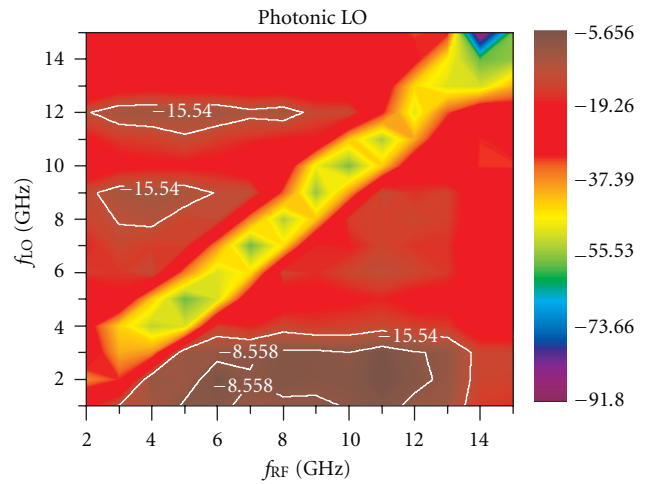


FIGURE 3: Downconversion ratios in dB for the photonic mixer. Contour lines represent 3 dB and 10 dB bandwidth.

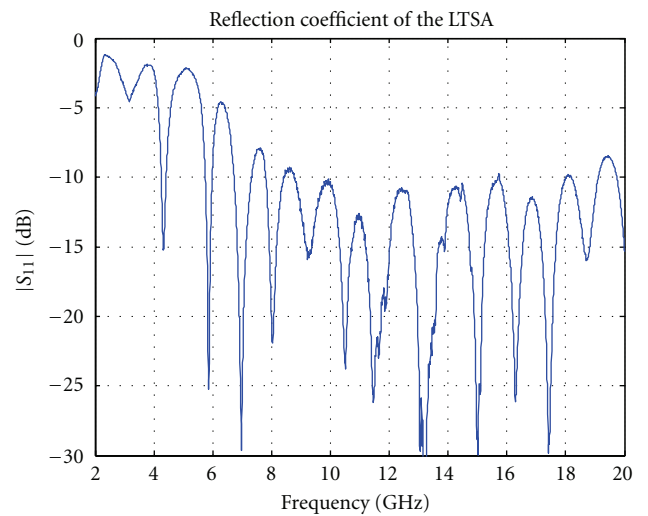


FIGURE 4: Measured reflection coefficient of the manufactured LTSA.

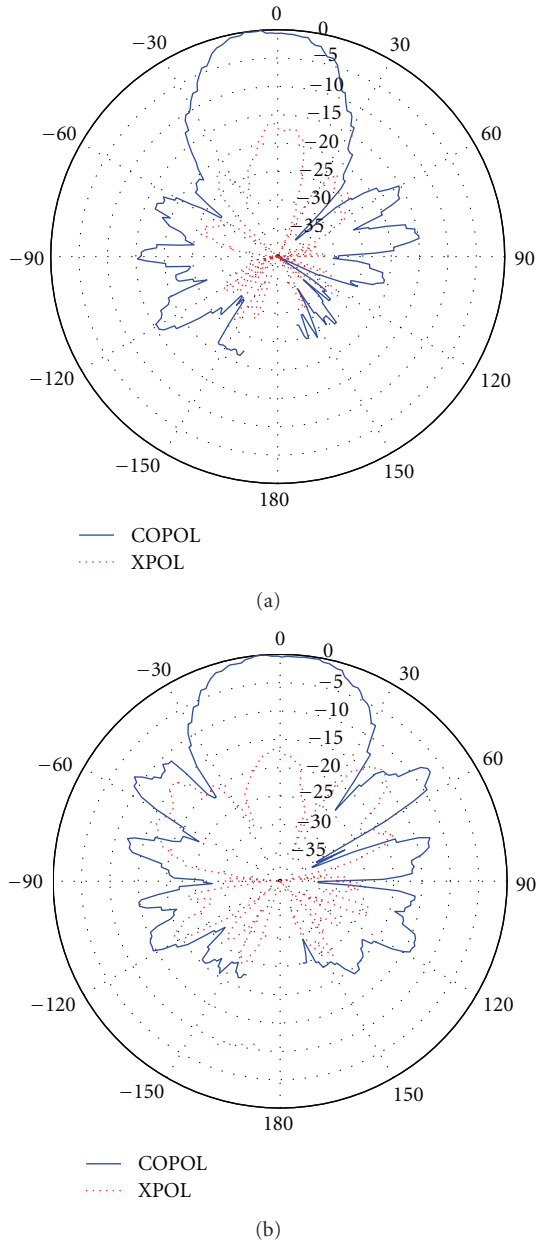


FIGURE 5: Antipodal LTSA radiation pattern (measured at 13 GHz).

desired relatively constant impedance presented to the XN-SOA over frequency. Also the radiation pattern has been measured, as shown in Figure 5, where such radiation pattern at 13 GHz is displayed as an example of how each of the elements of the array radiates. This antenna has a directivity in the whole band around 9 dBi-10 dBi.

3. Imaging Array Description and Experimental Setup

The final objective of this work is to validate the use of the introduced optoelectronic pixel for heterodyne RF detection in imaging arrays incorporating the advantages of remote

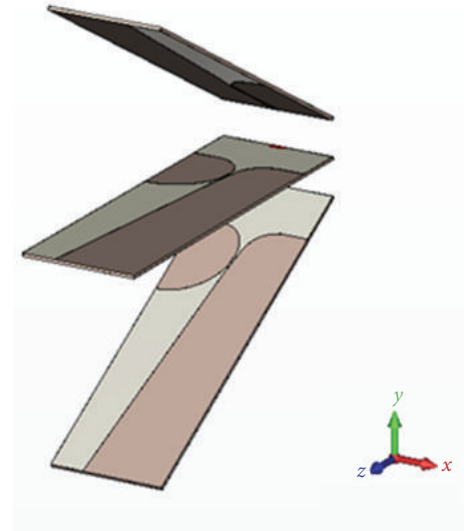


FIGURE 6: 3×1 Subarray based on antipodal LTSAs.



FIGURE 7: Picture of the actual 3×3 array inside the anechoic chamber.

photonic LO and IF distribution and the high integration capability of photonic circuits. For this reason, a 3×3 element array has been designed and fabricated based on the pixel described above to proof the concept. The 3×3 array design is based on three 3×1 subarray elements as shown in Figure 6, where we can see the LTSA radiant elements chosen for the pixels. Upper and lower elements are tilted 30° with respect to the central element in order to scan different directions and provide faster scanning capabilities. The final array built is shown in Figure 7, where we can see the actual appearance of the array made of the subarrays of Figure 5. A $130 \times 110 \times 70$ mm PVC box has been designed to hold the complete array and provide the desired tilt to the antennas. Each horizontal subarray (Figure 6) is formed by 3 LTSAs printed on a 110×100 mm Rogers Duroid 5880 substrate separated 30 mm from each other. Each subarray

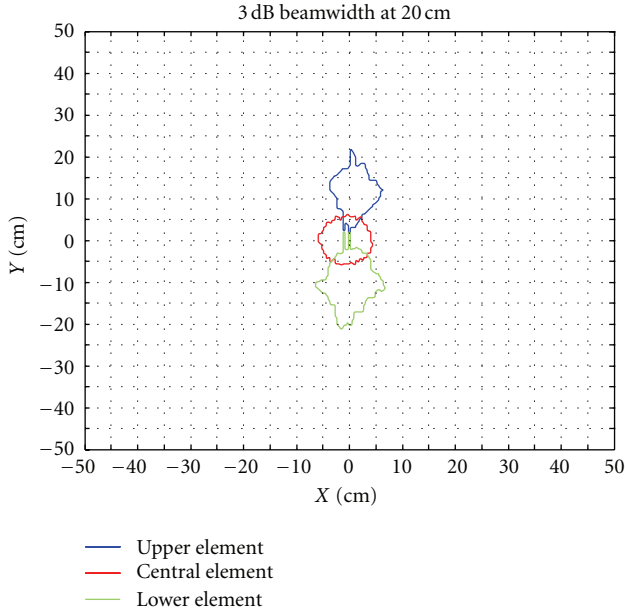


FIGURE 8: Beam spot diameter at 20 cm from the subarray from Figure 6. Working frequency 13 GHz.

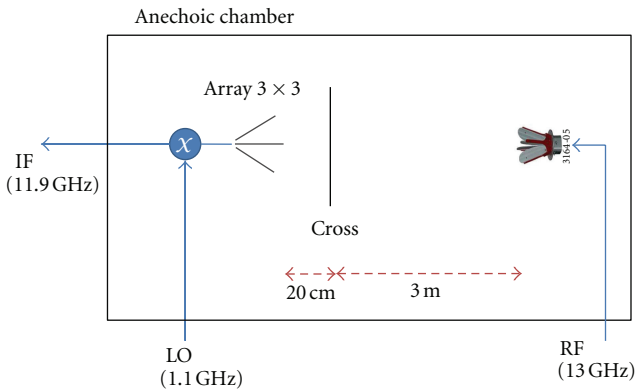


FIGURE 9: Imaging experiment (see text for details).

has been manufactured with a LPKF ProtoLaser S laser milling machine.

As mentioned briefly in the introduction, microwave imaging arrays (cameras) can be operated either in near field (higher spatial resolution) or far field. If the later is the case (far field imaging), the spatial resolution is fixed by the spot size of the array elements individual beams. In Figure 8, we show the measured spot diameter for the subarray shown in Figure 6 at 20 cm of the antenna (inside an anechoic chamber). These measurement results show 10 cm spot diameters (3 dB) for 13 GHz RF frequency. It is important to highlight that this spot diameter for the antenna elements that fixes the spatial resolution of the imaging system can be improved by increasing the operating frequency, as the types of antennas we are planning to use at higher frequencies present similar radiation patterns. In this situation, it is basically the operation frequency the

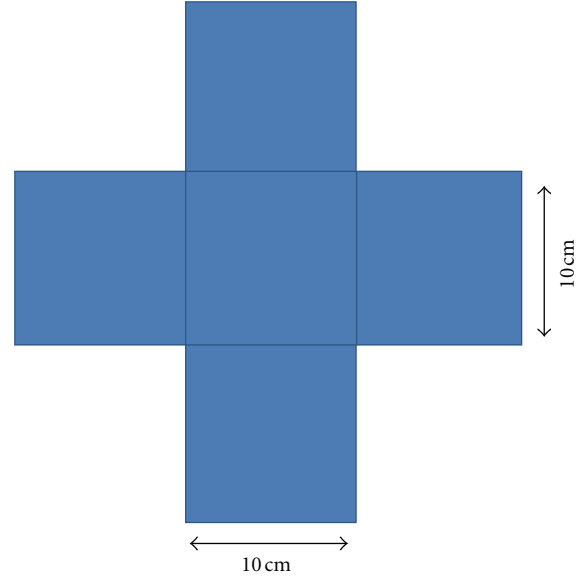


FIGURE 10: Metallic target for the imaging experiment.

parameter that fixes the spatial resolution of the system (beam diameter).

In order to evaluate the imaging performances of the array, an imaging experiment has been carried out (Figure 9). The working frequency has been chosen using the down-conversion ratios map of Figure 3 for optimum performance of the heterodyne photonic pixels ($f_{RF} = 13 \text{ GHz}$, $f_{LO} = 1.1 \text{ GHz}$). The 11.9 GHz IF (intermediate frequency) is remotely recovered for each pixel with a high-speed photodiode). In Figure 9, we can see how a transmitter element (horn) illuminates at the designated frequency (13 GHz) a metallic object placed 3 m from the emitter (horn) and 20 cm from the 3×3 imaging array. It is important to note here that these are the conditions used to evaluate the spot diameter for the independent elements of the array (10 cm, Figure 8), which will limit the spatial resolution of the system. For the results shown in the next section, the metallic object chosen for the imaging experiment is an aluminum cross of $300 \text{ mm} \times 300 \text{ mm}$ dimensions shown in Figure 10. Its dimensions are in the order of magnitude of the beam size.

4. Experimental Results

The images obtained for the object of Figure 10 are shown in Figures 11 and 12 using two different receiving pixels. As a preliminary step, and to separate the influence of the use of an optoelectronic pixel from the actual imaging capabilities of the array built, the array for Figure 7 is equipped with a set of electronic mixers, including RF preamplification, to evaluate the actual spatial resolution of the array. The results obtained are shown in Figure 11, where we can see that the cross is resolved through the simultaneous recovery of the amplitude signals for each pixel of the array. In this sense, it is important to note again that the beam diameter at 20 cm of the array is 10 cm, limiting the spatial resolution as can be extracted from Figure 11.

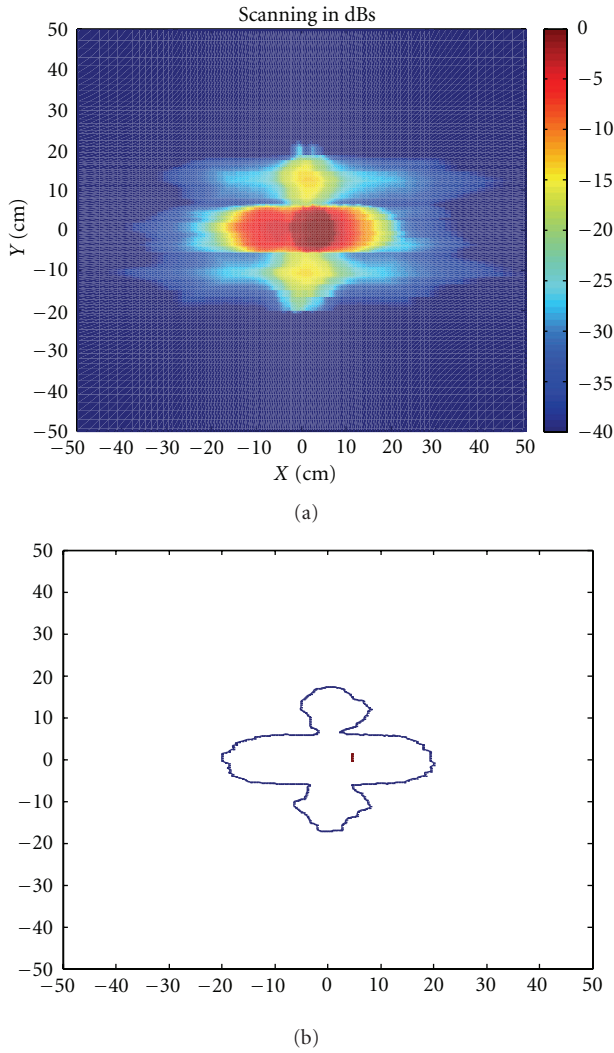


FIGURE 11: Results from the scanning of the object shown in Figure 10 with the 3×3 array using an electronic mixer for heterodyne detection. (a): power difference measured for each pixel with and without the cross (in dB). (b): -10 dB contour for the results shown on (a).

The scanning results obtained for the optoelectronic heterodyne pixel array are shown in Figure 12. We can observe that the image obtained is similar to the one recovered using electronic pixels (Figure 11). It must be noted at this point that, in this case, both the LO and IF are optically distributed using fiber optics to/from the array, eliminating the necessity of further electronics in the individual pixels. In this sense, this photonic-based imaging array presents evident advantages associated with its lower weight, lower power consumption EMI immunity, and flexibility, along with the integration capabilities associated with the possibility of implementing the XN-SOA and optical distribution fibers as photonic integrated circuits.

5. Conclusions

Microwave and millimeter wave imaging techniques have demonstrated their capacities in several and important

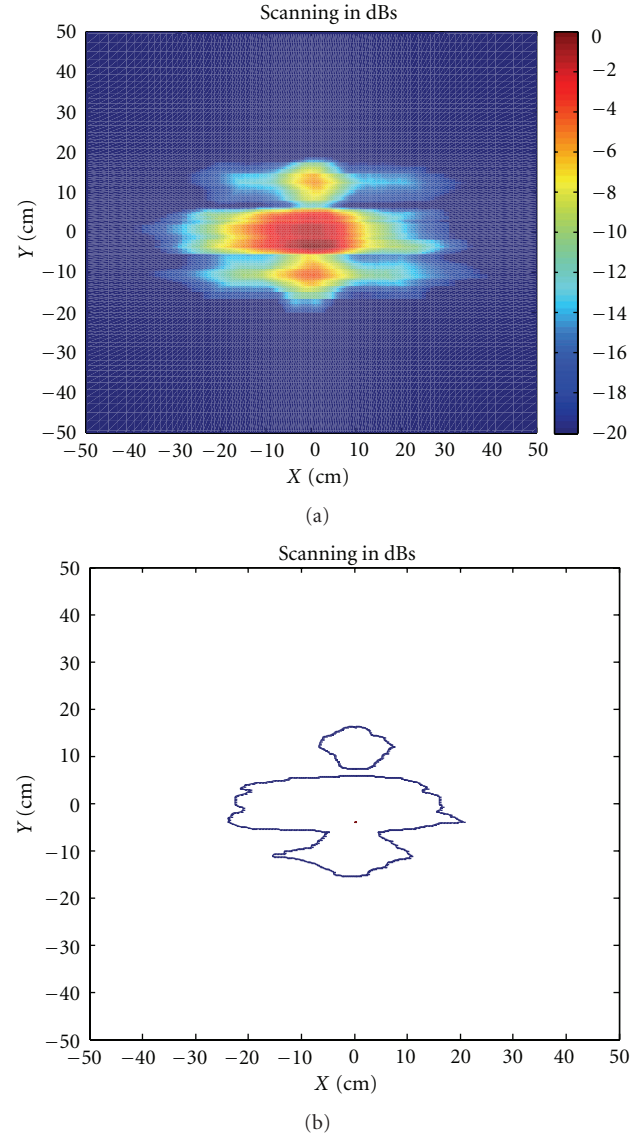


FIGURE 12: Results from the scanning of the object shown in Figure 10 with the 3×3 array using an optoelectronic mixer for heterodyne detection with remote LO and IF distribution. (a): power difference measured for each pixel with and without the cross (in dB). (b): -10 dB contour for the results shown on (a).

application fields. In order to introduce the well-known advantages of microwave photonics and radio-over-fiber techniques in this emerging field, in this work we have designed, implemented, and tested an imaging array based on a photonic heterodyne receivers. The objective is to take advantage of the already well-known advantages of photonic local oscillator distribution in antenna arrays and the introduction of a novel optoelectronic mixer to reduce even further the electronic components count at the antenna front-end, reducing thus power consumption, space, and cost at the expenses of a little less sensitivity. The photonic setup chosen, based on an XN-SOA in EO configuration, reduces also the optical elements typical to other optoelectronic mixers schemes (using external modulators, polarization control optics, etc), allowing for further

integration of the different optoelectronic components in photonic integrated circuits (PICs).

The results shown demonstrate the possibility of using this approximation for imaging arrays in the GHz band, but, even more important, they open the possibility to scale this architecture (once that has been validated) to higher frequencies (100 GHz). This further step is associated with the high bandwidth of the photonic components already available in the market for optical communications. In this sense, preliminary work of 100 GHz imaging arrays are already being under development.

References

- [1] J. Marti and J. Capmany, "Microwave photonics and radio-over-fiber research," *Microwave Magazine, IEEE*, vol. 10, pp. 96–105, 2009.
- [2] P. Berger, J. Bourderionnet, F. Bretenaker, D. Dolfi, and M. Alouini, "Time delay generation at high frequency using SOA based slow and fast light," *Optics Express*, vol. 19, pp. 21180–21188, 2011.
- [3] L. Jofre, C. Stoltidou, S. Blanch et al., "Optically beamformed wideband array performance," *IEEE Transactions on Antennas and Propagation*, vol. 56, no. 6, pp. 1594–1604, 2008.
- [4] T. Kuri, H. Toda, and K. I. Kitayama, "Dense wavelength-division multiplexing millimeter-wave-band radio-on-fiber signal transmission with photonic downconversion," *Journal of Lightwave Technology*, vol. 21, no. 6, pp. 1510–1517, 2003.
- [5] B. Hraimel, X. Zhang, and K. Wu, "Photonic down-conversion of millimeter wave multiband orthogonal frequency division multiplexing ultra-wideband using four wave mixing in an electro-absorption modulator," *Journal of Lightwave Technology*, vol. 28, no. 13, Article ID 5473097, pp. 1987–1993, 2010.
- [6] P. Acedo, H. Lamela, and C. Roda, "Optoelectronic up-conversion using compact laterally mode-locked diode lasers," *IEEE Photonics Technology Letters*, vol. 18, no. 17, pp. 1888–1890, 2006.
- [7] J. Palací, G. Villanueva, and J. Herrera, "EAM-SOA millimeter-wave frequency up-converter for radio-over-fiber applications," *Optics Communications*, vol. 284, no. 1, pp. 98–102, 2011.
- [8] C. Bohémond, A. Sharaiha, T. Rampone, and H. Khaleghi, "Electro-optical radiofrequency mixer based on semiconductor optical amplifier," *Electronics Letters*, vol. 47, no. 5, pp. 331–333, 2011.
- [9] J. H. Seo, C. S. Choi, Y. S. Kang, Y. D. Chung, J. Kim, and W. Y. Choi, "SOA-EAM frequency up/down-converters for 60-GHz Bi-directional radio-on-fiber systems," *IEEE Transactions on Microwave Theory and Techniques*, vol. 54, no. 2, pp. 959–966, 2006.
- [10] C. Bohémond, P. Morel, A. Sharaiha, T. Rampone, and B. Pucel, "Experimental and simulation analysis of the third-order input interception point in an all-optical rf mixer based on a semiconductor optical amplifier," *Journal of Lightwave Technology*, vol. 29, no. 1, Article ID 5638116, pp. 91–96, 2011.
- [11] S. Kharkovsky and R. Zoughi, "Microwave and millimeter wave nondestructive testing and evaluation," *IEEE Instrumentation and Measurement Magazine*, vol. 10, no. 2, pp. 26–38, 2007.
- [12] T. Henriksson, N. Joachimowicz, C. Conessa, and J. C. Bolomey, "Quantitative microwave imaging for breast cancer detection using a planar 2.45 GHz system," *IEEE Transactions on Instrumentation and Measurement*, vol. 59, no. 10, pp. 2691–2699, 2010.
- [13] D. M. Sheen, D. L. McMakin, and T. E. Hall, "Three-dimensional millimeter-wave imaging for concealed weapon detection," *IEEE Transactions on Microwave Theory and Techniques*, vol. 49, no. 9, pp. 1581–1592, 2001.
- [14] M. T. Ghasr, M. A. Abou-Khousa, S. Kharkovsky, R. Zoughi, and D. Pommerenke, "Portable real-time microwave camera at 24 GHz," *IEEE Transactions on Antennas and Propagation*, vol. 60, no. 2, pp. 1114–1125, 2012.
- [15] Á. R. Criado, C. de Dios, and P. Acedo, "Characterization of Ultra Non Linear SOA in a heterodyne detector configuration with remote Photonic Local Oscillator distribution," *IEEE Photonics Technology Letters*, vol. 24, no. 13, pp. 1136–1138, 2012.
- [16] X. Leijtens, "JePPIX: the platform for Indium Phosphide-based photonics," *Optoelectronics, IET*, vol. 5, pp. 202–206, 2011.
- [17] S. Ristic, A. Bhardwaj, M. Rodwell, L. Coldren, and L. Johansson, "An optical phase-locked loop photonic integrated circuit," *Journal of Lightwave Technology*, vol. 28, no. 4, pp. 1–1, 2009.
- [18] K. S. Yngvesson, T. L. Korzeniowski, Y. S. Kim, E. L. Kollberg, and J. F. Johansson, "Tapered slot antenna—a new integrated element for millimeter—wave applications," *IEEE Transactions on Microwave Theory and Techniques*, vol. 37, no. 2, pp. 365–374, 1989.
- [19] C. De Dios and H. Lamela, "Improvements to long-duration low-power gain-switching diode laser pulses using a highly nonlinear optical loop mirror: theory and experiment," *Journal of Lightwave Technology*, vol. 29, no. 5, Article ID 5678610, pp. 700–707, 2011.
- [20] J. B. Rizk and G. M. Rebeiz, "Millimeter-wave Fermi tapered slot antennas on micromachined silicon substrates," *IEEE Transactions on Antennas and Propagation*, vol. 50, no. 3, pp. 379–383, 2002.

Research Article

Fast Optical Beamforming Architectures for Satellite-Based Applications

B. Vidal,¹ T. Mengual,² and J. Martí¹

¹*Nanophotonics Technology Center, Universitat Politècnica de València, 46022 Valencia, Spain*

²*DAS Photonics, Ciudad Politécnica de la Innovación, 46022 Valencia, Spain*

Correspondence should be addressed to B. Vidal, bvidal@dcom.upv.es

Received 19 June 2012; Accepted 17 September 2012

Academic Editor: Nathan J. Gomes

Copyright © 2012 B. Vidal et al. This is an open access article distributed under the Creative Commons Attribution License, which permits unrestricted use, distribution, and reproduction in any medium, provided the original work is properly cited.

Photonic technology offers an alternative implementation for the control of phased array antennas providing large time bandwidth products and low weight, flexible feeding networks. Measurements of an optical beamforming network for phased array antennas with fast beam steering operation for space scenarios are presented. Experimental results demonstrate fast beam steering between 4 and 8 GHz without beam squint.

1. Introduction

The evolution of satellite communication and Earth observation missions has shown a clear trend towards systems with higher performance resulting in higher complexity. More in particular, a key requirement for modern space missions is the operation at wide bandwidths. As far as communication satellites are concerned, wide bandwidths are of great interest in order to accommodate broadband data connections, multiuser operation rates, and wider communications coverage. On the other side, Earth observation platforms also benefit from broadband microwave instruments which can provide a larger number of channels from which more complete and diverse remote sensing information can be extracted.

Additionally, advanced satellite missions are expected to provide high versatility through capabilities such as scanning and multibeam operation which combined to on-board information processing that allow the assignment of resources dynamically.

Wide bandwidth operation requires antenna array systems capable of providing true-time delay (TTD) to avoid beam squint (i.e., changes in the beam steering angle with frequency). However microwave implementations of TTD beamforming networks are rather bulky and heavy with poor harness characteristics, sensitivity to electromagnetic interference and a relatively large crosstalk level which degrade the performance of remote sensing instruments.

On the other hand, photonics allows the implementation of TTD beamforming networks without the problems associated with microwave implementations. Optical beamforming has been studied since the early 90s [1] because it provides many advantages over microwave and digital beamforming, such as light-weight, small size, wideband operation, flexibility, remoting capability, and immunity to electromagnetic interference. Different optical beamforming networks have been presented using a variety of components and arrangements [1–9].

Additionally, some optical beamforming architectures [10–13] offer the capability to control a set of independent beams simultaneously, that is, multibeam operation, although at the cost of increasing the complexity.

This paper reports on the feasibility of implementing fast multibeam TTD optical beamforming architectures to be used in future wideband satellite missions.

2. Fast Beam Steering Applications

Among the many applications of communications and Earth observation satellites [14] several of them would benefit from the capability of steering broadband beams with high speed. Low Earth Orbit (LEO) satellites for remote sensing usually employ a store and forward approach to send data to networks of receiving ground stations, such as Synthetic

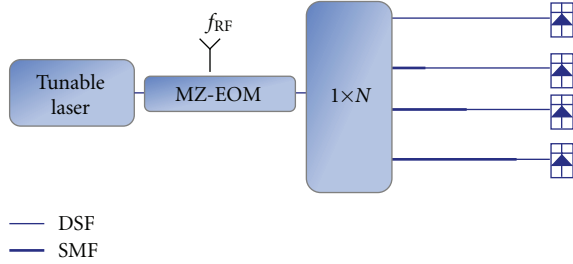


FIGURE 1: Optical beamformer based on a fast tunable laser.

Aperture Radar (SAR) instruments that require the use of several ground stations as well as large capacity on-board memory. Data transmission in this approach can be improved using broadband antenna systems with fast beam steering to track Earth stations and improve signal-to-noise ratio through antenna directivity at the receiver. Additionally, SAR systems show a clear trend toward broader bandwidths and Spot-SAR applications require both wide bandwidths and fast beam switching.

Future Medium Earth Orbit (MEO) constellations will require intersatellite broadband links to cover Internet traffic on satellite mobile phones, as the Iridium constellations actually do to provide voice calls and very limited data traffic. Fast beam steering networks with a limited number of simultaneous beams to track a set of moving satellites will be needed for the deployment of this kind of service.

Finally, satellites at the Geostationary Orbit (GEO) providing Very Small Aperture Terminal (VSAT) applications will apply frequency reuse strategies through fast hopping beam systems.

These and other satellite applications would benefit from the flexibility that fast beam steering broadband satellites could provide.

3. Optical Beamforming Architectures

The wide range of optical beamforming architectures proposed so far tackles different issues and are matched for specific scenarios. The definition of the scenario highly determines the most suitable beamforming architecture. In particular, in this Letter, fast beam steering and multibeam operation with a small/moderate number of antenna elements were identified as the key points for the applications identified in Section 2.

Architectures capable of fulfilling previous requirements include beamforming networks based on a fast tunable laser and a dispersive prism [12]. As shown in Figure 1, the output of the laser is amplitude modulated and launched to a dispersive prism made of a combination of highly dispersive fiber or standard single mode fiber and dispersion shifted fiber. By tuning the wavelength of the optical carrier a different time delay profile can be obtained due to the different time delay introduced by the fact that total dispersion in each branch of the prism is different. In this way, using a fast tunable laser, fast TTD beam steering can be implemented.

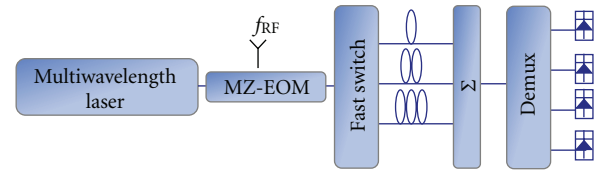


FIGURE 2: Optical beamformer based on a fast switch and dispersive fiber.

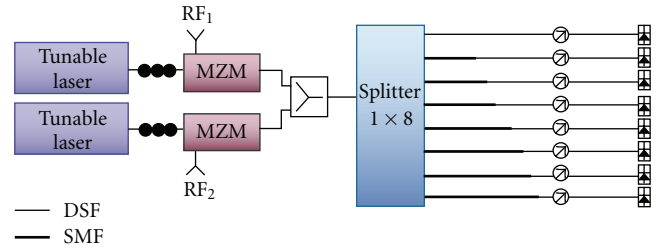


FIGURE 3: Block diagram of a fast multibeam forming network.

A second option is based on a fast switch (Figure 2) [2]. In this case, the architecture needs as many optical carriers as antenna elements (or subarrays if TTD is provided only to subarray level and phase control within the subarrays is done using microwave phase shifters) with a constant wavelength spacing between them. This set of optical carriers is amplitude modulated and using the fast switch is routed to a particular dispersive medium (e.g., a reel of a particular length). Dispersion introduces a relative time delay between optical carriers. Then the signals are combined and each optical carrier is demultiplexed to one photodiode. This architecture can be implemented using cascaded 2×2 fast optical switches or a $1 \times N$ optical switch. Since the cost of a fast optical switch can be significant, the solution based on a single switch should be preferred.

An additional important constraint is the need of multibeam operation. If multibeam is added to the requirement of fast beam steering, the architecture shown in Figure 1 is more suitable than the one of Figure 2. The OBFN based on a dispersive prism has straightforward multibeam capability, each additional beam just requires another optical source and external modulator. The TTD unit provides several time delay profiles when several optical carriers are used simultaneously. On the other hand, the architecture of Figure 2 requires the replication of the fast switch in order to provide multibeam operation (as many optical switches are needed as antenna beams).

4. Experimental Results

Figure 3 shows the block diagram of a fast beam steering architecture with two simultaneous beams.

Fast beam steering is obtained through a fast tunable laser (Intune Altonet 1200, central wavelength 1545 nm approximately) which provides a CW optical carrier whose wavelength can be rapidly tuned among a set of 84 channels with a spacing of 50 GHz (± 2.5 GHz). The beamformer was



FIGURE 4: Picture of the beamformer based on a dispersive prism.

designed to steer the main lobe to broadside at the central wavelength of the optical source (1545 nm approximately). Moreover, to provide fully versatility the beamwidth of each beam could be controlled (i.e., the amplitude contribution of each beam in the antenna elements has to be controlled independently) by means of VOAs (variable optical attenuator). Figure 4 shows a picture of complete beamforming network.

Amplitude and time delay measurements of the eight channels of the beamformer were carried out to derive the radiation pattern for different beam steering angles (i.e., different laser wavelengths). From these measurements, the radiation pattern was derived assuming an antenna array whose elements were set at 0.7λ , where $\lambda = c/(8 \text{ GHz})$. The minimum steering step that the beamformer can achieve using the optical source of the setup is around 1° and it can be swept from 46.9° to -41.9° . This particular resolution is only given by the optical source used in the experiments.

Figure 5, as an example, shows one of the measurements obtained. It presents the estimated radiation pattern for channel 32 (1552.90 nm). It can be seen that the main beam is steered at 20.8° and that the beam steering angle is the same for all the frequencies (i.e., there is no beam squint due to the fact that beam steering is implemented using time delays instead of phase shifts). In addition to the fact that radiation pattern shows no beam squint, also the sidelobe levels are consistent with expected values for uniform amplitude distributions (i.e., around 13.2 dB for a large array). Figure 6 shows how the radiation pattern can be steered by changing the wavelength.

The proposed architecture allows the reconfiguration of the radiation pattern shape. It is shown in Figure 7 where a uniform, triangular, and Taylor amplitude distributions were performed. The radiation pattern reshaping applies to both beams since it is implemented using VOAs which affect equally both optical sources.

To measure the laser switching speed the setup of Figure 8 was implemented. The laser was configured to switch between two wavelengths and an optical filter was used to attenuate one of these wavelengths. In this way, an electrical signal with two levels can be measured at the

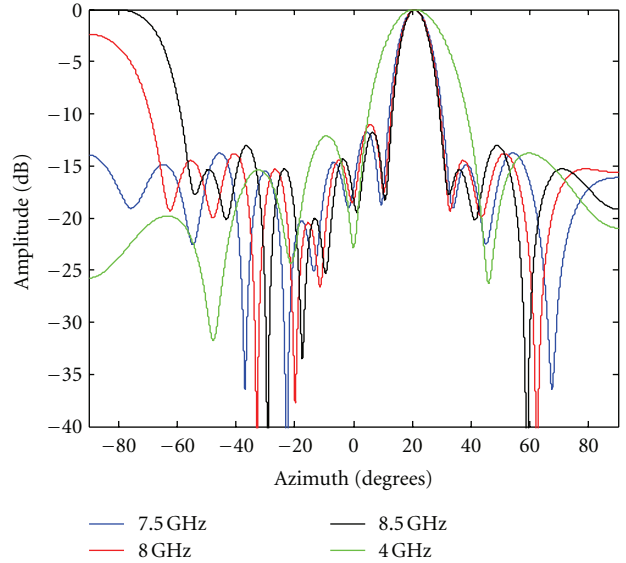


FIGURE 5: Radiation pattern of 8-element antenna calculated from the amplitude and phase when the laser is set at channel 32 (1552.90 nm).

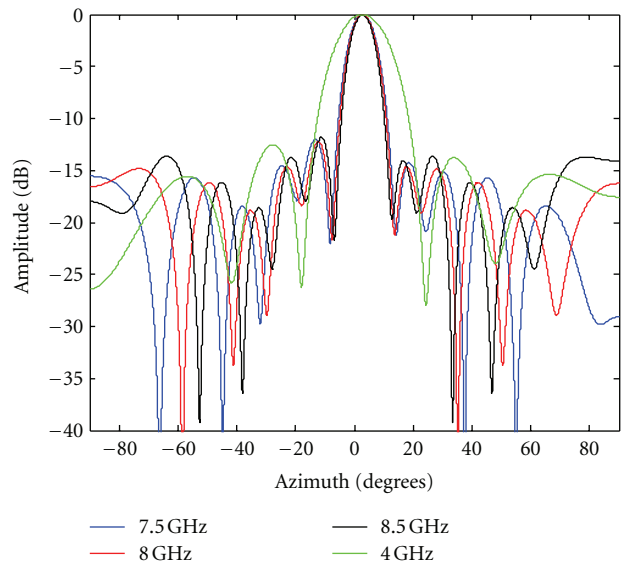


FIGURE 6: Radiation pattern of 8-element antenna calculated from the amplitude and phase when the laser is set at channel 50 (1545.69 nm).

output of a photodiode using an oscilloscope and from these measurements derive the laser switching speed.

As shown in Figure 9, measurements were carried out using two channels of the optical source (in particular channels 37 and 50) with a dwell time in each state of 200 ns (this is the minimum dwell time allowed by the laser evaluation board software). From the results it can be concluded that the laser rise time was 700 ps, the fall time was 1.2 ns, that is, a switching time of around 1 ns. Finally, the measurements show that time in each state was around 440 ns. Since the

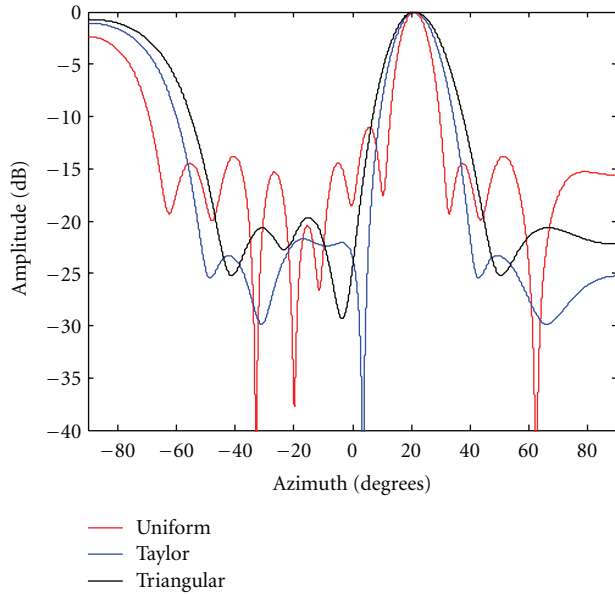


FIGURE 7: Radiation pattern for a uniform, Taylor and triangular amplitude distributions for steering at 20.8° (channel 32, 1552.90 nm).

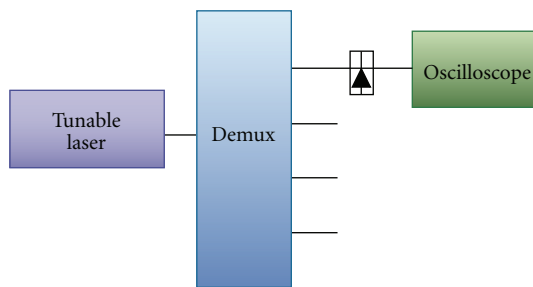


FIGURE 8: Setup for laser speed characterization.

optical source can change from any channel to any other, this architecture allows an arbitrary pattern of steering angles for beam hopping services. For continuous scans the time delay of the sweep would be given by the number of steps which is given by the number of channels of the optical source.

5. Conclusion

Fiber-optic signal processing provides interesting features to implement beamforming networks especially suitable for satellite applications. Key requirements in satellites include low weight, remote delivery to feed deployable array antennas, immunity to electromagnetic interference, and robustness to space radiation. These characteristics match appropriately with inherent features of fiber-optic systems. Additionally, broad bandwidth and fast operation obtained through photonic technology pave the way for the development of new satellite systems with advances capabilities and improved resilience. The use of optical beamforming architectures for satellite applications where fast beam steering

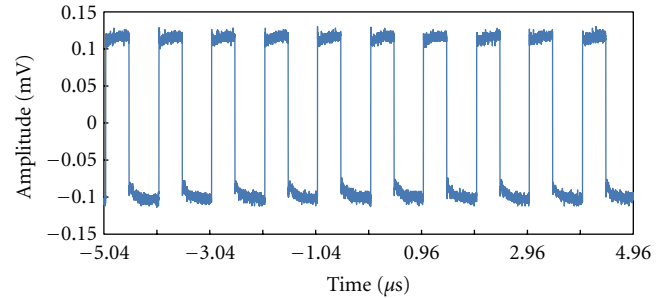


FIGURE 9: Electrical signal at the oscilloscope as shown in Figure 7 for a dwell time of 200 ns.

is required has been reviewed. Measurements of an optical beamforming architecture showing fast operation (switching time of around 1 ns) have been provided between 4 and 8 GHz showing the feasibility of photonic fast beamforming.

References

- [1] W. Ng, A. A. Walston, G. L. Tangonan, I. L. Newberg, J. J. Lee, and N. Bernstein, "The first demonstration of an optically steered microwave phased array antenna using true-time-delay," *Journal of Lightwave Technology*, vol. 9, no. 9, pp. 1124–1131, 1991.
- [2] D. T. K. Tong and M. C. Wu, "A novel multiwavelength optically controlled phased array antenna with a programmable dispersion matrix," *IEEE Photonics Technology Letters*, vol. 8, no. 6, pp. 812–814, 1996.
- [3] B. Vidal, J. L. Corral, M. A. Piqueras, and J. Martí, "Optical delay line based on arrayed waveguide gratings' spectral periodicity and dispersive media for antenna beamforming applications," *IEEE Journal on Selected Topics in Quantum Electronics*, vol. 8, no. 6, pp. 1202–1210, 2002.
- [4] B. Vidal, J. L. Corral, and J. Martí, "Optical delay line employing an arrayed waveguide grating in fold-back configuration," *IEEE Microwave and Wireless Components Letters*, vol. 13, no. 6, pp. 238–240, 2003.
- [5] B. Vidal, T. Mengual, C. Ibáñez-López et al., "Simplified WDM optical beamforming network for large antenna arrays," *IEEE Photonics Technology Letters*, vol. 18, no. 10, pp. 1200–1202, 2006.
- [6] M. A. Piqueras, G. Grosskopf, B. Vidal et al., "Optically beamformed beam-switched adaptive antennas for fixed and mobile broad-band wireless access networks," *IEEE Transactions on Microwave Theory and Techniques*, vol. 54, no. 2, pp. 887–899, 2006.
- [7] B. Vidal, T. Mengual, C. Ibáñez-López, and J. Martí, "Optical beamforming network based on fiber-optical delay lines and spatial light modulators for large antenna arrays," *IEEE Photonics Technology Letters*, vol. 18, no. 24, pp. 2590–2592, 2006.
- [8] L. Jofre, C. Stoltidou, S. Blanch et al., "Optically beamformed wideband array performance," *IEEE Transactions on Antennas and Propagation*, vol. 56, no. 6, pp. 1594–1604, 2008.
- [9] L. Zhuang, C. G. H. Roeloffzen, A. Meijerink et al., "Novel ring resonator-based integrated photonic beamformer for broad-band phased array receive antennas-part II: experimental prototype," *Journal of Lightwave Technology*, vol. 28, no. 1, pp. 19–31, 2010.

- [10] N. A. Riza, "An acoustooptic-phased-array antenna beam-former for multiple simultaneous beam generation," *IEEE Photonics Technology Letters*, vol. 4, no. 7, pp. 807–809, 1992.
- [11] R. D. Esman, M. Y. Frankel, J. L. Dexter et al., "Fiber-optic prism true time-delay antenna feed," *IEEE Photonics Technology Letters*, vol. 5, no. 11, pp. 1347–1349, 1993.
- [12] B. Vidal, M. A. Piqueras, and J. Martí, "Multibeam photonic beamformer based on optical filters," *IEE Electronics Letters*, vol. 42, no. 17, pp. 980–981, 2006.
- [13] L. Yaron, R. Rotman, S. Zach, and M. Tur, "Photonic beam-former receiver with multiple beam capabilities," *IEEE Photonics Technology Letters*, vol. 22, no. 23, pp. 1723–1725, 2010.
- [14] B. R. Elbert, *The Satellite Communications Applications Handbook*, Artech House, Norwood, NJ, USA, 2004.